題目(和文)	発光分光診断によるヘリウムプラズマ電子密度・温度測定における衝突輻射モデルの展開
Title(English)	Advancements in Collisional-Radiative Models for Electron Density and Temperature Determination in Helium Plasma Using Optical Emission Spectroscopy Diagnostics
著者(和文)	LINKeren
Author(English)	Keren Lin
出典(和文)	学位:博士(工学), 学位授与機関:東京工業大学, 報告番号:甲第12539号, 授与年月日:2023年9月22日, 学位の種別:課程博士, 審査員:赤塚 洋,沖野 晃俊,竹内 希,萩原 誠,清田 恭平,江角 直道
Citation(English)	Degree:Doctor (Engineering), Conferring organization: Tokyo Institute of Technology, Report number:甲第12539号, Conferred date:2023/9/22, Degree Type:Course doctor, Examiner:,,,,,
学位種別(和文)	博士論文
Type(English)	Doctoral Thesis

Advancements in Collisional-Radiative Models for Electron Density and Temperature Determination in Helium Plasma Using Optical Emission Spectroscopy Diagnostics

by

Lin Keren

A Doctoral Thesis
Submitted to the Department of Electrical and Electronic Engineering
School of Engineering
Tokyo Institute of Technology

Supervisor: Akatsuka Hiroshi

Date: July.2023

ABSTRACT

In this study, three models of excitation kinetics are developed for determining the electron density and temperature of helium plasma with optical emission spectroscopy (OES) method.

The first model is developed by extracting the dominant processes in the low-pressure helium CR model. The model is able to diagnose electron density and temperature of low-pressure helium plasma with OES measurement by inputting the number density of level 3^1S, 3^3S, and 3^1D. The population and depopulation of state 2^1S, 2^3S, 2^1P, 3^1S, 3^3S, and 3^1D are analysed and the extracted essential processes are used to build simplified rate equations. Electron density and temperature can be determined by finding the global minimum of an objective function based on the simplified rate equations. The model was verified theoretically and experimentally. The results showed the error of electron temperature obtained by the model is generally lower than 0.5 eV. The obtained electron density also agrees well with results of probe method. The model can be applied for diagnosing low-pressure microwave induced helium plasma.

The second model is developed by improving the conventional three-line analysis which based on collisional-radiative (CR) model for plasmas found in the boundary area of thermonuclear fusion reactors with very high-temperature. The number of input lines is increased from three to eight in the present study. The absorption effect of optical thick level 1^1S is included to the CR model. Bias-variance analysis is used to find the suitable fitting parameters (N_1, N_e, T_e, $\Lambda_{4,1}$, $\Lambda_{8,1}$, and $\Lambda_{14,1}$) and the value of the regularization parameter (μ = 5) for the algorithm. The results showed that the difference of levels 3^1S, 3^3S, and 3^1D became larger, but the other levels had better fitting, especially level 4^1D and 4^3D. In general, the new algorithm has relatively better performance compared to the conventional method.

The third model possesses the function of diagnosing the electron density and temperature of atmospheric-pressure helium plasma. The rate coefficients of atomic collision processes are calculated and compiled to the conventional helium CR model to expand its validity to atmospheric pressure. An algorithm is developed to determine the electron density, electron temperature, and number density of two metastable levels by input the number density of eight levels (3^1S, 3^3S, 3^1P, 3^3P, 3^1D, 3^3D, 4^1D, and 4^3D) based on the revised CR model. The results showed that it agrees well with the probe method in the low-pressure microwave induced helium plasma experiment. On the other hand, in the atmospheric-pressure non-equilibrium helium plasma experiment, the electron density and temperature determined by the algorithm also agreed well with those obtained by the continuum spectrum analysis.

CONTENTS

LIST OF FIGURES

LIST OF TABLES

1. INTRODUCTION

1.1. Research Background

Plasmas are known as the fourth state of matters. It can be categorized into many different types according to their characteristic. The following figure shows the electron density N_e and temperature T_e of different types of plasmas.

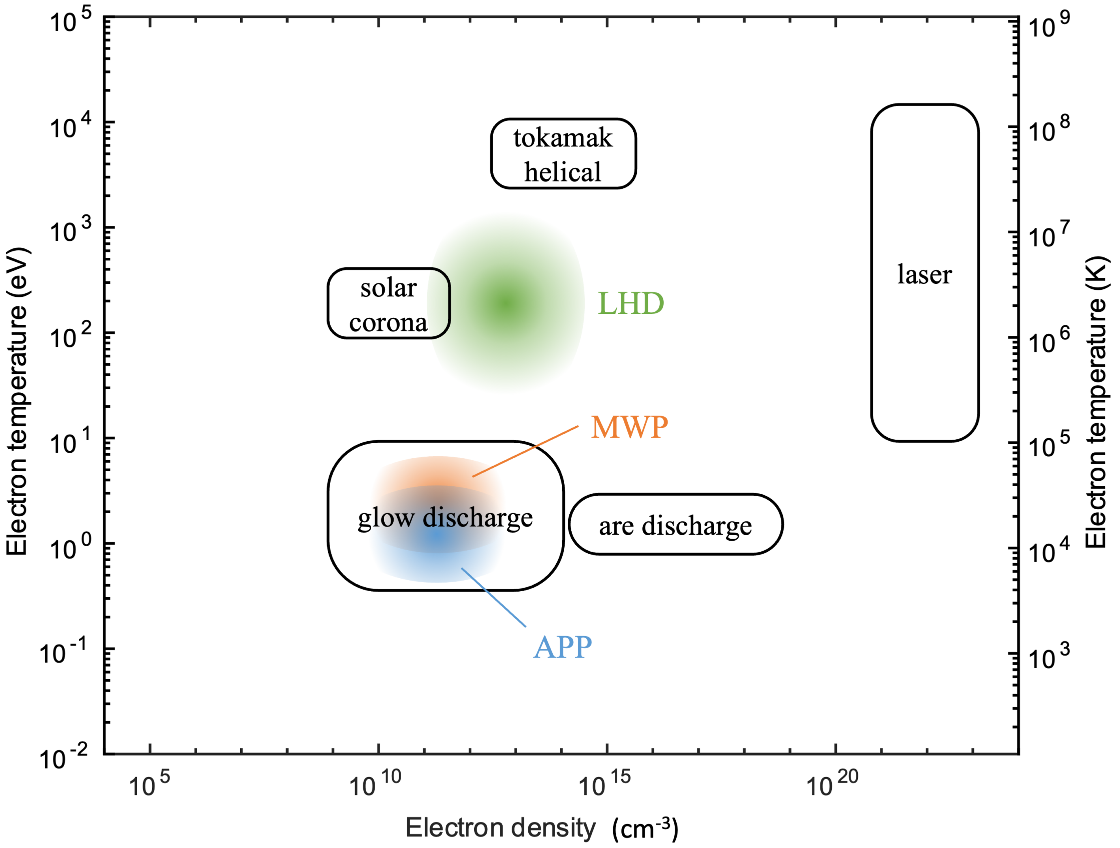

Figure 1. Electron density and temperature of different types of plasmas [1]. APP is the atmospheric pressure plasma. MWP is the microwave induced plasma. LHD is the large helical device plasma.

They have various applications. For example, the DC glow discharge plasma source with controlled potential can be applied for ion implantation [2][3], and the arc discharge can be used to produce material with specific characteristics [4][5][6]. For helium plasmas, they are often used in the field of medical, material processing, and thermonuclear fusion. Many studies have shown that the atmospheric plasma jet treatment is helpful for the recovering of burning wound [7][8]. It can be also applied to process the ceramic material [9][10]. According to Refs. [11][12][13], influences of helium is essential in the fusion reactor as ash of burnt fuel. Therefore, it is important to study the plasma in different conditions and for various applications.

In applications, particularly for medical and dental ones, it is important to obtain plasma parameters precisely, especially the electron density and temperature, since it gives not only an index to categorize the plasma but also a key factor to estimate the number density of reactive species in the processing. Presently, probe and spectroscopy methods are often used to measure plasma parameters. This study focuses on using the optical emission spectroscopy (OES) measurement, which passively measures photons from plasmas, to determine the electron density and temperature of helium plasma.

1.2. Basic Theories

1.2.1. Weakly ionized plasma

The plasmas researched in this study are the weakly ionized plasmas. The fractional ionization of a plasma is

$$x_{\mathrm{iz}} \approx \frac{N_{\mathrm{i}}}{N_{\mathrm{g}} + N_{\mathrm{i}}}, \tag{1.2.1}$$

where N_{g} and N_{i} is the neutral gas and ion density, respectively, and $x_{\mathrm{iz}} \ll 1$ for weakly ionized plasmas. They are usually driven electrically. The most important processes in these plasmas are the collisions of charged species with neutral particles, and the impacts between neutral particles. The surface loss in their boundaries is also essential. The steady state is sustained by the ionization of neutrals. Most parts of the plasmas are in quasi-neutral state, therefore it can be considered:

$$N_{\mathrm{i}} \approx N_{\mathrm{e}}. \tag{1.2.2}$$

If all particles in the plasma are in thermal equilibrium, their temperatures can be characterized by:

$$T_{\mathrm{i}} = T_{\mathrm{e}} = T_{\mathrm{g}}, \tag{1.2.3}$$

where T_{i}, T_{e}, and T_{g} is the ion, electron, and gas temperature, respectively. They are in unit of V in this chapter. Unfortunately, for low-pressure weakly ionized plasma, the applied driven power preferentially heats the mobile electrons. The heavier ions and neutrals can only exchange energy by collisions, so:

$$T_{\mathrm{i}} \ll T_{\mathrm{e}}. \tag{1.2.4}$$

Table 1 shows the parameters of two types of plasmas.

Table 1. Parameters of the low-pressure processing plasma and the high-pressure arc discharge plasma.

	Low-pressure discharges	High-pressure arc discharges
Electron temperature T_{e} (V)	$1-10$	$0.1-2$
Electron density N_{e} (cm^{-3})	$10^{9}-10^{14}$	$10^{14}-10^{19}$
Pressure P (Torr)	$0.001-1$	≈ 760
Ion temperature T_{i} (eV)	$T_{\mathrm{i}} \ll T_{\mathrm{e}}$	$T_{\mathrm{i}} \lesssim T_{\mathrm{e}}$

The parameters indicate that the light and heavy particles are closer to thermal equilibrium at high pressure.

1.2.2. Sheaths

The thin positively charged layers at the boundary of plasmas that are joined to wall surfaces are called sheaths. Assuming a plasma is generated between two grounded walls perpendicular to x-axis in a 2-dimention plane as shown in Figure 1.

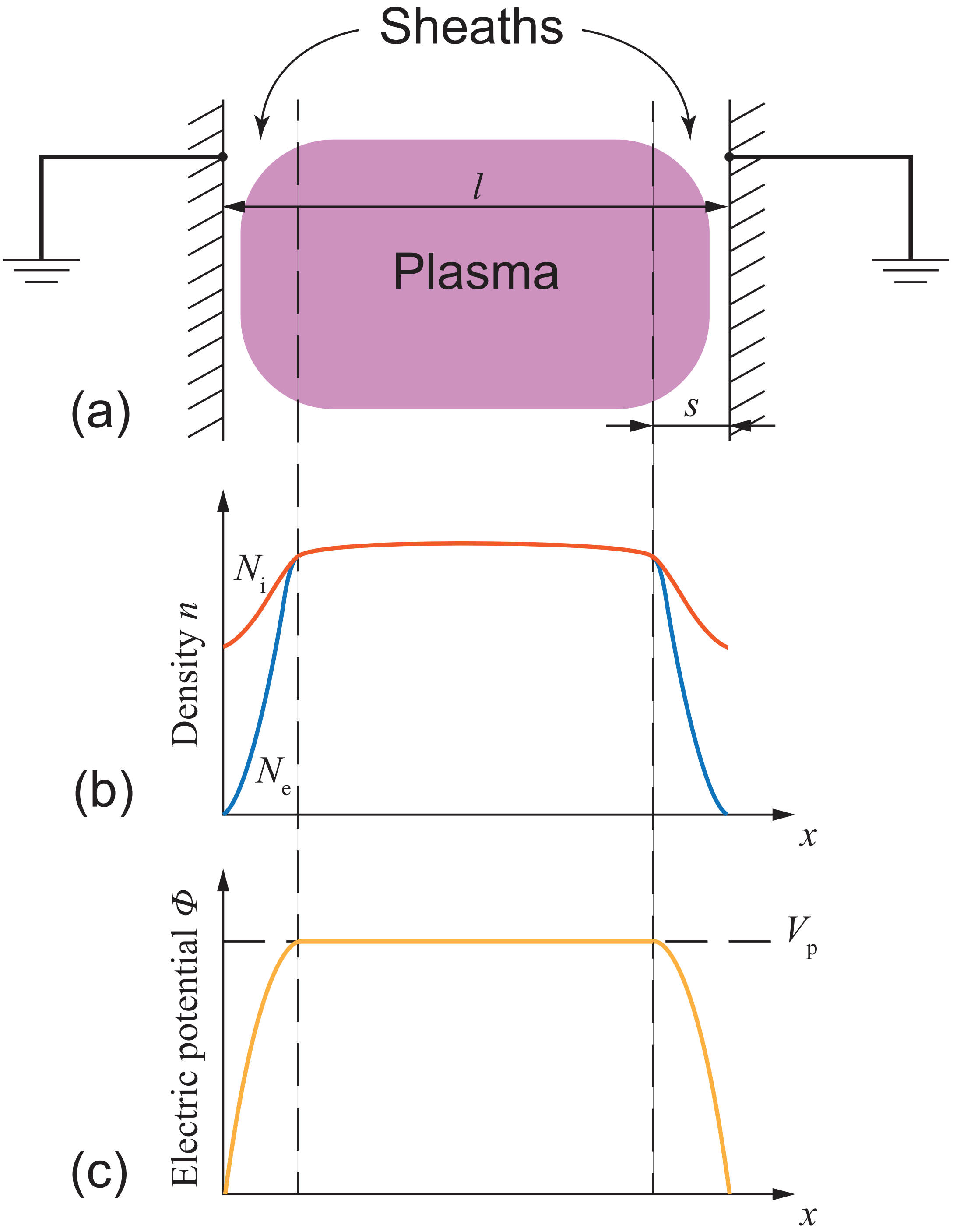

Figure 2. The formation of plasma sheaths. (a) is the overview of the plasma and walls. (b) is the electron and ion densities. (c) is the electric potential.

If the scale of the plasma is larger than the Debye length:

$$\lambda_D[cm] \approx 734\sqrt{\frac{T_e}{N_e}}, \tag{1.2.5}$$

It can be treated as quasi-neutral, and the electric field and electric potential are zero everywhere inside the plasma. The thermal velocity of electrons ($v_{\mathrm{th}}^{\mathrm{e}}$) and that of ions ($v_{\mathrm{th}}^{\mathrm{i}}$) can be obtained by:

$$v_{\mathrm{th}}^{\mathrm{e}} = \sqrt{\frac{eT_{\mathrm{e}}}{m_{\mathrm{e}}}}, \tag{1.2.6}$$

and

$$v_{\mathrm{th}}^{\mathrm{i}} = \sqrt{\frac{eT_{\mathrm{i}}}{m_{\mathrm{i}}}}, \tag{1.2.7}$$

respectively, where e is the element charge, m_{e} and m_{i} is the mass of electron and ion, respectively. If the temperature is in Kelvin (K), Eqs. (1.2.6) and (1.2.7) can be written as:

$$v_{\mathrm{th}}^{\mathrm{e}} = \sqrt{\frac{k_{\mathrm{B}}T_{\mathrm{e}}}{m_{\mathrm{e}}}}, \tag{1.2.8}$$

and

$$v_{\mathrm{th}}^{\mathrm{i}} = \sqrt{\frac{k_{\mathrm{B}}T_{\mathrm{i}}}{m_{\mathrm{i}}}}, \tag{1.2.8}$$

where k_{B} is the Boltzmann's constant. Since $T_{\mathrm{i}} \lesssim T_{\mathrm{e}}$ and $m_{\mathrm{i}} \gg m_{\mathrm{e}}$,

$$v_{\mathrm{th}}^{\mathrm{e}} \gg v_{\mathrm{th}}^{\mathrm{i}}. \tag{1.2.9}$$

After the plasma is generated, the electrons with high speed are lost to the walls on a very short time-scale, which leads to a potential profile in Figure 1 (c) and the electric fields E. Thus, the ion density, as shown in Figure 1 (b), is much larger than electron density in the sheaths ($N_{\mathrm{i}} \gg N_{\mathrm{e}}$). It should be noted that $l \gg s$. The electric fields in the sheaths pull the electrons back to the plasma, and accelerate the ions to the wall. To confine most electrons, the plasma potential V_p is expected to be a few times of T_{e}.

1.2.3. Maxwell distribution

Normally, electrons are in near-thermal equilibrium at temperature T_{e} but ions are almost never in thermal equilibrium. For a single species in thermal equilibrium, in the absence of time variation, spatial gradients, and accelerations, the maxwell distribution can be applied:

$$f'(v) = N\left(\frac{m}{2\pi k_{\mathrm{B}}T}\right)^{3/2} \exp\left(\frac{-mv^2}{2k_{\mathrm{B}}T}\right). \tag{1.2.10}$$

where the temperature is in unit of K. For electrons, they have the classical Maxwell-Boltzmann distribution:

$$f(v) = 4\pi v^2\left(\frac{m_{\mathrm{e}}}{2\pi k_{\mathrm{B}}T_{\mathrm{e}}}\right)^{3/2} \exp\left(-\frac{m_{\mathrm{e}}v^2}{2k_{\mathrm{B}}T_{\mathrm{e}}}\right), \tag{1.2.11}$$

which satisfies the following normalization condition:

$$\int f(v)\mathrm{d}v = 1. \tag{1.2.12}$$

The average velocity is

$$\bar{v} = \sqrt{\frac{8k_{\mathrm{B}}T_{\mathrm{e}}}{\pi m_{\mathrm{e}}}}, \tag{1.2.13}$$

the root mean square velocity is

$$\sqrt{\langle v\rangle^2} = \sqrt{\frac{3k_{\mathrm{B}}T_{\mathrm{e}}}{m_{\mathrm{e}}}}, \tag{1.2.14}$$

and the most probable velocity is

$$v_{\mathrm{p}} = \sqrt{\frac{2k_{\mathrm{B}}T_{\mathrm{e}}}{m_{\mathrm{e}}}}. \tag{1.2.15}$$

The corresponding electron energy distribution function (EEDF) can be obtained by:

$$f(\epsilon) = 2\sqrt{\frac{\epsilon}{\pi}}(k_{\mathrm{B}}T_{\mathrm{e}})^{-3/2}\exp\left(-\frac{\epsilon}{k_{\mathrm{B}}T_{\mathrm{e}}}\right) \tag{1.2.16}$$

with normalization:

$$\int f(\epsilon)\, d\epsilon = 1, \tag{1.2.17}$$

and the average energy is

$$\bar{\epsilon} = \frac{3}{2}k_{\mathrm{B}}T_{\mathrm{e}}. \tag{1.2.18}$$

1.2.4. Neutral hydrogen and hydrogen-like ions

Considering an ion with charge ze with Coulomb attraction field at the origin, and an electron with charge $-e$ moving around it. The quantization scheme of the classical electron motion can be illustrated as shown in Figure 2 [13][14][15]. The total energy E is the sum of the kinetic and potential energies, which is negative. τ is the period of the orbit. λ and μ_{λ} are the angular momentum and its projection onto a certain direction, respectively. $2\pi\mu_{\lambda}$, $2\pi\lambda$, and $-2E\tau$ are chosen as the *x*-, *y*-, and *z*-axis. respectively. All the possible orbits are included in the space enclosed by three planes:

$$2\pi\lambda = 2\pi\mu_{\lambda}(x = y), \tag{1.2.19a}$$

$$2\pi\lambda = -2\pi\mu_{\lambda}(x = -y), \tag{1.2.19b}$$

and

$$2\pi\lambda = -2E\tau(y = z). \tag{1.2.19c}$$

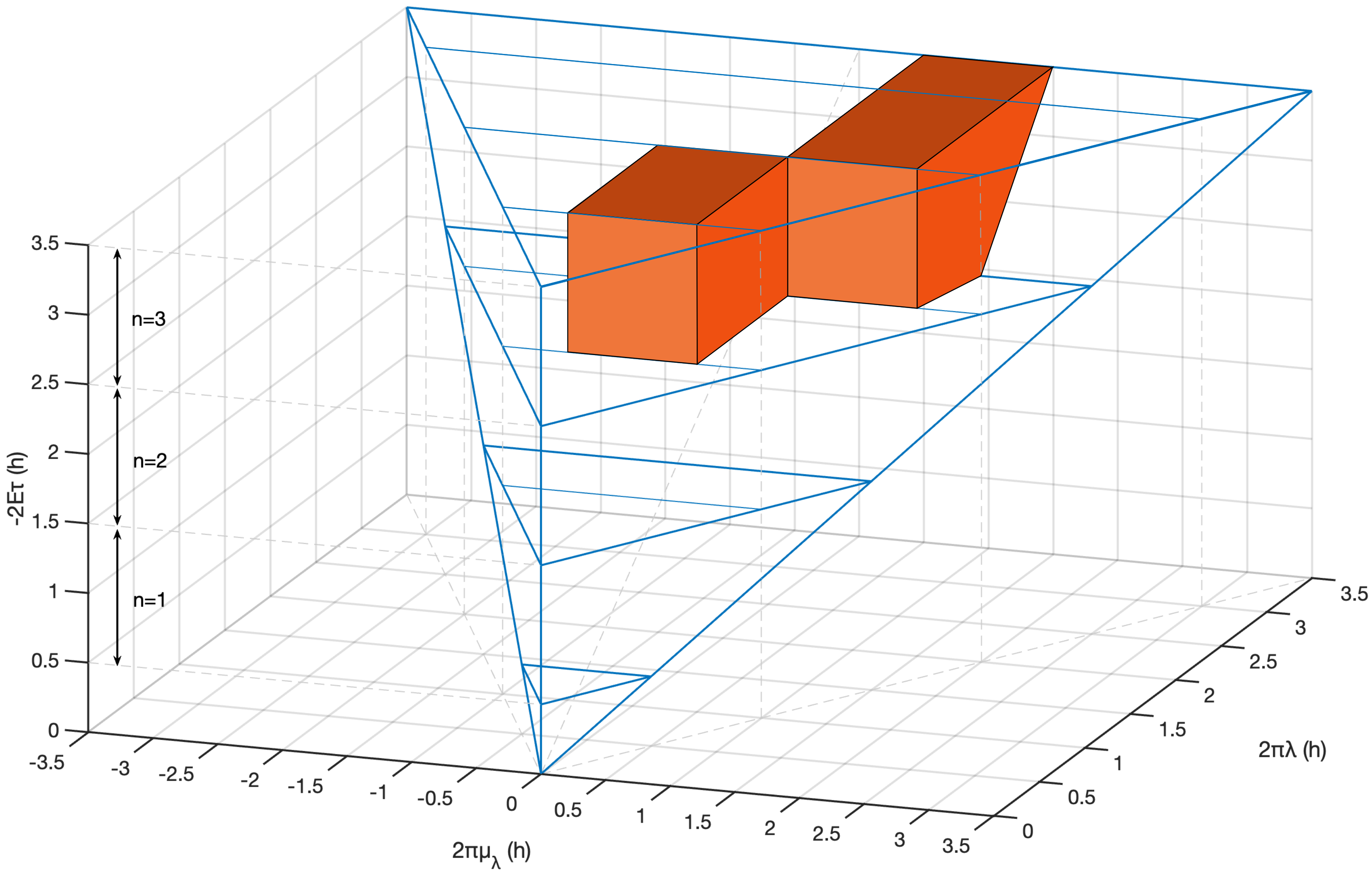

Figure 3. The quantization scheme of the classical electron motion of a hydrogen-like ion [16].

It should be noted that parameters are in units of h. The whole space can be divided into elementary cells in the volume of h^3 according to the following rules:

1. $m_l - 0.5 < 2\pi\mu_\lambda/h < m_l + 0.5$,

2. $l - 1 < 2\pi\lambda < l + 1$,

3. $n - 0.5 < -2E\tau/h < n + 0.5$,

where n, l, and m_l are called the principal quantum number, angular momentum quantum number, and the magnetic quantum number, respectively. The orange volumes in Figure 2 represent state in $(n, l, m_l) = (3, 1, 0)$ and $(n, l, m_l) = (3, 2, 0)$, respectively. The energy of levels with the same *n* is given by:

$$E_n = -\frac{R_0}{n^2}, \tag{1.2.20}$$

where R_0 is the Rydberg constant. It can be obtained by:

$$R_0 = -\frac{e^2}{8\pi\varepsilon_0 a_0} = 2.1799 \times 10^{-18}\ \mathrm{J} = 13.605\ \mathrm{eV}, \tag{1.2.21}$$

where $\varepsilon_0 = 8.854 \times 10^{-12}[\mathrm{C/Vm}]$ is the dielectric constant of vacuum and a_0 is the first Bohr radius:

$$a_0 = \frac{\varepsilon_0 h}{\pi m_\mathrm{e} e^2}. \tag{1.2.22}$$

1.2.5. Neutral helium

For neutral helium and helium-like ions, there are two electrons. The ground and excited states can be designated by the principal quantum number n of the excited electron, the total orbital angular momentum L, and the total spin angular momentum S. This scheme of combination is call *L-S* coupling. The designation of a certain level can be written as $n^{2S+1}L$, and the $2S + 1$ is called the multiplicity. More specifically, it is called singlet and triplet when S equals to 0 and 1, respectively. $L = 0, 1, 2, 3, \ldots$ is assigned as S, P, D, F, … because of the early nomenclature [17][18][19]. The energy level of neutral helium is shown in Figure 3.

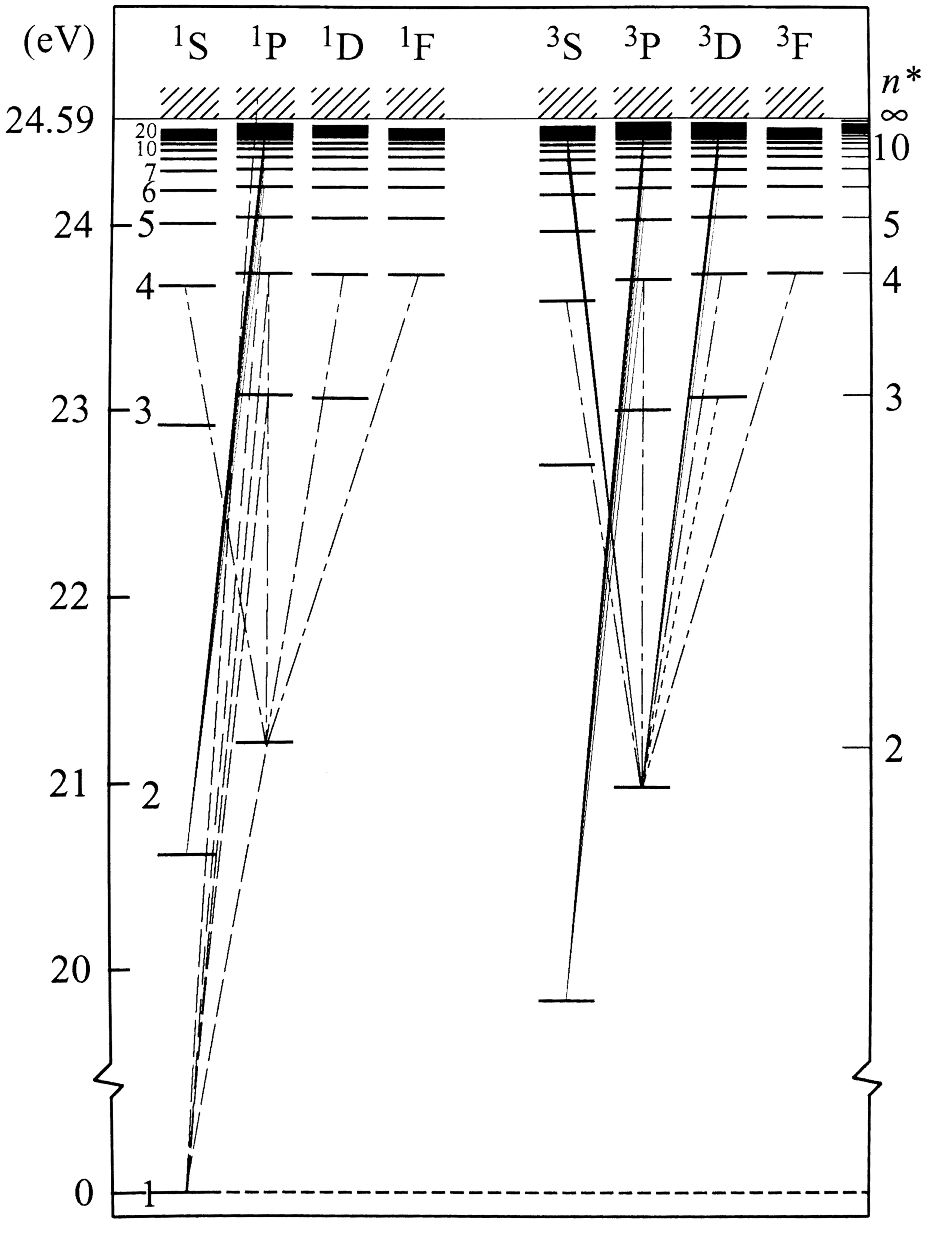

Figure 4. The energy-level diagram of neutral helium [1].

n^* is the effective principal quantum number which can be obtained by:

$$n^* = \sqrt{\frac{\epsilon_{\mathrm{H}}^{\mathrm{io}}}{\epsilon_p^{\mathrm{io}}}}, \tag{1.2.23}$$

where ϵ_H^{io} and ϵ_p^{io} are the first ionization energy of hydrogen and the ionization energy of the level p. The relationship between the excitation and ionization energy of level p is given by:

$$\epsilon_p^{\mathrm{io}} + \epsilon_p^{\mathrm{ex}} = \epsilon_{\mathrm{He}}^{\mathrm{io}} = 24.5874 \text{ eV}, \tag{1.2.24}$$

where $\epsilon_{\mathrm{He}}^{\mathrm{io}}$ is the first ionization energy of helium. The statistical weight of the level p can be calculated by:

$$g_p = (2S + 1)(2L + 1). \tag{1.2.25}$$

The parameters for all levels of helium are show in Table 2. The level p can be further split into fine-structure level with the total angular momentum J ($J = L - S, L - S + 1$, ..., $L + S$). The designation can be written as $n^{2S+1}L_J$ which is also adopted for hydrogen atoms and hydrogen-like ions [20][21][22][23].

Table 2. Parameters of Neutral Helium. ϵ_p^{ex} is the excitation energy of level p.

p	$n^{2S+1}L$	n^*	ϵ_p^{ex} (eV)	$g(p)$	p	$n^{2S+1}L$	n^*	ϵ_p^{ex} (eV)	$g(p)$
1	$1^1\mathrm{S}$	0.744	0	1	34	$6^1\mathrm{F}$+	5.998	24.209	27
2	$2^1\mathrm{S}$	1.850	20.615	1	35	$6^3\mathrm{F}$+	5.998	24.209	81
3	$2^3\mathrm{S}$	1.689	19.819	3	36	$7^1\mathrm{S}$	6.858	24.298	1
4	$2^1\mathrm{P}$	2.009	21.217	3	37	$7^3\mathrm{S}$	6.701	24.284	3
5	$2^3\mathrm{P}$	1.937	20.963	9	38	$7^1\mathrm{P}$	7.011	24.310	3
6	$3^1\mathrm{S}$	2.856	22.920	1	39	$7^3\mathrm{P}$	6.931	24.304	9
7	$3^3\mathrm{S}$	2.697	22.718	3	40	$7^1\mathrm{D}$	6.996	24.309	5
8	$3^1\mathrm{P}$	3.011	23.086	3	41	$7^3\mathrm{D}$	6.996	24.309	15
9	$3^3\mathrm{P}$	2.933	23.006	9	42	$7^1\mathrm{F}$+	6.998	24.309	40
10	$3^1\mathrm{D}$	2.998	23.073	5	43	$7^3\mathrm{F}$+	6.998	24.309	120
11	$3^3\mathrm{D}$	2.997	23.073	15	44	$(n,S) = 8,0$	7.998	24.374	64
12	$4^1\mathrm{S}$	3.858	23.673	1	45	$(n,S) = 8,1$	7.998	24.374	192
13	$4^3\mathrm{S}$	3.700	23.593	3	46	$(n,S) = 9,0$	8.998	24.419	81
14	$4^1\mathrm{P}$	4.011	23.741	3	47	$(n,S) = 9,1$	8.998	24.419	243
15	$4^3\mathrm{P}$	3.932	23.707	9	48	$(n,S) = 10,0$	9.995	24.451	100
16	$4^1\mathrm{D}$	3.997	23.736	5	49	$(n,S) = 10,1$	9.999	24.451	300
17	$4^3\mathrm{D}$	3.997	23.735	15	50	$n = 11$	11	24.468	484
18	$4^1\mathrm{F}$	3.999	23.736	7	51	$n = 12$	12	24.486	576
19	$4^3\mathrm{F}$	3.999	23.736	21	52	$n = 13$	13	24.500	676
20	$5^1\mathrm{S}$	4.858	24.010	1	53	$n = 14$	14	24.511	784
21	$5^3\mathrm{S}$	4.701	23.971	3	54	$n = 15$	15	24.52	900
22	$5^1\mathrm{P}$	5.011	24.045	3	55	$n = 16$	16	24.527	102
23	$5^3\mathrm{P}$	4.931	24.028	9	56	$n = 17$	17	24.533	115
24	$5^1\mathrm{D}$	4.997	24.024	5	57	$n = 18$	18	24.538	129
25	$5^3\mathrm{D}$	4.996	24.042	15	58	$n = 19$	19	24.542	144
26	$5^1\mathrm{F}$+	4.998	24.042	16	59	$n = 20$	20	24.546	160
27	$5^3\mathrm{F}$+	4.999	24.042	48	60	$n = 21$	21	24.549	176
28	$6^1\mathrm{S}$	5.858	24.19	1	61	$n = 22$	22	24.552	193
29	$6^3\mathrm{S}$	5.701	24.168	3	62	$n = 23$	23	24.554	211
30	$6^1\mathrm{P}$	6.011	24.210	3	63	$n = 24$	24	24.556	230
31	$6^3\mathrm{P}$	5.931	24.200	9	64	$n = 25$	25	24.558	250
32	$6^1\mathrm{D}$	5.997	24.209	5	65	$n = 26$	26	24.560	270
33	$6^3\mathrm{D}$	5.996	24.208	15					

1.2.6. Boltzmann distribution

According to the statistical mechanics, if plasmas is in a state of thermodynamic equilibrium, the ratio of number density of the upper level q and the lower level p can be expected by the Boltzmann distribution:

$$\frac{N_q}{N_p} = \frac{g_q}{g_p} \exp\left(-\frac{\epsilon_{p,q}}{k_\mathrm{B} T_\mathrm{e}}\right), \tag{1.2.26}$$

where $\epsilon_{p,q}$ is the difference of the excitation energy between the levels p and q. The thermodynamic relationship could be extended to the continuum states of the electron. Considering continuum states of free electrons have its velocity v within the range dv. The upper level is regarded as the collection of states of the ground-state ion core paired with the free state electrons, the Eq. (1.2.26) can be written as:

$$\frac{N_\mathrm{i}(v)dv}{N_p} = \frac{g_\mathrm{i}(v)dv}{g_p} \exp\left(-\frac{\Delta\epsilon}{k_\mathrm{B} T_\mathrm{e}}\right) \tag{1.2.27}$$

with

$$\Delta\epsilon = \epsilon_p^\mathrm{io} + \frac{1}{2} m_\mathrm{e} v^2. \tag{1.2.28}$$

The statistical weight of the upper level is given by:

$$g_\mathrm{i}(v) = \frac{4\pi {m_\mathrm{e}}^3 v^2}{N_\mathrm{e} h^3} g_\mathrm{e} g_\mathrm{i}, \tag{1.2.29}$$

where g_e and g_i is the statistical weight of electron and ground state of ion, respectively. Since $N_i = \int N_i(v)dv$, by applying the normalization condition for the Maxwell distribution, the Saha-Boltzmann distribution can be obtained:

$$\frac{N_\mathrm{i} N_\mathrm{e}}{N_p} = \frac{2 g_\mathrm{i}}{g_p} {\Lambda_\mathrm{B}}^{-3} \exp\left(-\frac{\epsilon_p^\mathrm{io}}{k_\mathrm{B} T_\mathrm{e}}\right) \equiv {Z_p}^{-1} \tag{1.2.30a}$$

or

$$N_p = Z_p N_\mathrm{i} N_\mathrm{e} \tag{1.2.30b}$$

with

$$Z_p = \frac{g_p}{2g_\mathrm{i}} \left(\frac{h^2}{2\pi m_\mathrm{e} k_\mathrm{B} T_\mathrm{e}} \right)^{3/2} \exp\left(\frac{\epsilon_p^\mathrm{io}}{k_\mathrm{B} T_\mathrm{e}} \right), \tag{1.2.30c}$$

where Z_p is called the Saha-Boltzmann distribution, and Λ_B is the thermal de Broglie wavelength of electrons:

$$\Lambda_\mathrm{B} = \frac{h}{\sqrt{2\pi m_\mathrm{e} k_\mathrm{B} T_\mathrm{e}}}. \tag{1.2.31}$$

1.2.7. Black-body radiation

Considering an ensemble of atoms with two levels p and q $(p > q)$. The temporal development of the upper-level population can be expressed as:

$$\frac{\mathrm{d}N_q}{\mathrm{d}t} = N_p B_{p,q} I_\nu - N_q \left(A_{q,p} + B_{q,p} I_\nu \right), \tag{1.2.32}$$

where $I_\nu\ [\ \mathrm{W \cdot m^{-2} \cdot sr^{-1} \cdot s}\ ]$ is the spectral radiance, A and B are the Einstein coefficients with the interrelationships

$$g_q B_{q,p} = g_p B_{p,q} \tag{1.2.33a}$$

and

$$A_{q,p} = \frac{2h\nu^3}{c^2} B_{q,p}. \tag{1.2.33b}$$

The situation is illustrated in Figure 5.

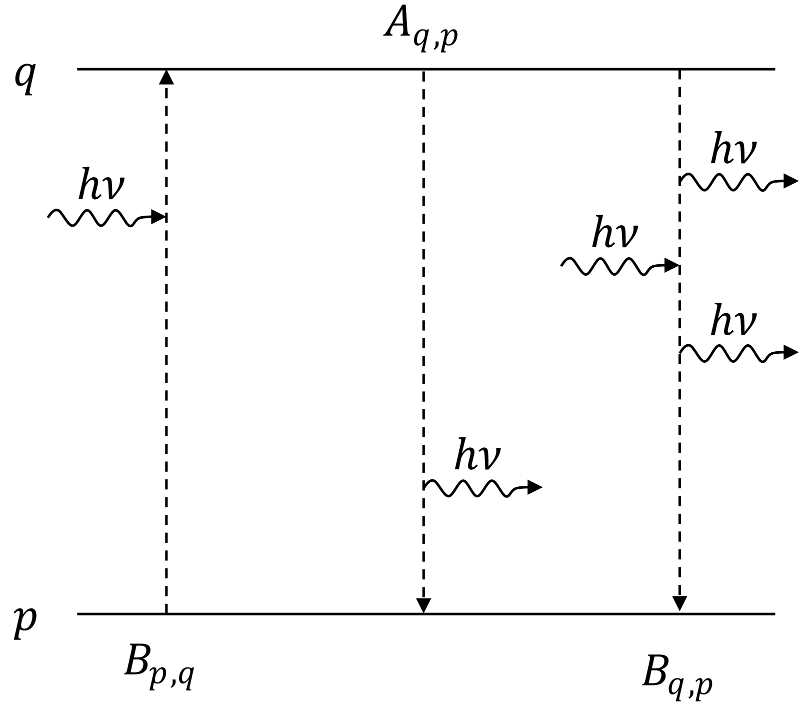

Figure 5. The emission-absorption process of atoms in a radiation field [1].

The three terms on the right-hand-side of Eq. (1.2.32) represent the excitation by absorption of photons, the deexcitation by spontaneous transition, and the induced emission, respectively. By assuming the system is in thermodynamic equilibrium the population ratio can be given by the Boltzmann distribution:

$$\frac{N_q}{N_p} = \frac{g_q}{g_p}\exp\left(-\frac{h\nu}{k_\mathrm{B}T}\right). \tag{1.2.34}$$

Then,

$$I_\nu \mathrm{d}\nu = \frac{2h\nu^3}{c^2}\cdot\frac{\mathrm{d}\nu}{\left(\frac{h\nu}{k_\mathrm{B}T}\right)-1}. \tag{1.2.35}$$

This is called Planck's distribution or black-body radiation. It has a maximum intensity at a certain frequency which is obtained from the derivative of Eq. (1.2.35),

$$\nu_\mathrm{max} \cong 2.8k_\mathrm{B}T/h. \tag{1.2.36}$$

In the low-frequency region ($h\nu \ll k_BT$), Eq. (1.2.35) can be reduced to

$$I_\nu \mathrm{d}\nu = \frac{2k_\mathrm{B}T\nu^2}{c^2}\mathrm{d}\nu, \tag{1.2.37}$$

which is called the Rayleigh-Jeans law. In the high-frequency region ($h\nu \gg k_\mathrm{B}T$), Eq. (1.2.35) can be expressed as

$$I_\nu \mathrm{d}\nu = \frac{2h\nu^3}{c^2}\exp\left(-\frac{h\nu}{k_\mathrm{B}T}\right)\mathrm{d}\nu. \tag{1.2.38}$$

The total energy density of the black-body radiation is given by the Stefan-Boltzmann law:

$$\int_0^\infty \frac{4\pi}{c} I_\nu \mathrm{d}\nu = \frac{8\pi^5 {k_\mathrm{B}}^4}{15h^3c^3}T^4[\mathrm{J}\cdot\mathrm{m}^{-3}]. \tag{1.2.39}$$

It is convenient to express Eq. (1.2.35) in terms of wavelength in some cases:

$$I_\lambda \mathrm{d}\lambda = \frac{2hc^2}{\lambda^5}\cdot\frac{\mathrm{d}\lambda}{\exp\left(\frac{hc}{\lambda k_\mathrm{B}T}\right)-1}. \tag{1.2.40}$$

The peak wavelength in this expression is given by

$$\lambda_\mathrm{max} \cong 2.9\times 10^{-3}/T. \tag{1.2.41}$$

1.2.8. Broadening of Spectral Lines

In practical case, spectral lines are broadened with finite widths. Sometimes, they are also shifted from their original positions. When an emitter of radiation with photon frequency ν_0 is moving with velocity component v toward the detector, the observed frequency of the radiation ν has the following relationship:

$$\frac{\nu-\nu_0}{\nu_0} = \frac{v}{c}. \tag{1.2.42}$$

Then, the observed profile of line has the Gaussian shape:

$$P(\nu)\mathrm{d}\nu = \frac{1}{\Delta\nu_\mathrm{D}\sqrt{\pi}}\exp\left[-\left(\frac{\nu-\nu_0}{\Delta\nu_\mathrm{D}}\right)^2\right]\mathrm{d}\nu, \tag{1.2.43}$$

where $\Delta\nu_D$ is the Doppler width which is given by

$$\Delta\nu_{\mathrm{D}} = \frac{\nu_0}{c}\sqrt{\frac{2k_{\mathrm{B}}T_{\mathrm{g}}}{m_{\mathrm{a}}}}, \tag{1.2.44}$$

where m_{a} is the mass of the corresponding atoms.

1.3. Radiation Transport

In the previous chapter, all photons emitted in the radiative processes are assumed to leave the plasma without absorption. In practical case, photons emitted in a transition from p to q could be absorbed by the lower-lying level p before it leaves the plasma. This chapter will introduce the reabsorption of the photon.

1.3.1. Absorption coefficient

Consider a simple one-dimensional absorption model as shown in Figure 6.

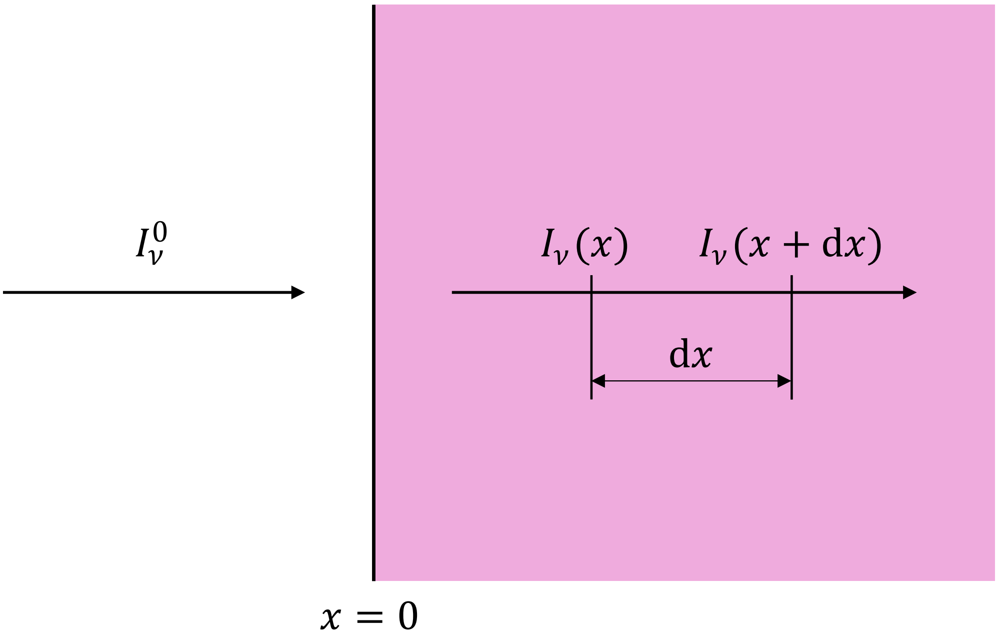

Figure 6. Geomertry of the one-dimentional radiation absorption model.

The radiation with intensity I_ν^0 is incident with the uniform medium at $x \geq 0$. The medium has the absorption property κ_ν, which is called the absorption coefficient. Let the intensity of the radiation at x be $I_\nu(x)$. Then the change in the intensity in the medium is given by

$$I_\nu(x+dx) = I_\nu(x) - \kappa_\nu I_\nu(x)dx, \tag{1.3.1a}$$

and

$$dI_\nu(x) = -\kappa_\nu I_\nu(x)dx. \tag{1.3.1b}$$

The equation is readily solved as

$$I_\nu(x) = I_\nu^0 \exp(-\kappa_\nu x). \tag{1.3.2a}$$

or

$$I_\nu(x) = I_\nu^0 \exp(-\tau_\nu), \tag{1.3.2b}$$

where τ_ν is called the optical depth and κ_ν is given by

$$\kappa_\nu = \frac{h\nu}{4\pi} B_{p,q} N_p P(\nu) = \frac{e^2}{4m_\mathrm{e} c\varepsilon_0} N_p f_{p,q} P(\nu), \tag{1.3.3a}$$

and

$$\int_\mathrm{line} \kappa_\nu d\nu = \frac{e^2}{4m_\mathrm{e} c\varepsilon_0} N_p f_{p,q}. \tag{1.3.3b}$$

The total absorption or the equivalent width is obtained by

$$W = \int_\mathrm{line} \left[1 - \frac{I_\nu(x)}{I_\nu^0}\right] d\nu = \int_\mathrm{line} [1 - \exp(-\kappa_\nu x)] d\nu\,. \tag{1.3.4}$$

In the optical thin case, the total absorption can be obtained by

$$W = x \int_\mathrm{line} \kappa_\nu d\nu = \frac{e^2}{4m_\mathrm{e} c\varepsilon_0} N_p f_{p,q} x. \tag{1.3.5}$$

1.3.2. Emission coefficient

If the uniform medium in Figure 8 is replaced by a plasma that also emits line radiation corresponding to absorption. Defining the emission coefficient as η_ν, then Eqs. (1.3.1a) and (1.3.1b) can be written as

$$I_\nu(x+\mathrm{d}x) = I_\nu(x) - \kappa_\nu I_\nu(x)\mathrm{d}x + \eta_\nu \mathrm{d}x, \tag{1.3.6a}$$

and

$$\mathrm{d}I_\nu(x) = -\kappa_\nu I_\nu(x)\mathrm{d}x + \eta_\nu \mathrm{d}x, \tag{1.3.6b}$$

respectively. I_ν is readily solved as

$$I_\nu(x) = I_\nu^0 \exp(-\kappa_\nu x) + \frac{\eta_\nu}{\kappa_\nu}[1-\exp(-\kappa_\nu x)]. \tag{1.3.7a}$$

In many practical cases, the incident radiation is absent and Eq. (1.3.7a) can be written as

$$I_\nu(x) = \frac{\eta_\nu}{\kappa_\nu}[1-\exp(-\kappa_\nu x)] \tag{1.3.7b}$$

or

$$I_\nu(x) = \frac{\eta_\nu}{\kappa_\nu}[1-\exp(-\tau_\nu)]. \tag{1.3.7c}$$

The emission coefficient is given by

$$\eta_\nu = N_q A_{q,p} \frac{h\nu}{4\pi} P(\nu), \tag{1.3.8}$$

and the absorption coefficients is given by

$$\kappa_\nu = \left(N_p B_{p,q} - N_q B_{q,p}\right) \frac{h\nu}{4\pi} P'(\nu), \tag{1.3.9}$$

where $P'(\nu) = P(\nu)$, which represents complete redistribution of frequency. Then, η_ν/κ_ν is obtained as

$$\frac{\eta_\nu}{\kappa_\nu} = \frac{N_q A_{q,p}}{N_p B_{p,q} - N_q B_{q,p}} = \frac{2h\nu^3}{c^2} \cdot \frac{1}{N_p g_q / N_q g_p - 1}. \tag{1.3.10}$$

By applying Boltzmann distribution, see Eq. (1.2.26), Eq. (1. 3.10) can be expressed in terms of the temperature:

$$\frac{\eta_\nu}{\kappa_\nu}=\frac{2h\nu^3}{c^2}\cdot\frac{1}{\exp\left(\frac{h\nu}{k_\mathrm{B}T_\mathrm{ex}}\right)-1}, \tag{1.3.11}$$

where T_{ex} is called the excitation temperature for the level p and q populations. In the optically thin case ($\tau_\nu \ll 1$), Eq. (1.3.7c) can be written as

$$I_\nu(x)=\eta_\nu x. \tag{1.3.12}$$

Then,

$$\int_\mathrm{line} I_\nu(x)d\nu = N_q A_{q,p}\frac{h\nu}{4\pi}x. \tag{1.3.13}$$

1.3.2. Optical escape factor

In the optical thick case, the actual depopulating flux contributed by the radiative spontaneous transition $A_{q,p}$ and its corresponding absorption effect can be written as

$$\Gamma = N_q \Lambda_{q,p} A_{q,p}. \tag{1.3.14}$$

where $\Lambda_{q,p}$ is called the escape factor or the optical escape factor. According to Refs. [24][25][26][27][28], for an infinite cylindrical geometry, in the case of a Gaussian profile, the optical escape factor is given by

$$\Lambda_{q,p}\approx\frac{1.6}{\kappa_0 R\sqrt{\pi \ln(\kappa_0 R)}}, \tag{1.3.15}$$

where κ_0 and R are the absorption coefficient at line center and the tube radius respectively. The absorption coefficient is given by:

$$\kappa_0=\frac{e^2}{8m_\mathrm{e}c\varepsilon_0\Delta\nu_\mathrm{D}\pi^{3/2}}N_p f_{p,q}. \tag{1.3.16}$$

It is usually preferred to use the following fitted equation to calculate the optical escape factor over a wider range of optical thickness:

$$\Lambda_{q,p} \approx \frac{1.92 - \dfrac{1.3}{1 + (\kappa_0 R)^{6/5}}}{(\kappa_0 R + 0.62)\sqrt{\pi \ln(1.357 + \kappa_0 R)}}. \tag{1.3.17}$$

In the optical thin case, the optical escape factor is given by:

$$\Lambda_{q,p} \approx 1. \tag{1.3.18}$$

1.4. Current Diagnostic Methods for Helium Plasma

The studies introduced in this paper focus on diagnosis of electron density and temperature of different types of helium plasma. It has important application value in various fields such as material surface treatment [29], biomedicine [30], and nuclear fusion [31]. Some of them are generated at atmospheric pressure with low electron temperature, while others are generated at low pressure with extremely high electron temperature [32]. Different methods are usually used to diagnose different types of plasma. In order to explore the physical characteristics and chemical reaction mechanisms of helium plasma, it is necessary to accurately diagnose its electron density and temperature. Electron density and temperature are important parameters that affect energy distribution, transport, stability, and radiation. They reflect the thermodynamic and dynamic state of the plasma. Different methods are usually used to diagnose different types of plasma.

Optical emission spectroscopy (OES) is a commonly used diagnostic method for helium plasma. It uses the principle, as shown in the previous chapters, that atoms or molecules in plasma emit characteristic spectral lines after deexcitation. By measuring the intensity, wavelength and width of the spectral lines, information such as number density of excited states. The OES method has the following advantages: it does not need to contact the plasma and does not affect its state; it is suitable for plasma of different pressures and compositions; it can achieve spatial and temporal resolution; it can simultaneously measure multiple elements or impurities.

In recent years, the research progress on the OES method for electron temperature and density of helium plasma mainly includes the following aspects:

- The establishment of the collisional-radiative (CR) model. The collisional-radiative model is a mathematical model that describes the relationship between the number density of excited states and electron density and temperature in plasma [24]. It is the theoretical basis for diagnosing electron density and temperature by OES method. The establishment of the CR model needs to consider various atomic reaction processes in plasma, such as collisional excitation, collisional de-excitation, spontaneous transition, stimulated radiation, charge exchange, ionization and recombination. The evaluation of the CR model needs to consider factors such as the solution method of the model equation, the uncertainty of the rate coefficients, the number of energy levels included in the model, the influence of molecular ions, and comparison with experimental data. For example, the CR model suitable for low-pressure helium plasma [33] and the CR model for atmospheric pressure argon plasma [34][35] have been developed.

- Electron density and temperature diagnostic method based on spectral line intensity ratio. The diagnostic method based on spectral line intensity ratio uses the characteristic that the number density of different states changes with electron temperature and density. By measuring the ratio of the intensities of two or more spectral lines, electron temperature and density can be obtained simultaneously. This method does not require absolute calibration and is not affected by the self-absorption effect, so it has high accuracy and reliability. The diagnostic method based on spectral line intensity ratio requires the selection of appropriate spectral line pairs or combinations to ensure sufficient sensitivity and discrimination to electron temperature and density [36][38].

Existing OES diagnosis of electron density and temperature of helium plasma based on CR model mainly uses three spectral lines in the visible wavelength range [37]. Although it can be applied to the diagnosis of low-pressure plasma, the rate equation is complicated and requires a lot of calculations. The CR model suitable for Large Helical Device (LHD) helium plasma still has accuracy problems because it does not consider the self-absorption effect [37]. In addition, since the current CR model does not consider atomic collision processes, it can only be applied to low pressure.

This paper will introduce three studies to solve the above problems. The first study solves the problem that the rate equation of the CR model is complicated and difficult to calculate through dominant process extraction. The second study improves the accuracy of the helium plasma CR model for LHD thermos-nuclear fusion plasma by calculating the escape factor and increasing the number of spectral lines used for diagnosis. The third study calculates the rate coefficients of atomic collisions and integrates them into the CR model to expand its valid range to atmospheric pressure for future medical or dental applications, solving the problem that the conventional helium plasma CR model is only suitable for low pressure. The following table shows the target plasma, objectives, and the original work of the corresponding plasma.

Table 3. Overview of the studies.

Chapter	Target plasma	Objectives	Original work
4	Low-pressure microwave induced helium plasma	Simplify the low-pressure CR model	Dominant processes extraction
5	LHD helium plasma (low pressure, high electron temperature)	Improve three-line analysis	Calculation of escape factor, development of new fitting algorithm
6	Atmospheric-pressure helium plasma	Expands the validity of the low-pressure CR model	Calculation of atomic collision rate coefficients, development of atmospheric-pressure helium CR model

2. COLLISIONAL-RADIATIVE MODEL

2.1. Atomic Processes

2.1.1. Atomic processes in helium plasma

In the case of helium plasma, it has the following processes:

$$\mathrm{He}(p) + e^- \underset{F_{q,p}}{\overset{C_{p,q}}{\rightleftarrows}} \mathrm{He}(q) + e^-, \tag{2.1.1a}$$

$$\mathrm{He}(p) + e^- \underset{\alpha_p}{\overset{S_p}{\rightleftarrows}} \mathrm{He}^+ + e^- + e^-, \tag{2.1.1b}$$

$$\mathrm{He}(p) + h\nu \underset{A_{q,p}}{\overset{(1-\Lambda_{q,p})A_{q,p}}{\rightleftarrows}} \mathrm{He}(q), \tag{2.1.1c}$$

$$\mathrm{He}(p) + h\nu \underset{\beta_p}{\rightleftarrows} \mathrm{He}^+ + e^-, \tag{2.1.1d}$$

$$\mathrm{He}(p) + \mathrm{He}(1) \underset{L_{q,p}}{\overset{K_{p,q}}{\rightleftarrows}} \mathrm{He}(q) + \mathrm{He}(1), \tag{2.1.1e}$$

$$\mathrm{He}(p) + \mathrm{He}(1) \underset{W_p}{\overset{V_p}{\rightleftarrows}} \mathrm{He}^+ + e^- + \mathrm{He}(1), \tag{2.1.1f}$$

$$\mathrm{He}_2(p) + e^- \rightleftarrows \mathrm{He}_2(q) + e^-, \tag{2.1.1g}$$

$$\mathrm{He}_2(p) + e^- \rightleftarrows {\mathrm{He}_2}^+ + e^- + e^-, \tag{2.1.1h}$$

$$\mathrm{He}_2(p) + h\nu \rightleftarrows \mathrm{He}_2(q), \tag{2.1.1i}$$

$$\mathrm{He}_2(p) + h\nu \rightleftarrows {\mathrm{He}_2}^+ + e^-, \tag{2.1.1j}$$

$$\mathrm{He}_2(p) + \mathrm{He}(1) \rightleftarrows \mathrm{He}_2(q) + \mathrm{He}(1), \tag{2.1.1k}$$

$$\mathrm{He}_2(p) + \mathrm{He}(1) \rightleftarrows {\mathrm{He}_2}^+ + e^- + \mathrm{He}(1), \tag{2.1.1l}$$

$${\mathrm{He}_2}^+ + \mathrm{He}(1) \rightleftarrows \mathrm{He}^+ + \mathrm{He}(1) + \mathrm{He}(1), \tag{2.1.1m}$$

$$\mathrm{He}_2(p) + \mathrm{He}(1) \rightleftarrows {\mathrm{He}_2}^+ + e^-, \tag{2.1.1n}$$

$$\mathrm{He}(3) + \mathrm{He}(1) \rightleftarrows \mathrm{He}^+ + e^- + \mathrm{He}(1), \tag{2.1.1o}$$

$$\mathrm{He}(3) + \mathrm{He}(1) + \mathrm{He}(1) \rightleftarrows \mathrm{He}_2(2^3\textstyle\sum_u^+) + \mathrm{He}(1). \tag{2.1.1p}$$

They are the electron collision excitation and deexcitation, the electron collision ionization and three-body recombination, the photon excitation and radiative spontaneous transition, the photon ionization and radiative recombination, the atomic collision excitation and deexcitation, the atomic collision ionization and three-body recombination, the excitation and deexcitation of He_2 molecules by electron impacts, the ionization and three-body recombination of He_2 molecules by electron impacts, photon excitation and radiative spontaneous transition of He_2 molecules, the photon ionization and radiative recombination of He_2 molecules, the excitation and deexcitation of He_2 molecules by neutral impacts, the ionization and three-body recombination of He_2 molecules by neutral impacts, the impacts of neutral helium with molecular ions, the Hornbeck-Molnar processes, the Penning ionization, and the triple collision of the metastable state helium $\mathrm{He}(3)$ with the ground state atoms, respectively. At low pressure, only the processes in Eqs. (2.1.1a - d) are essential. At high pressure with high neutral particles densities, Eqs. (2.1.1a - f) will be demonstrated later. For the other processes, they are neglected in this study because they have not been studied yet.

2.1.2. Radiative spontaneous transitions

The Einstein A coefficient (also called transition probability) is used to describe the rate-coefficients of radiative spontaneous transitions. It is given by:

$$A_{q,p} = \frac{2\pi e^2 \nu^2}{m_e c^3 \varepsilon_0} \frac{g_p}{g_q} f_{p,q} [\mathrm{s}^{-1}]. \tag{2.1.2}$$

$f_{p,q}$ is the absorption oscillator strength which is defined by:

$$f_{p,q} = \frac{8\pi^2 m_e}{3h^2} g_q |\langle q|\boldsymbol{r}|p\rangle|^2, \tag{2.1.3}$$

with the electric dipole moment:

$$\langle q|e\boldsymbol{r}|p\rangle = \int \psi_q^* e\boldsymbol{r} \psi_p \mathrm{d}\boldsymbol{r}, \tag{2.1.4}$$

where ψ_p and ψ_q are the wavefunctions and $\boldsymbol{r}$ is the position vector of the optical electron which taking part in the transition. Based on the Kramers formula, the oscillator strength can be simplified as:

$$f_{p,q} = \frac{64}{3\sqrt{3}} \cdot \frac{1}{2n^5 n'^3 \left(n^{-2} - n'^{-2}\right)^3} g_{\mathrm{bb}}, \tag{2.1.5}$$

where g_{bb} the Gaunt factor for bound-bound transitions, n and n' are the principal quantum number of level p and q, respectively.

2.1.3. Photoionization and radiative recombination

Photoionization and radiative recombination are inverse processes with each other. The photoionization cross-section from state p to the continuum state having energy ϵ is given by:

$$\sigma_{p,\epsilon}^{\mathrm{pi}}(\nu) = \frac{2\pi^2 e^2 \nu}{3c\varepsilon_0} |\langle p|\boldsymbol{r}|q_\epsilon\rangle|^2, \tag{2.1.6}$$

where q_ϵ represents the quantum state. Considering the final state are within the energy width $\mathrm{d}\epsilon$ centered at ϵ, Eq. (2.1.6) can be expressed in terms of the differential oscillator strength:

$$\sigma_{p,\epsilon}^{\mathrm{pi}}(\nu) = \frac{e^2}{4m_{\mathrm{e}} c\varepsilon_0} \cdot \frac{\mathrm{d}f_{p,\epsilon}}{\mathrm{d}\nu} \tag{2.1.7}$$

with

$$\mathrm{d}\nu = \frac{\mathrm{d}\nu}{h}. \tag{2.1.8}$$

For hydrogen-like ions, by replacing p and ϵ with the "principal quantum number" n and κ, respectively, the oscillator strength is given as:

$$f_{p,\kappa} = \frac{64}{3\sqrt{3}} \cdot \frac{1}{2n^5 n'^3 \left(n^{-2} + n'^{-2}\right)^3} g_{\mathrm{bf}} \tag{2.1.9}$$

with

$$\mathrm{d}f_{p,\epsilon} = f_{p,\kappa}\mathrm{d}\kappa, \tag{2.1.10}$$

where g_{bf} is the bound-free Gaunt factor. Then, the cross-section of the photoionization can be written as:

$$\sigma_{p,\epsilon}^{\mathrm{pi}}(\nu) = \alpha\pi\frac{64}{3\sqrt{3}}\left(\frac{n^2 a_0}{z}\right)^2\frac{1}{n^3}\left(\frac{z^2 R_0/n}{h\nu}\right)^3 g_{\mathrm{bf}}. \tag{2.1.11}$$

By assuming the thermodynamic equilibrium, the Saha-Boltzmann equation and Planck's distribution can be used for the ionization ratio and the radiation field. Then, the Milne's formula can be obtained as:

$$\frac{\sigma_{p,\epsilon}^{\mathrm{pi}}(\nu)}{\sigma_p^{\mathrm{rad}}(\epsilon)} = \frac{2m_{\mathrm{e}}c^2\epsilon}{h^2\nu^2}\frac{g_{\mathrm{i}}}{g_p} \tag{2.1.12}$$

and

$$\sigma_p^{\mathrm{rad}}(\epsilon) = \pi\frac{64}{3\sqrt{3}}\cdot\frac{z^2R_0}{m_{\mathrm{e}}c^2}\left(\frac{n^2 a_0}{z}\right)^2\frac{1}{n^3}\cdot\frac{1}{1+\epsilon/(z^2R_0/n^2)}\cdot\frac{1}{\epsilon/(z^2R_0/n^2)}g_{\mathrm{bf}}. \tag{2.1.13}$$

The rate-coefficient for the radiative recombination is given as:

$$\begin{aligned}\beta_p &= \int_0^\infty \sigma_p^{\mathrm{rad}}(\epsilon)f(\epsilon)v\mathrm{d}\epsilon \\ &= \sqrt{\frac{2}{m_{\mathrm{e}}}}\int_0^\infty \sigma_p^{\mathrm{rad}}(\epsilon)f(\epsilon)\epsilon\mathrm{d}\epsilon\ [\mathrm{m^3s^{-1}}].\end{aligned} \tag{2.1.14}$$

2.1.4. Electron collision excitation and deexcitation

The electron collision excitation and deexcitation are inverse process with each other. Let $\sigma_{p,q}^{\mathrm{ee}}$ and $\sigma_{q,p}^{\mathrm{ee}}$ represent the cross-sections of the electron collision excitation and deexcitation ($p < q$), respectively. Based on the Maxwell distribution function and the Boltzmann distribution, the following relationship can be obtained:

$$\frac{\sigma_{q,p}^{\mathrm{ee}}(\epsilon)}{\sigma_{p,q}^{\mathrm{ee}}\left(\epsilon_{p,q}+\epsilon\right)}=\frac{g_p}{g_q}\cdot\frac{\epsilon_{p,q}+\epsilon}{\epsilon}, \tag{2.1.15}$$

which is called the Klein-Rosseland formula. The rate coefficient of electron collision excitation is obtained by:

$$C_{p,q}=\int_{\epsilon_{p,q}}^{\infty}\sigma_{p,q}^{\mathrm{ee}}(\epsilon)f\,(\epsilon)v\mathrm{d}\epsilon$$

$$=\sqrt{\frac{2}{m_{\mathrm{e}}}}\int_{\epsilon_{p,q}}^{\infty}\sigma_{p,q}^{\mathrm{ee}}(\epsilon)f\,(\epsilon)\sqrt{\epsilon}\mathrm{d}\epsilon[\mathrm{m}^3\mathrm{s}^{-1}]. \tag{2.1.16}$$

It should be noted that ϵ is measured in units of eV. The electron collision deexcitation rate coefficient is given by:

$$F_{q,p}=\int_{0}^{\infty}\sigma_{q,p}^{\mathrm{ee}}(\epsilon)f\,(\epsilon)v\mathrm{d}\epsilon$$

$$=\sqrt{\frac{2}{m_{\mathrm{e}}}}\int_{0}^{\infty}\sigma_{q,p}^{\mathrm{ee}}(\epsilon)f\,(\epsilon)\sqrt{\epsilon}\mathrm{d}\epsilon$$

$$=\sqrt{\frac{2}{m_{\mathrm{e}}}}\cdot\frac{g_p}{g_q}\int_{\epsilon_{p,q}}^{\infty}\sigma_{p,q}^{\mathrm{ee}}(\epsilon)f\,\left(\epsilon-\epsilon_{p,q}\right)\sqrt{\epsilon}\mathrm{d}\epsilon[\mathrm{m}^3\mathrm{s}^{-1}]. \tag{2.1.17}$$

It can be also obtained by:

$$F_{q,p}=\frac{g_p}{g_q}\exp\left(\frac{\epsilon_{p,q}}{k_{\mathrm{B}}T_{\mathrm{e}}}\right)C_{p,q} \tag{2.1.18a}$$

or

$$F_{q,p}=\frac{Z_p}{Z_q}C_{p,q}. \tag{2.1.18b}$$

Presently, the analytical cross-section [39][40] can be applied for calculating the rate coefficients. It is given by:

$$\sigma_{p,q}^{\mathrm{ee}}(\epsilon)=\pi{a_0}^2\frac{R_0}{g_p}\epsilon^{-1}\Omega\left(\frac{\epsilon}{\epsilon_{\mathrm{th}}}\right), \tag{2.1.19}$$

where Ω is the collision strength. For dipole-allowed transitions ($\Delta S=0$, $\Delta L=\pm1$):

$$\Omega(x) = \left[\xi_1 \cdot \ln(x) + \sum_{i=2}^{5} \left(\frac{\xi_i}{x^{i-2}}\right)\right] \left(\frac{x+1}{x+\xi_6}\right), \tag{2.1.20a}$$

for dipole-forbidden transitions ($\Delta S = 0, \Delta L \neq \pm 1$):

$$\Omega(x) = \left[\sum_{i=1}^{4} \left(\frac{\xi_i}{x^{i-1}}\right)\right] \left(\frac{1}{x^2+\xi_5}\right), \tag{2.1.20b}$$

for spin-forbidden transitions ($\Delta S \neq 0$):

$$\Omega(x) = \left[\sum_{i=1}^{4} \left(\frac{\xi_i}{x^{i-1}}\right)\right] \left(\frac{x^2}{x^2+\xi_5}\right), \tag{2.1.20c}$$

The values of the fit parameters ξ are shown in Tables 4-6 [39]. For the electron collisions with $p \leq 27$ ($5^3\mathrm{F}^+$), $36 \leq q \leq 43$ ($7^3\mathrm{F}^+$), and $p < q$, the rate coefficients can be approximately calculated by:

$$C_{p,q} = \left(\frac{6}{7}\right)^3 C_{p,q-8}, \tag{2.1.21a}$$

and

$$F_{p,q} = \left(\frac{6}{7}\right)^3 F_{q-8,p}. \tag{2.1.21b}$$

Table 4. Fit coefficients for the dipole-allowed excitation collision strength.

p	q	ξ_1	ξ_2	ξ_3	ξ_4	ξ_5	ξ_6
1^1S	2^1P	7.087E-01	9 34 02	9.800E+01	2 986E+00	1 293E+00	3.086E-01
1^1S	3^1P	1.730E-01	2.410E-02	-4.709E-01	7.690E-01	-3.209E-01	8.568E-01
1^1S	4^1P	6.923E-02	6.893E-03	-2.079E-01	3.508E-01	-1.497E-01	4.280E-02
2^1S	2^1P	3.404E+01	7.267E+01	1.710E+02	-2.100E+03	4.704E+02	1.194E+01
2^1S	3^1P	3.336E+00	-1.147E+00	-4.889E+00	2.023E+01	-1.336E+01	1.059E+01
2^1S	4^1P	8.826E-01	-3.618E-01	-1.231E+00	5.606E+00	-3.985E+00	5.890E+00
2^1P	3^1S	4.604E+00	-2.204E+00	-1.093E+01	3.893E+01	-2.440E+01	5.612E+00
2^1P	3^1D	6.255E+01	4.468E+01	-2.409E+02	4.069E+02	-1.955E+02	1.055E+01
2^1P	4^1S	5.545E-01	-4.400E-04	-6.360E-01	1.785E+00	-4.656E-01	3.675E+00
2^1P	4^1D	7.910E+00	9.449E+00	-4.534E+01	7.295E+01	-3.374E+01	5.963E+00
3^1S	3^1P	2.052E+02	3.598E+02	-2.758E+03	5.668E+03	-3.660E+03	1.922E+01
3^1S	4^1P	9.271E+00	-2.468E+00	-2.309E+01	9.929E+01	-7.446E+01	1.829E+01
3^1D	3^1P	2.932E+02	8.061E+02	1.229E+05	-9.222E+05	1.898E+06	1.134E+02
3^1D	4^1F	4.145E+02	3.149E+02	-2.065E+03	3.516E+03	-1.650E+03	2.407E+01
3^1D	4^1P	3.712E+00	2.713E+00	-5.615E+00	5.290E+00	-2.158E+00	0.000E+00
3^1P	4^1S	2.839E+01	-1.091E+01	-7.548E+01	2.545E+02	-1.695E+02	2.058E+01
3^1P	4^1D	1.629E+02	6.048E+01	-1.055E+03	2.398E+03	-1.390E+03	2.594E+01
4^1S	4^1P	6.787E+02	9.856E+02	-1.751E+04	-4.424E+03	2.284E+05	1.876E+01
4^1D	4^1F	8.606E+02	9.447E+03	1.573E+06	8.880E+07	-3.090E+09	2.356E+02
4^1D	4^1P	1.161E+03	3.649E+03	6.912E+05	-1.081E+07	5.967E+07	1.523E+02
2^3S	2^3P	7.696E+01	1.250E+02	4.938E+01	-4.778E+02	3.189E+02	8.157E+00
2^3S	3^3P	3.202E+00	-3.594E+00	3.934E+00	1.138E+01	-9.145E+00	3.360E+00
2^3S	4^3P	9.700E-01	-4.920E-01	1.629E+00	5.632E-01	4.405E-02	5.963E+00
2^3P	3^3S	1.929E+01	4.277E+00	-6.306E+01	1.483E+02	-6.056E+01	8.088E+00
2^3P	3^3D	1.414E+02	9.031E+00	-6.238E+02	1.183E+03	-6.424E+02	8.626E+00
2^3P	4^3S	2.198E+00	2.445E-01	-4.386E-01	-1.691E+00	7.824E+00	4.614E+00
2^3P	4^3D	2.209E+01	2.204E+01	-1.161E-02	2.050E+02	-1.064E+02	5.876E+00
3^3S	3^3P	4.881E+02	7.567E+02	-6.376E+03	1.258E+04	-7.062E+03	1.652E+01
3^3S	4^3P	7.079E+00	-9.037E-01	-1.830E+00	2.059E+01	-8.431E+00	2.199E+00
3^3P	3^3D	9.796E+02	1.371E+03	8.389E+04	-4.649E+05	6.375E+05	4.209E+01
3^3P	4^3S	1.233E+02	2.406E+01	-5.256E+02	1.274E+03	-6.444E+02	2.301E+01
3^3P	4^3D	3.295E+02	6.359E+01	-1.630E+03	4.159E+03	-2.512E+03	2.522E+01
3^3D	4^3F	1.255E+03	8.455E+02	-6.966E+03	1.319E+04	-6.781E+03	2.291E+01
3^3D	4^3P	2.639E+01	-8.708E+00	8.497E+01	4.800E+00	-2.920E+01	4.310E+00
4^3S	4^3P	1.734E+03	2.784E+03	-4.698E+04	1.403E+05	-1.127E+05	3.854E+01
4^3P	4^3D	3.462E+03	8.765E+03	5.011E+05	-6.347E+06	1.989E+07	6.541E+01
4^3D	4^3F	2.884E+03	2.423E+04	1.663E+07	-2.552E+08	2.912E+09	5.760E+02

Table 5. Fit coefficients for the dipole-forbidden collision strength.

p	q	ξ_1	ξ_2	ξ_3	ξ_4	ξ_5
1^1S	2^1S	1.888E+03	-5.754E-01	3439E+ 0	-2.088E+00	2.544E+01
1^1S	3^1S	4.033E-02	-1.872E-02	2.368E+00	-1.379E+00	1.258E+02
1^1S	3^1D	9.708E-03	2.855E-02	-8.265E-02	4.944E-02	1.992E-01
1^1S	4^1S	1.613E-02	-5.564E-02	2.943E-01	-2.024E-01	2.342E+01
1^1S	4^1D	5.420E-03	1.198E-02	-3.173E-02	1.606E-02	1.060E-01
1^1S	4^1F	4.383E-05	-1.033E-04	3.772E-03	1.631E-02	5.644E+01
2^1P	3^1P	1.689E+01	-4.916E+01	1.185E+02	-7.711E+01	1.079E+01
2^1P	4^1F	4.731E+00	2.708E+01	-3.209E+01	1.993E+01	2.372E+01
2^1P	4^1P	3.599E+00	-1.267E+01	1.916E+01	-1.007E+01	0.000E+00
2^1S	3^1S	3.762E+00	-1.140E+01	1.403E+01	-5.377E+00	1.010E+00
2^1S	3^1D	1.058E+01	3.485E+01	7.830E+01	-1.043E+02	5.370E+01
2^1S	4^1S	T.829E-01	-2.417E+00	2.876E+00	-1.108E+00	0.000E+00
2^1S	4^1D	1.872E+00	5.458E+00	-6.857E+00	5.902E+00	3.358E+01
2^1S	4^1F	5.041E-01	4.182E+00	-6.329E+00	3.139E+00	9.425E+00
3^1D	4^1S	5.089E+00	-2.327E+01	5.943E+01	-4.074E+01	6.132E-01
3^1D	4^1D	9.109E+01	-2.982E+02	6.165E+02	-3.155E+02	1.178E+01
3^1P	4^1F	1.542E+02	7.434E+02	4.114E+02	-5.986E+02	2.059E+02
3^1P	4^1P	6.444E+01	-2.365E+02	4.775E+02	-3.084E+02	1.641E+01
3^1S	3^1D	5.183E+01	-1.322E+03	7.452E+04	-9.993E+04	1.321E+03
3^1S	4^1S	1.523E+01	-8.159E+01	1.695E+02	-9.929E+01	5.103E+00
3^1S	4^1D	2.685E+01	-8.58TE+01	1.017E+02	-4.008E+01	0.000E+00
3^1S	4^1F	1.939E+01	-4.539E+01	3.911E+01	-1.204E+01	0.000E+00
4^1S	4^1D	2.148E+02	1.271E+04	1.046E+07	-1.575E+07	9.878E+04
4^1S	4^1F	3.057E+01	-1.045E+03	2.904E+04	-3.037E+0d	4.012E+02
4^1F	4^1P	2.068E+02	-5.424E+04	1.854E+07	-3.077E+07	6.528E+04
2^3S	3^3S	8.344E+00	-2.658E+01	3.488E+01	-1.43IE+01	0.000E+00
2^3S	3^3D	1.679E+01	5.841E+01	3.435E+02	-3.922E+02	6.290E+01
2^3S	4^3S	l.636E+II	-3.577E+00	1.959E+00	8.S21E-01	0.000E+00
2^3S	4^3D	4.063E+£D	1.541E+01	6.089E+01	-7.115E+01	5.762E+01
2^3S	4^3F	5.676E-01	4.383E+00	9.326E+00	-9.539E+00	1.816E+01
2^3P	3^3P	4.512E+01	-1.261E+02	2.182E+02	-6.746E+01	4.133E+00
2^3P	4^3P	9.110E+09	-2.180E+01	2.242E+01	-5.746E+00	0.000E+00
2^3P	4^3F	9.560E+00	5.997E+01	3.657E+01	-5.017E+01	3.155E+01
3^3S	3^3D	1.556E+02	-1.686E+03	4.257E+04	-4.764E+04	2.347E+02
3^3S	4^3S	3.802E+01	-1.898E+02	3.64E+02	1.587E+01	1.719E+01
3^3S	4^3D	3.031E+01	1.193E+02	1.209E+02	-1.560E+02	5.758E+01
3^3S	4^3F	3.902E+01	1.083E 2	8.382E+02	-8.417E+02	4.843E+01
3^3P	4^3F	4.062E+02	1.633E+03	6.40TE+03	1.657E+03	1.825E+02
3^3P	4^3P	1.832E+02	-8.062E+02	1.381E+03	-7.116E+02	2.103E+00
3^3D	4^3S	2.782E+01	9.856E+01	8.697E+02	2.306E+03	1.772E+02
3^3D	4^3D	2.774E+02	-8.107E+02	3.733E+03	-2.662E+03	3.313E+01
4^3S	4^3D	5.093E+02	-1.954E+03	2.489E+03	-1.035E+03	0.000E+00
4^3S	4^3F	1.047E+02	-1.941E+03	2.306E+04	-2.258E+04	9.136E+01
4^3P	4^3F	6.768E+02	-6.926E+04	7.596E+06	-1.069E+07	8.532E+03

Table 6. (a) Fit coefficients for the spin-forbidden collision strength ($n =$ 1 and 2).

p	q	ξ_1	ξ_2	ξ_3	ξ_4	ξ_5
1^1S	2^3P	2.823E-01	2.048E+00	5.287E+00	-7.636E+00	2.728E+01
1^1S	2^3S	6.888E-01	1.975E-01	7.232E+00	-4.839E+00	5.003E+01
1^1S	3^3D	3.172E-03	2.325E-02	-5.084E-02	2.441E-02	-9.854E-01
1^1S	3^3P	6.730E-02	5.465E-01	-4.434E-01	-1.042E-01	1.140E+01
1^1S	3^3S	9.392E-02	-1.641E-01	7.606E-02	-4.536E-03	-9.246E-01
1^1S	4^3D	1.334E-03	1.819E-02	-3.848E-02	1.896E-02	-9.893E-01
1^1S	4^3F	0.000E+00	4.079E-04	-3.863E-04	1.701E-05	-9.497E-01
1^1S	4^3P	2.585E-02	2.275E-01	-5.827E-02	-1.615E-01	1.505E+01
1^1S	4^3S	3.008E-02	-3.956E-02	-1.940E-03	1.154E-02	-9.813E-01
2^1P	3^3D	1.702E+01	1.484E+03	-4.593E+02	-8.789E+02	3.229E+02
2^1P	3^3P	1.093E+01	8.331E+03	1.929E+04	-1.731E+04	5.540E+03
2^1P	3^3S	4.980E+00	4.415E+02	1.002E+03	-8.063E+02	5.626E+02
2^1P	4^3D	3.686E+00	1.887E+02	-9.472E+00	-1.471E+02	1.729E+02
2^1P	4^3F	8.678E-01	3.062E+01	-3.479E+01	1.127E+01	3.760E+01
2^1P	4^3P	2.243E+00	5.624E+02	8.402E+02	-3.634E+02	1.504E+03
2^1P	4^3S	6.494E-01	2.526E+01	-1.162E+00	5.160E+01	1.225E+02
2^1S	2^3P	5.983E+02	-5.310E+02	3.348E+02	-2.412E+02	2.239E+02
2^1S	3^3D	4.042E+00	1.358E+02	8.142E+01	-2.085E+02	1.737E+02
2^1S	3^3P	1.382E+00	8.314E+01	2.834E+02	-1.831E+02	3.176E+02
2^1S	3^3S	6.648E-01	1.940E+03	6.935E+02	1.447E+03	6.339E+03
2^1S	4^3D	9.480E-01	2.121E+01	-7.385E+00	-1.085E+01	7.917E+01
2^1S	4^3F	2.338E-01	-6.755E+01	8.613E+03	-8.035E+03	1.772E+04
2^1S	4^3P	2.701E-01	1.187E+01	7.598E+00	1.182E+00	1.051E+02
2^1S	4^3S	1.236E-01	2.041E+02	-2.538E+02	1.090E+03	3.582E+03
2^3P	2^1P	7.477E+03	-7.356E+01	-1.484E+04	9.359E+03	1.364E+03
2^3P	3^1D	1.248E+01	8.429E+02	-7.194E+02	1.665E+02	2.114E+02
2^3P	3^1P	1.010E+01	3.349E+03	1.034E+04	-1.269E+04	3.023E+03
2^3P	3^1S	3.068E+00	1.914E+02	1.311E+03	-1.191E+03	5.774E+02
2^3P	4^1D	3.009E+00	1.194E+02	-1.716E+02	9.982E+01	9.528E+01
2^3P	4^1F	5.663E-01	1.780E+01	-3.464E+01	1.990E+01	1.573E+01
2^3P	4^1P	2.226E+00	4.009E+02	3.283E+03	-3.644E+03	1.904E+03
2^3P	4^1S	5.902E-01	1.755E+01	1.286E+01	1.786E+01	1.158E+02
2^3S	2^1P	4.893E+01	4.251E+03	-4.330E+03	1.934E+02	8.928E+02
2^3S	2^1S	5.475E+01	3.483E+05	2.545E+05	-5.090E+05	5.424E+04
2^3S	3^1D	1.854E+00	3.979E+01	4.699E+00	-2.647E+01	8.091E+01
2^3S	3^1P	1.383E+00	5.353E+01	3.937E+02	-4.378E+02	4.331E+02
2^3S	3^1S	6.561E-01	5.721E+02	2.975E+03	-1.773E+03	5.210E+03
2^3S	4^1D	5.492E-01	8.462E+00	-1.079E+01	5.007E+00	3.464E+01
2^3S	4^1F	8.208E-02	-1.311E+01	1.155E+03	-1.001E+03	5.398E+03
2^3S	4^1P	3.412E-01	9.770E+00	2.173E+02	-2.240E+02	5.031E+02
2^3S	4^1S	1.694E-01	7.331E+01	8.903E+01	1.828E+02	2.183E+03

Table 6. (b) Fit coefficients for the spin-forbidden collision strength ($n =$ 3 and 4).

p	q	ξ_1	ξ_2	ξ_3	ξ_4	ξ_5
3^1D	4^3D	4. 743E+01	1.223E+05	2.074E+05	-2.839E+05	1.990E+04
3^1D	4^3F	6.314E+01	2.583E+04	-5.741E+03	-1.452E+04	1.536E+03
3^1D	4^3P	0.000E+00	3.369E+03	6.115E+03	-5.152E+03	8.638E+02
3^1D	4^3S	1.499E+00	1.809E+03	1.005E+03	-6.550E+02	9.339E+02
3^1P	4^3D	1.470E+01	5.349E+03	5.281E+03	-9.207E+03	1.556E+03
3^1P	4^3F	7.766E+01	1.248E+04	8.902E+03	-2.051E+04	2.003E+03
3^1P	4^3P	1.125E+01	1.295E+05	5.808E+04	-8.942E+04	4.622E+04
3^1P	4^3S	7.973E+00	5.673E+03	5.417E+03	-6.546E+03	3.901E+03
3^1S	3^3D	6.729E+02	6.022E+05	-2.032E+06	1.788E+06	2.709E+04
3^1S	3^3P	1.242E+03	1.094E+07	-2.101E+07	1.138E+07	3.429E+05
3^1S	4^3D	4.674E+00	2.273E+02	7.469E+02	-8.390E+02	2.907E+02
3^1S	4^3F	1.601E+00	1.311E+03	5.193E+02	-1.588E+03	4.897E+02
3^1S	4^3P	1.878E+00	7.168E+02	1.402E+03	6.210E+01	1.290E+03
3^1S	4^3S	1.395E+00	1.370E+04	-3.392E+04	7.064E+04	2.137E+04
4^1D	4^3F	6.489E+07	2.437E+10	-2.880E+13	9.177E+13	6.255E+06
4^1S	4^3D	9.651E+02	3.404E+07	-1.015E+08	7.969E+07	1.764E+06
4^1S	4^3F	2.102E+02	8.995E+05	-2.902E+06	2.495E+06	3.244E+04
4^1S	4^3P	2.968E+03	1.709E^08	-4.113E+08	3.782E+08	4.486E+06
3^3D	3^1D	1.136E+09	2.017E+12	-1.201E+15	1.669E+17	1 343E+08
3^3D	3^1P	8.097E+04	-7.012E+05	2.225E+06	-2.064E+06	8.385E+03
3^3D	4^1D	4.723E+01	1.223E+05	2.166E+05	-2.717E+05	1.935E+04
3^3D	4^1F	6.305E+01	2.582E+04	-1.481E 04	-5.014E+03	1.496E+03
3^3D	4^1P	0.000E+00	2.958E+03	6.343E+03	-9.301E+03	9.406E+02
3^3D	4^1S	6.079W01	9.783E+02	1.616E+03	-1.574E+03	8.714E+02
3^3P	3^1D	6.039E+03	4.209E+07	-1.969E+08	2.637E+08	2.223E+05
3^3P	3^1P	6.013E+03	-1.055E^04	1.091E+04	-6.078E+03	8.163E+02
3^3P	4^1D	7.376E+00	2.988E+03	8.028E+03	-7.799E+03	1.065E+03
3^3P	4^1F	6.272E+01	6.842E+03	1.574E+03	-5.607E+03	1.122E+03
3^3P	4^1P	2.776E+01	-8.087E+01	3.210E+02	-2.668E+02	2.3S4E+01
3^3P	4^1S	3.4ß3E+00	1.338E+03	5.297E+03	-2.062E+03	2.147E+03
3^3S	3^1D	1.545E+02	4.931E+04	4.578E+04	-9.484E+04	6.629E+03
3^3S	3^1P	8.167E+01	8.655E+04	-5.278E<04	-4.450E+04	1.313E+04
3^3S	3^1S	1.731E+02	2.350E+06	5.044E+06	-7.406E+06	3.601E+05
3^3S	4^1D	3.036E+00	-2.081E+03	6.538E+05	-5.498E+05	1.362E+05
3^3S	4^1F	9.155E-01	6.187E+02	2.079E+02	-6.677E+02	3.049E+02
3^3S	4^1P	1.725E+00	4.197E+02	1.477E+03	-1.845E+03	1.186E+03
3^3S	4^1S	9.802E-01	7.690E+03	-2.354E+04	4.408E+04	1.801E+04
4^3D	4^1D	1.055E+09	-3.116E+11	7.151E+13	-5.641E+15	7.344E+07
4^3D	4^1F	1.828E+07	4.946E+12	-6.367E+14	1.475E+16	5.281E+08
4^3D	4^1P	3.467E+05	-1.223E+05	-1.174E+07	2.974E+07	7.585E+04
4^3F	4^1F	1.026E+10	3.470E+13	-2.933E+16	5.666E+18	6.300E+08
4^3F	4^1P	2.520E+05	-1.057E+06	-1.446E+06	8.086E+06	4.052E+04
4^3P	4^1D	1.466E+04	8.679E+08	-3.528E+09	4.055E+09	4.333E+06
4^3P	4^1F	1.878E+04	4.402E+07	-2.107E+08	2.660E+08	2.108E+05
4^3P	4^1P	1.482E+04	-4.752E+04	3.964E+04	3.244E+03	2.200E+03
4^3S	4^1D	2.220E+02	3.024E+06	9.322E+06	-1.334E+07	4.572E+05
4^3S	4^1F	4.678E+01	7.677E+04	-1.273E+05	6.421E+04	5.849E+03
4^3S	4^1P	1.650E+02	1.455E+06	-2.740E+06	1.284E+06	1.720E+05
4^3S	4^1S	3.429E+02	9.919E+06	-7.244E+06	3.127E+07	1.147E+06

2.1.5. Electron collision ionization and three-body recombination

The Electron collision ionization and three-body recombination are inverse processes with each other. Let σ_p^{ei} donates the electron collision ionization cross-section. The corresponding rate coefficient is given by:

$$S_p = \int_{\epsilon_p^{\mathrm{io}}}^{\infty} \sigma_p^{\mathrm{ei}}(\epsilon) f\,(\epsilon)\sqrt{\epsilon}\mathrm{d}\epsilon. \tag{2.1.22}$$

By applying the Saha-Boltzmann relationship, the electron three-body recombination rate coefficient is obtained as:

$$\alpha_p = Z_p S_p. \tag{2.1.23}$$

The fitted analytic cross-section is suggested for calculating the rate coefficients for levels with $p \leq 19$ $(4^3\mathrm{F})$ [39][41]:

$$\sigma_p^{\mathrm{ei}} = \frac{10^{-13}}{\epsilon_p^{\mathrm{io}}\epsilon}\left[\xi_1 \cdot \ln\left(\frac{\epsilon}{\epsilon_p^{\mathrm{io}}}\right) - \sum_{i=2}^{6} \xi_i \left(1 - \frac{\epsilon_p^{\mathrm{io}}}{\epsilon}\right)^{i-1}\right], \tag{2.1.24}$$

The values of the fit coefficients are shown in Table 7. For $20\ (5^1\mathrm{S}) \leq p \leq 43(7^3\mathrm{F}^+)$, the classical scaling was applied as follows:

$$\sigma_{n^{2S+1}L}^{\mathrm{ei}}(\epsilon) = \left(\frac{\epsilon_{4^{2S+1}L}^{\mathrm{io}}}{\epsilon_{n^{2S+1}L}^{\mathrm{io}}}\right)^2 \sigma_{4^{2S+1}L}^{\mathrm{ei}}\left(\frac{\epsilon}{\epsilon_{4^{2S+1}L}^{\mathrm{io}}/\epsilon_{n^{2S+1}L}^{\mathrm{io}}}\right). \tag{2.1.25}$$

States with $p \geq 44$ $(n > 7)$ are treated as degenerate, and their cross-section is formulated as follows:

$$\sigma_p^{\mathrm{ei}} = 2.32 \times 10^{-16}\left(\frac{13.6}{\epsilon_p^{io}}\right)^2 \frac{\epsilon/\epsilon_p^{\mathrm{io}} - 1}{\left(\epsilon/\epsilon_p^{\mathrm{io}}\right)^2}\ln\left(\frac{1.25\epsilon}{\epsilon_p^{\mathrm{io}}}\right). \tag{2.1.26}$$

Table 7. Fit coefficients for electron collision ionization and double ionization cross-sections.

p	ξ_1	ξ_2	ξ_3	ξ_4	ξ_5	ξ_6
1^1S	5.857E-01	-4.457E-01	7.680E-01	-2.521E+00	3.317E+00	0.000E+00
2^3S	2.427E-01	-1.900E-01	3.205E-01	7.631E-01	-8.329E-01	-2.405E-01
2^1S	3.076E-01	-2.748E-01	4.462E-01	-1.841E-01	1.336E+00	-1.775E+00
2^3P	2.104E-01	-1.750E-01	2.994E-01	9.493E-01	-4.479E-01	-3.833W01
2^1P	2.068E-01	-2.034E-01	5.759E-01	-2.442E-01	1.986E+00	-2.019E+00
3^3S	1.878E-01	-1.871E-01	1.223E+00	-3.805E+00	8.412E+00	-5.872E+00
3^1S	I.787E-01	-1.775E-01	7.023E-01	-1.132E+00	3.727E+00	-5.255E+00
3^3P	2.694E-01	-2.606E-01	6.4T6E-01	-2.256E+00	5.876E+00	-4.273E+00
3^3D	8.034E-02	-7.667E-02	8.839E-01	-4.051E+00	1.110E+01	-7.427E+00
3^1D	9.637E-02	-9.370E-02	1.051E+00	-4.831E+00	1.251E+01	-8.287E+00
3^1P	1.654E-01	-1.640E-01	3.123E-01	-4.326E-02	1.729E+00	-1.691E-F00
4^3S	9.429E-02	-7.480E-02	8.668E-01	-3.637E+00	8.681E+00	-5.816E+00
4^1S	1.206E-01	-1.136E-01	7.407E-01	-3.115E+00	7.325E+00	-4.900E+00
4^3P	2.128W01	-1.957E-01	4.731E-01	-1.800E+00	3.918E+00	-2.596E+00
4^3D	2.507E-02	-4.722E-03	1.340E-01	7.719E-01	-4.388E-01	1.245E-01
4^1D	1.814E-02	1.047E-02	6.380E-02	1.172E+00	-9.804E-01	3.382E-01
4^3F	6.742E-03	4.431E-02	-8.945E-02	1.335E+00	4.955E-01	-1.073E+00
4^1F	4.340E-02	1.216E-02	3.506E-01	-1.911E+00	6.694E+00	-4.631E+00
4^1P	1.807E-01	-1.724E-01	2.448E-01	-6.578E-01	2.026E+00	-1.535E+00
double	1.223E-06	8.208E-03	-6.676E-02	2.978E-01	-1.925E-01	0.000E+00

2.1.6. Atomic collision excitation and deexcitation

The atomic collision excitation and deexcitation are inverse process with each other. It is suggested to use Gousset's equations [42] to calculate the rate coefficient of the L-changing atomic collision excitation ($n = 5, 6,$ and 7) with the gas temperature T_{g}:

$$K_{p,q} = \frac{7.76 \times 10^{-10}}{g_p} \left(\frac{\epsilon_q^{\mathrm{ex}} - \epsilon_p^{\mathrm{ex}}}{k_{\mathrm{B}} T_{\mathrm{g}}} \right)^{-0.29}, \tag{2.1.27a}$$

when $(\epsilon_q^{\mathrm{ex}} - \epsilon_p^{\mathrm{ex}})/(k_{\mathrm{B}} T_{\mathrm{g}}) < 1$, and

$$K_{p,q} = \frac{7.76 \times 10^{-10}}{g_p} \left(\frac{\epsilon_q^{\mathrm{ex}} - \epsilon_p^{\mathrm{ex}}}{k_{\mathrm{B}} T_{\mathrm{g}}} \right)^{-0.29} \mathrm{e}^{-a\left(\frac{\epsilon_q^{\mathrm{ex}} - \epsilon_p^{\mathrm{ex}}}{k_{\mathrm{B}} T_{\mathrm{g}}} \right)}, \tag{2.1.27b}$$

when $(\epsilon_q^{\mathrm{ex}} - \epsilon_p^{\mathrm{ex}})/(k_{\mathrm{B}}T_{\mathrm{g}}) > 1$, where the parameter a is close to unity and depends slightly on the transition from p to q. The rate coefficient of other L-changing excitations is given by:

$$K_{p,q} = 128\pi a_0^2 \left(\frac{\epsilon_{\mathrm{H}}^{\mathrm{io}}}{\epsilon_q^{\mathrm{ex}} - \epsilon_p^{\mathrm{ex}}}\right)^2 f_{p,q} \sqrt{\frac{k_{\mathrm{B}}T_{\mathrm{g}}}{\pi m_{\mathrm{He}}} \cdot \frac{m_{\mathrm{e}} m_{\mathrm{He}}}{m_{\mathrm{H}}(m_{\mathrm{e}} + m_{\mathrm{He}})}}\, \Psi_{p,q} \tag{2.1.28a}$$

with

$$\Psi_{p,q} = 1 + \frac{\dfrac{2k_{\mathrm{B}}T_{\mathrm{g}}}{\epsilon_q^{\mathrm{ex}} - \epsilon_p^{\mathrm{ex}}}}{1 + \left[\dfrac{2m_e k_{\mathrm{B}}T_{\mathrm{g}}}{(m_{\mathrm{e}} + m_{\mathrm{He}})(\epsilon_q^{\mathrm{ex}} - \epsilon_p^{\mathrm{ex}})}\right]^2} \exp\left(-\frac{\epsilon_q^{\mathrm{ex}} - \epsilon_p^{\mathrm{ex}}}{k_{\mathrm{B}}T_{\mathrm{g}}}\right), \tag{2.1.28b}$$

where $\epsilon_{\mathrm{H}}^{io}$ is the first ionisation energy of hydrogen, m_{H}, and m_{He} are the mass of hydrogen atoms, and helium atoms, respectively. The rate coefficient of atomic collision L-changing deexcitation rate coefficient can be determined by the detailed balance equation:

$$L_{q,p} = K_{p,q} \frac{g_p}{g_q} \exp\left(\frac{\epsilon_q^{\mathrm{ex}} - \epsilon_p^{\mathrm{ex}}}{k_{\mathrm{B}}T_{\mathrm{g}}}\right). \tag{2.1.29}$$

For transitions between Rydberg levels $p \geq 44$ ($n > 7$), the rate coefficient is given by[43]:

$$K_{p,q} = \frac{F_{q,p}}{\dfrac{p^{*2}}{q^{*2}} \exp\left[\dfrac{1.58 \times 10^5}{T_{\mathrm{g}}}\left(\dfrac{1}{p^{*2}} - \dfrac{1}{q^{*2}}\right)\right]}, \tag{2.1.30}$$

and

$$L_{q,p} = 1.8 \times 10^{-9} \frac{p^{*6.4}}{q^{*7.4}}, \tag{2.1.31}$$

where p^* and q^* are the effective principal quantum numbers [44][45][46] of the corresponding states. The values of the effective principal quantum numbers are shown in Table 2.

2.1.7. Atomic collision ionization and three-body recombination

The atomic collision ionization and three-body recombination are inverse processes with each other. According to Drawin [47], the rate coefficients of the atomic collision ionization is given by:

$$V_p = 128\pi a_0^2 \left(\frac{\epsilon_{\mathrm{H}}^{\mathrm{io}}}{\epsilon_p^{\mathrm{io}}}\right)^2 \xi_p \sqrt{\frac{k_{\mathrm{B}} T_{\mathrm{g}}}{\pi m_{\mathrm{He}}} \cdot \frac{m_{\mathrm{e}} m_{\mathrm{He}}}{m_{\mathrm{H}}(m_{\mathrm{e}} + m_{\mathrm{He}})}} \Psi_p, \tag{2.1.32a}$$

and

$$\Psi_p = 1 + \frac{\frac{2k_{\mathrm{B}} T_{\mathrm{g}}}{\epsilon_p^{\mathrm{io}}}}{1 + \left[\frac{2m_{\mathrm{e}} k_{\mathrm{B}} T_{\mathrm{g}}}{(m_{\mathrm{e}} + m_{\mathrm{He}})\epsilon_p^{\mathrm{io}}}\right]^2} \exp\left(-\frac{\epsilon_p^{\mathrm{io}}}{k_{\mathrm{B}} T_{\mathrm{g}}}\right). \tag{2.1.32b}$$

Then, the rate coefficient of atomic three-body recombination is obtained by:

$$W_p = V_p \frac{g_p}{2g_{\mathrm{i}}} \left(\frac{h^2}{2\pi m_{\mathrm{e}} k_{\mathrm{B}} T_{\mathrm{e}}}\right)^{3/2} \exp\left(\frac{\epsilon_p^{\mathrm{io}}}{k_{\mathrm{B}} T_{\mathrm{g}}}\right), \tag{2.1.33}$$

2.2. Rate equation

If a plasma is optically thin, it can be assumed that all photons emitted by ions and atoms in the plasma leave the plasma directly without any absorption; if it is also assumed that the plasma is isotropic, the line intensity $\Phi_{p,q}$ of the plasma observed by a spectrometer is given by

$$\Phi_{p,q} = N_p A_{p,q} h\nu V \left(\frac{\mathrm{d}\Omega}{4\pi}\right) \text{ [W]}, \tag{2.2.1}$$

where V and $d\Omega$ is the volume of the plasma for observing and the solid angle. If all geometric factors are known, $\Phi_{p,q}$ is only determined by the number density of the upper level N_p. At low-pressure, by only considering spontaneous radiative transitions and transitions induced by electron impacts and omitting all the other transition processes, the temporal development of the number density of level p can be described

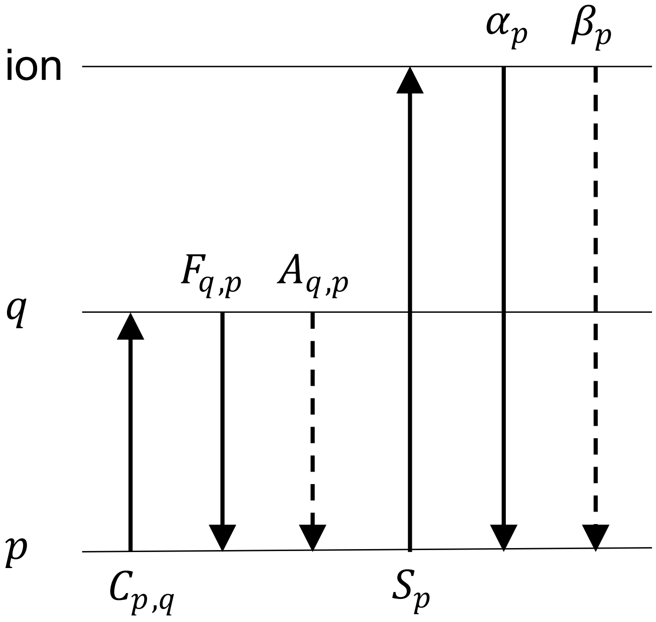

Figure 7. Population and depopulation processes in the atmospheric pressure helium CR model. The solid and dashed lines represent collisional and radiative processes, respectively.

by:

$$\frac{\mathrm{d}N_p}{\mathrm{d}t} = \sum_{q<p} C_{q,p} N_\mathrm{e} N_q + \sum_{q>p} F_{q,p} N_\mathrm{e} N_q + \sum_{q>p} A_{q,p} N_q - \sum_{q>p} C_{p,q} N_\mathrm{e} N_p - \sum_{q<p} F_{p,q} N_\mathrm{e} N_p - \sum_{q<p} A_{p,q} N_p - S_p N_\mathrm{e} N_p + \alpha_p {N_\mathrm{e}}^2 N_\mathrm{i} + \beta_p N_\mathrm{e} N_\mathrm{i}. \tag{2.2.2}$$

It should be noted that the rate equation holds under the assumption that the plasma is homogeneous and the population dynamics are not affected by the ions. Terms like $C_{p,q} N_\mathrm{e}$ or $A_{p,q}$ in units of s^{-1} are called the rate or the probability, and those like $C_{p,q} N_\mathrm{e} N_p$ and $A_{p,q} N_p$ in units of m^{-3}s^{-1} are called the flux.

2.3. Relaxation time

According to Eq. (2.2.2), the rate equation of level p can be expressed as:

$$\frac{\mathrm{d}N_p}{\mathrm{d}t} = \Gamma_{\mathrm{in}} - \Gamma_{\mathrm{out}}$$

$$= \Gamma_{\mathrm{in}} - \zeta N_p, \tag{2.3.1}$$

where Γ_{in}, Γ_{out}, and ζ are the populating flux, the depopulating flux, and the outflow rate, respectively. The solution of steady state is:

$$N_{p_0} = \Gamma_{\mathrm{in}}/\zeta. \tag{2.3.2}$$

Let N_p, $t = 0$, given as $N_p(0) = N_{p_0} + \Delta N_p(0)$, then the rate equation reduces to

$$\frac{\mathrm{d}\Delta N_p(t)}{\mathrm{d}t} = -\zeta \Delta N_p(t). \tag{2.3.3}$$

It is readily solved as:

$$N_p(t) = \frac{\Gamma_{\mathrm{in}}}{\zeta} + \Delta N_p(0)\exp(-\zeta t). \tag{2.3.4}$$

The characteristic time of the equation is defined as the relaxation time $t^{\mathrm{rl}} = \zeta^{-1}$, which is given as:

$$t_p^{\mathrm{rl}} = \left(\sum_{q>p} C_{p,q} N_{\mathrm{e}} + \sum_{q<p} F_{p,q} N_{\mathrm{e}} + \sum_{q<p} A_{p,q} + S_p N_{\mathrm{e}} \right)^{-1}. \tag{2.3.5}$$

For hydrogen-like atoms (ions), a rough approximation of the relaxation time for ground-state can be applied:

$$t_1^{\mathrm{rl}} = (S_1 N_{\mathrm{e}})^{-1}. \tag{2.3.6}$$

According to Fujimito [1], the rate coefficients have the following relationships:

$$C_{p,p+1} \gg C_{p,p+n}, \tag{2.3.7a}$$

$$F_{p,p-1} \gg F_{p,p-n}, \tag{2.3.7b}$$

and

$$C_{p,p+1} \gg S_p, \tag{2.3.7c}$$

Then, it can be concluded:

$$t_1^{\mathrm{rl}} \gg t_p^{\mathrm{rl}}\ (p \geq 2). \tag{2.3.8}$$

Except for extreme situations, it can be also assumed:

$$N_1 + N_{\mathrm{i}} \gg \sum_{p \geq 2} N_p\,. \tag{2.3.9}$$

2.4. Quasi-steady state (QSS)

The considerations above indicate that the time derivative of all states can be approximated to zero except the ground state and ion state:

$$\frac{\mathrm{d}N_p}{\mathrm{d}t} = 0\ (p \geq 2), \tag{2.4.1}$$

which is called the quasi-steady state (QSS). Combining Eqs. (2.2.2) and (2.2.1), the rate equations of all levels can be expressed in the matrix form:

$$\begin{pmatrix} -\zeta_2 & \zeta_{3,2} & \cdots & \zeta_{k,2} \\ \zeta_{2,2} & -\zeta_3 & & \zeta_{k,3} \\ \vdots & & \ddots & \vdots \\ \zeta_{2,k} & \zeta_{3,k} & \cdots & -\zeta_k \end{pmatrix} \begin{pmatrix} N_2 \\ N_3 \\ \vdots \\ N_k \end{pmatrix} = \begin{pmatrix} -\zeta_{1,2} \\ -\zeta_{1,3} \\ \vdots \\ -\zeta_{1,k} \end{pmatrix} N_1 + \begin{pmatrix} -\zeta_{\mathrm{ion},2} \\ -\zeta_{\mathrm{ion},3} \\ \vdots \\ -\zeta_{\mathrm{ion},k} \end{pmatrix} N_{\mathrm{i}}. \tag{2.4.2}$$

The solution of Eq. (2.4.1) is in the form:

$$\begin{aligned} N_p &= r_p^{\mathrm{rec}} Z_p N_{\mathrm{i}} N_{\mathrm{e}} + r_p^{\mathrm{io}} \frac{Z_p}{Z_1} N_1 \\ &\equiv N_p^{\mathrm{rec}} + N_p^{\mathrm{io}} \end{aligned} \tag{2.4.3a}$$

with the relationship

$$r_p^{\mathrm{rec}} + r_p^{\mathrm{io}} = 1. \tag{2.4.3b}$$

N_p^{io} and N_p^{rec} are called the ionizing and recombining plasma component, respectively. r_p^{io} and r_p^{rec} are called the population coefficients which are functions of electron density and temperature. They indicate the respect to the two thermodynamic equilibriums, respectively, of level p. For example, considering an extreme situation that a plasma has no ions and $r_p^{\mathrm{io}} = 1$, according to Eq. (2.4.3a), the populations of a certain level p have the Boltzmann distribution with respect to the ground state density. If the plasma has no ground state atoms and $r_p^{\mathrm{rec}} = 1$, the populations of level p have the Saha-Boltzmann distribution with respect to the ion and electron density. The level is in LTE. Conventionally, the method applying Eq. (2.2.2) with the assumption Eq. (2.4.1) is called the collisional-radiative model.

2.5. Ionizing plasma

2.5.1. Ionizing plasma component

The ionizing plasma component of level p ($p > 2$) is defined as:

$$N_p^{\mathrm{io}} \equiv r_p^{\mathrm{io}} \frac{Z_p}{Z_1} N_1. \tag{2.5.1}$$

According to Fujimoto [48][49], it can be divided into two phases by the N_{e} dependency. The lower-density region is called the corona phase where N_p^{io} is proportional to N_{e}. The higher-density region is called the saturation phase where the change of N_p^{io} with an increase of N_{e} is much smaller than that of the corona phase. It is hard to clearly define the boundary of the two phases, but it is found that with the increase of N_{e} higher-lying levels enter saturation phase earlier than lower-lying levels.

2.5.2. Corona phase

In the corona phase, for a certain level p, the population flux is dominated by the electron collision excitation from the ground state. The depopulation flux is mainly contributed by the radiative decay to lower levels. Thus, the ionizing plasma component of level p that is in corona phase can be estimated by:

$$N_p^{\mathrm{io}} \approx \frac{C_{1,p} N_{\mathrm{e}} N_1}{\sum_{q<p} A_{p,q}}. \tag{2.5.1}$$

2.5.3. Transition from the corona phase to the saturation phase

Between the corona and saturation phase, there exists a moment that having the following relationship in the depopulation flux:

$$\sum_{q<p} A_{p,q} \approx C_{p,p+1} N_{\mathrm{e}}. \tag{2.5.2}$$

Assuming at this N_{e}, level $p-1$ is still in the corona phase, then

$$N_1 C_{1,p} N_{\mathrm{e}} \approx N_{p-1}^{\mathrm{io}} C_{1,p-1} N_{\mathrm{e}}. \tag{2.5.3}$$

By approximately estimating the population of $p-1$ and substitute the rate coefficients [1], the relationship for Griem's boundary level is obtained by:

$$N_{\mathrm{e}} \approx \frac{1.5 \times 10^{24}}{{p_G}^{8.5}} \left(\frac{k_B T_{\mathrm{e}}}{z R_0}\right)^{1/2} z^7 [\mathrm{m}^{-3}]. \tag{2.5.4}$$

and

$$p_G \approx 480 \left(\frac{N_{\mathrm{e}}}{z^7}\right)^{-2/17}. \tag{2.5.5}$$

2.5.4. Saturation phase

In the saturation phase where N_e is higher than the Griem's boundary for level p, there is no significant change of N_p^io with an increase of N_e. The electron collision excitation from the adjacent lower-level and that to the adjacent higher-level dominate the populating and depopulating flux, respectively. The following relationship can be used to estimate the populating and depopulating flux of level p:

$$N_{p-1}^\mathrm{io} C_{p-1,p} N_\mathrm{e} \approx N_p^\mathrm{io} C_{p,p+1} N_\mathrm{e}. \tag{2.5.6}$$

The mechanism is called the ladder-like excitation. In a further higher-density region that all excited states ($p \geq 2$) are in the saturation phase, Eq. (2.5.6) can be written as:

$$N_1 C_{1,2} N_\mathrm{e} \approx N_2^\mathrm{io} C_{2,3} N_\mathrm{e} \approx N_3^\mathrm{io} C_{3,4} N_\mathrm{e} \approx \cdots . \tag{2.5.7}$$

2.5. Recombining plasma (high temperature)

2.5.1. Recombining plasma component

The recombining plasma component of level p ($p > 2$) is defined as:

$$N_p^\mathrm{rec} \equiv r_p^\mathrm{rec} Z_p N_\mathrm{i} N_\mathrm{e}. \tag{2.5.8}$$

The temperature is assumed to be high ($T_\mathrm{e}/z^2 \gg 15000$ K) in this section. In this case, both populating and depopulating fluxes are dominated by radiative processes (the radiative recombination and spontaneous transitions) at the low-density region. For high-density region, which exceeds the Griem's boundary, electron collisional processes become the dominant processes instead of radiative processes [50][51].

2.5.2. Capture radiative cascade phase

In the low-density region, the population flux is contributed by the radiative recombination and the radiative cascade from higher-lying levels; the depopulation processes are mainly the radiative decay. This situation is therefore named capture radiative cascade (CRC) phase. The following balance relation can be applied of the CRC phase:

$$N_p^{\mathrm{rec}} \approx \frac{\beta_p N_{\mathrm{i}} N_{\mathrm{e}} + \sum_{q>p} N_q^{\mathrm{rec}} A_{q,p}}{\sum_{q<p} A_{p,q}}. \tag{2.5.9}$$

By estimating N_q^{rec} with its Saha-Boltzmann value, Eq. (2.5.9) can be written as:

$$N_p^{\mathrm{rec}} \approx \frac{\left(\beta_p + \sum_{q>p} Z_q A_{q,p}\right) N_{\mathrm{i}} N_{\mathrm{e}}}{\sum_{q<p} A_{p,q}}. \tag{2.5.10}$$

In the high-temperature temperature situation, according to the approximations of β_p and $A_{p,q}$by Fujimoto[1], N_p^{rec} is given by:

$$N_p^{\mathrm{rec}} \approx Z_p N_{\mathrm{i}} N_{\mathrm{e}} \tag{2.5.11a}$$

or

$$r_p^{\mathrm{rec}} \approx 1. \tag{2.5.11b}$$

2.5.3. Transition from the CRC phase to the saturation phase

When the transition happens, by ignoring minor processes the following depopulating fluxes become equal:

$$N_p^{\mathrm{rec}} \sum_{q<p} A_{p,q} \approx N_p^{\mathrm{rec}} \sum_{q>p} C_{p,q} N_{\mathrm{e}}\,. \tag{2.5.12}$$

For populating fluxes:

$$\beta_p N_\mathrm{i} N_\mathrm{e} + \sum_{q>p} N_q^\mathrm{rec} A_{q,p} \approx \sum_{q>p} N_q^\mathrm{rec} F_{q,p} N_\mathrm{e}\,. \tag{2.5.13}$$

It is found that for, both populating and depopulating, the transition takes place almost at the same electron density, and the boundary can be estimated by Eqs. (2.5.4) and (2.5.5).

2.5.4. Saturation (LTE) phase

In the high-density region, the electron collision excitation to the higher-lying level and the electron collision ionization (depopulating) processes are almost exactly balanced by their corresponding inverse populating processes (the electron collision deexcitation and the electron three-body recombination, respectively). Then, the dominant populating balance is given by:

$$N_{p+1}^\mathrm{rec} F_{p+1,p} N_\mathrm{e} = N_p^\mathrm{rec} C_{p,p+1} N_\mathrm{e}. \tag{2.5.14}$$

Then, the population ratio is the Boltzmann distribution:

$$\frac{N_{p+1}^\mathrm{rec}}{N_p^\mathrm{rec}} = \frac{Z_{p+1}}{Z_p}. \tag{2.5.15}$$

It is also concluded that for a level in LTE:

$$N_p^\mathrm{rec} = Z_p N_\mathrm{i} N_\mathrm{e}. \tag{2.5.16}$$

2.6. Recombining plasma (low temperature)

When the temperature is low ($T_\mathrm{e}/z^2 \ll 15000\,\mathrm{K}$), only very high-lying levels have $N_p^\mathrm{rec} \approx 1$ in high densities. N_p^rec is much smaller than 1 in many cases. At low temperature, it can be also divided into the CRC phase and the saturation phase according to the dominant processes. In the CRC phase, the populations are much smaller than their Saha-Boltzmann values. In the saturation phase, the populations of higher-lying levels are close to their Saha-Boltzmann values, but the lowest-lying levels never reach the Saha-Boltzmann values [50][51][52][53][54][55].

2.6.1. CRC phase

In the CRC phase at low temperature, it is found that the magnitude of populations has weaker dependence on the levels. For higher-lying levels, the p-dependency is relatively stronger, and they are more heavily populated at low temperature than at high temperature. In the populating flux, the cascade contributes about 50 % more than its contribution in high-temperature case. The depopulating flux is contributed by radiative decay to lower-lying levels. In the highest-density region of CRC phase, the population balance can be estimated by:

$$N_p^{\mathrm{rec}} \approx \frac{N_{p+1}^{\mathrm{rec}} F_{p+1,p} N_{\mathrm{e}}}{\sum_{q<p} A_{p,q}}. \tag{2.6.1}$$

2.6.2. Saturation phase and Byron's boundary

In the saturation phase, lower-lying levels has the ladder-like deexcitation with the following balance:

$$N_{p+1}^{\mathrm{rec}} F_{p+1,p} N_{\mathrm{e}} \approx N_p^{\mathrm{rec}} F_{p,p-1} N_{\mathrm{e}}. \tag{2.6.2}$$

Higher-lying levels are in LTE with

$$F_{p,p-1} \approx C_{p,p+1}. \tag{2.6.3}$$

The boundary between them is given by:

$$p_G \approx 480\left(\frac{z^2 R_0}{3k_B T_e}\right)^{1/2}, \tag{2.6.4}$$

which is called Byron's boundary.

2.6.3. Griem's boundary

When temperature is low, the Griem's boundary lies below the Byron's boundary. In this case, the deexcitation rate coefficient can be used to determine the Griem's boundary instead of excitation rate coefficients. The approximation is given by:

$$F_{p,p-1} \approx 1.2 \times 10^{-14} p^3 \left(\frac{R_0}{p^2 k_B T_e}\right)^{0.17}. \tag{2.6.5}$$

Then,

$$p_G \approx 1.6 \times 10^{-3} / {N_\mathrm{e}}^{2/15}. \tag{2.6.6}$$

2.7. Diagram of the phases

Generally, the phases of the ionizing and recombing plasma can be illustrated as the diagram shown in Figure 6. It should be noted that in many practical situations, the electron temperature is high and ionizing plasma component is dominant; the Byron's boundary lies far below $p = 2$, and does not appear in the diagram.

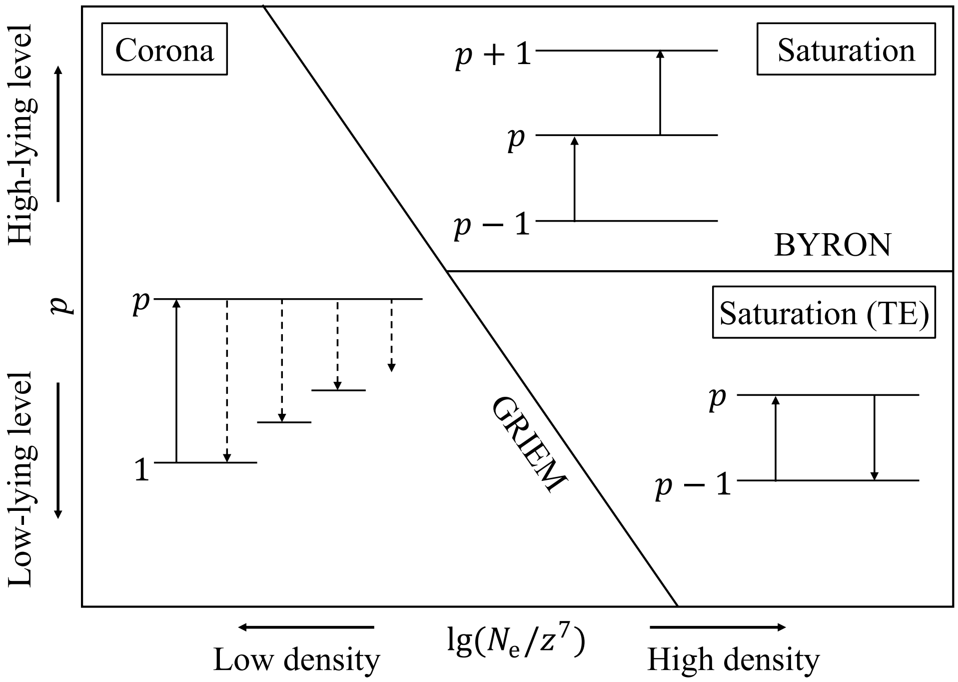

(a) Ionizing plasma component

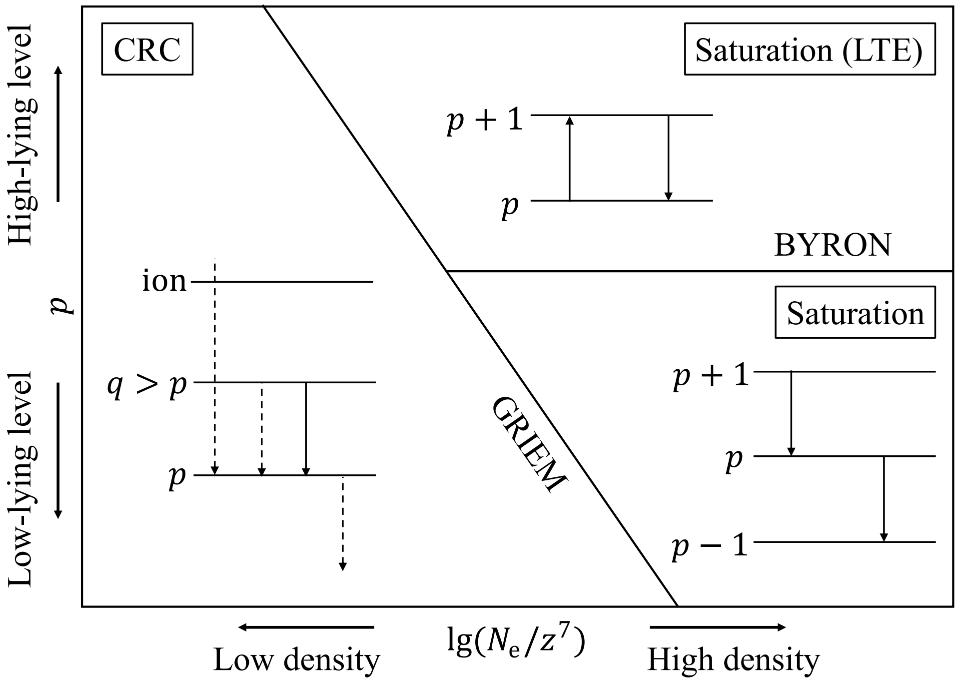

(b) Ionizing plasma component

Figure 8. (a) shows the phases in the ionizing plasma component. (b) shows the phases in the recombining plasma component. The solid lines represent collision processes and the dashed lines represents radiative processes [56].

3. MEASUREMENTS OF PLASMA PARAMETERS

This chapter provides an introduction to the theoretical foundations of plasma parameter determination through Optical Emission Spectroscopy (OES) and probe measurements.

3.1. Obtaining of Number Density in OES Measurement

For a transition from level p to q, the energy gap between the two energy levels is

$$\epsilon_{p,q} = \left|\epsilon_p^{\mathrm{ex}} - \epsilon_q^{\mathrm{ex}}\right|, \tag{3.1.1a}$$

or

$$\epsilon_{p,q} = \left|\epsilon_p^{\mathrm{io}} - \epsilon_q^{\mathrm{io}}\right|. \tag{3.1.1b}$$

The central wavelength of the emission line corresponds to the transition is given by

$$\lambda_{p,q} = \frac{hc}{\epsilon_{p,q}}, \tag{3.1.2}$$

and the corresponding photon frequency is given by

$$\nu_{p,q} = \frac{\epsilon_{p,q}}{h}, \tag{3.1.3}$$

The number density of the upper level of the transition is given by

$$N_p = \frac{\lambda_{p,q}}{hc}\frac{\Phi_{p,q}}{A_{p,q}}, \tag{3.1.4}$$

where $\Phi_{p,q}$ is spectral flux density in unit of $\mathrm{W \cdot m^{-3}}$, which can be calculated from the spectral emissivity $\varepsilon(\lambda)$ $[\mathrm{W \cdot m^{-3} \cdot sr^{-1} \cdot nm^{-1}}]$:

$$\Phi_{p,q} = 4\pi \int_{\mathrm{line}} \varepsilon(\lambda)\, d\lambda, \tag{3.1.5}$$

The line intensity of the transition is quantified by the line emissivity $\varepsilon_{p,q}$ $[\mathrm{W \cdot m^{-3} \cdot sr^{-1}}]$ [57]:

$$\varepsilon_{p,q} = N_p A_{p,q} \frac{hc}{4\pi\lambda_{p,q}} = \int_{\text{line}} \varepsilon(\lambda)\, d\lambda. \tag{3.1.6}$$

It can be also expressed as

$$\varepsilon_{p,q} = \varepsilon(\lambda) P(\lambda) \tag{3.1.7a}$$

with

$$\int_{\text{line}} P(\lambda)\, d\lambda = 1. \tag{3.1.7b}$$

The spectral radiance $L(\lambda)$ $[\mathrm{W \cdot m^{-2} \cdot sr^{-1} \cdot nm^{-1}}]$ is given by

$$L(\lambda) = \varepsilon(\lambda) \cdot x, \tag{3.1.8}$$

where x is the thickness of plasma in the direction that parallel to the measurement direction.

3.2. Continuum Spectrum Analysis

According Refs. [58][59][60], the bremsstrahlung caused by electron-atom interaction dominates the continuum spectrum. The emissivity of the continuum spectrum is given by

$$\varepsilon_{\text{ea}}(\lambda) = \sqrt{\frac{2}{m_{\text{e}}}} \frac{N_{\text{e}} N_{\text{a}}}{\lambda^2} \frac{hc}{4\pi} = \int_{h\nu}^{\infty} Q_{\text{ea}}^{\text{B}}(\lambda, \epsilon) \sqrt{\epsilon} f(\epsilon) d\epsilon. \tag{3.2.1}$$

where N_a is the atom density. $Q_{ea}^{B}(\lambda, \epsilon)$ is given with the electron-neutral momentum-transfer cross-section Q_{ea}^{mom}:

$$Q_{\text{ea}}^{\text{B}}(\lambda, \epsilon) = \frac{8\alpha_{\text{fs}}}{3\pi} \frac{\epsilon}{m_{\text{e}} c^2} \left(1 - \frac{hc}{2\lambda\epsilon}\right) \sqrt{1 - \frac{hc}{\lambda\epsilon}} Q_{\text{ea}}^{\text{mom}}(\epsilon) \tag{3.2.2a}$$

with the fine structure constant

$$\alpha_{\mathrm{fs}} = \frac{e^2}{2\epsilon_0 hc} = 7.297 \times 10^{-3}, \tag{3.2.3b}$$

where ϵ_0 is the vacuum permittivity. The momentum-transfer cross-section of the relevant gas species can be found in databases such as LXCat [61]. Electron density and temperature can be determined by fitting the measured continuum spectrum with the theoretical emissivity $\varepsilon_{\mathrm{ea}}$.

3.3. Sensitivity Calibration

In practical case, the efficiency of the spectroscopy and the geometrical efficiency must be considered. The efficiency $\eta(\lambda)$ should be determined in the calibration. Figure 9 shows the setup of the absolute calibration experiment in this study. Let $y(\lambda)$ be the count number obtained in the measurement, then the spectral radiance is given by

$$L(\lambda) = \frac{y(\lambda) h\nu}{\eta(\lambda) S_{\mathrm{lum}} \Delta\Omega}, \tag{3.2.1}$$

where S_{lum} and $\Delta\Omega$ are the luminous area observed from the fiber head and the solid angle, respectively. $\Delta\Omega$ can be calculated by

$$\Delta\Omega = \frac{S_{\mathrm{rec}}}{r^2}, \tag{3.2.2}$$

where S_{rec} is the light receiving area of the fiber head. In the case of Figure 9:

$$\Delta\Omega_1 = \frac{S_2}{{r_1}^2}, \tag{3.2.3a}$$

and

$$S_2 = S_1 \cos\theta, \tag{3.2.3b}$$

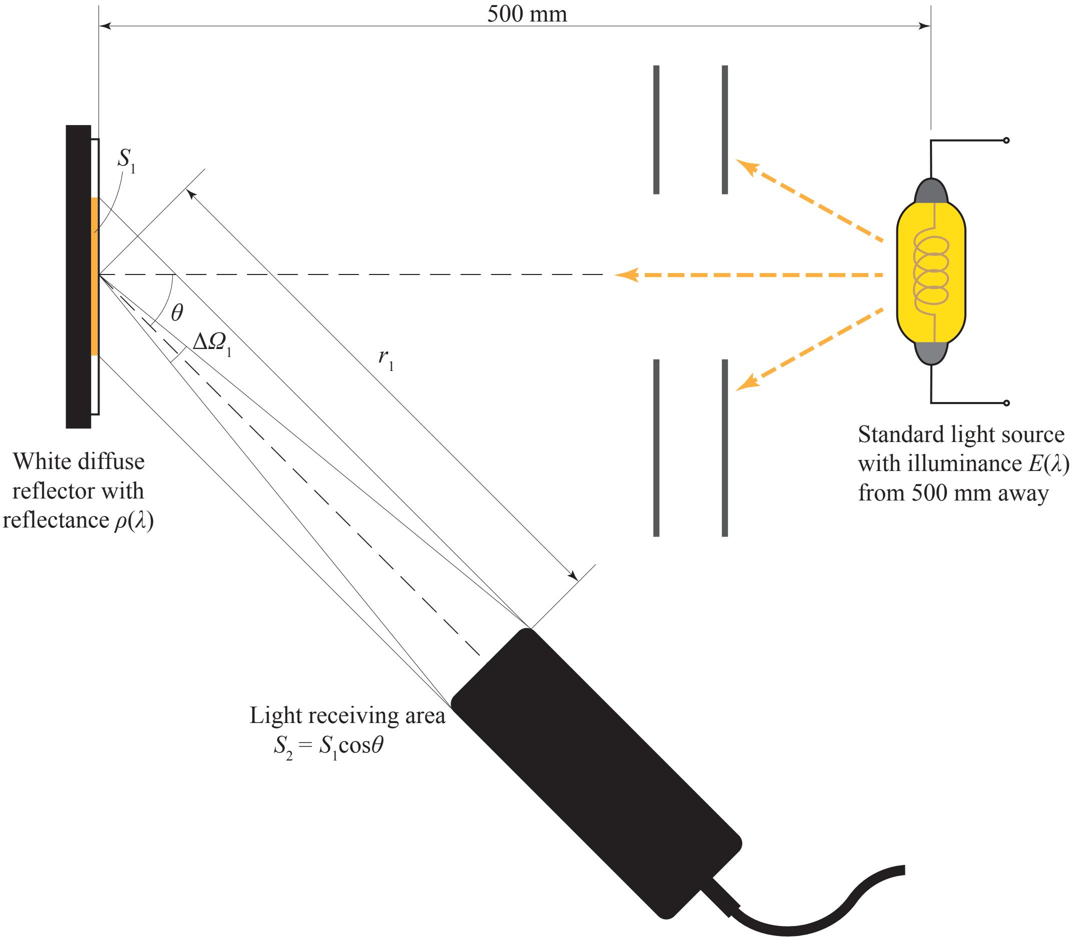

Figure 9. Optical setup of the absolute calibration.

The efficiency is given by

$$\eta(\lambda) = \frac{hc}{\lambda} \frac{\pi r_1{}^2}{S_1 S_2 \cos\theta} \frac{y_{\text{cali}}(\lambda)}{\rho(\lambda)E(\lambda)}, \tag{3.2.4a}$$

where $y_{\text{cali}}(\lambda)$ is the count number obtained in the calibration, $\rho(\lambda)$ is the reflectance of the reflector, and $E(\lambda)$ $[\mathrm{W \cdot m^{-2} \cdot nm^{-1}}]$is the illuminance of the standard light source with from 500 mm away with the relationship:

$$E(\lambda)\rho(\lambda) = \frac{\pi L(\lambda)}{\eta(\lambda)}. \tag{3.2.4b}$$

The parameters of the reflector and standard light source are shown in Table 8 and Figure 10.

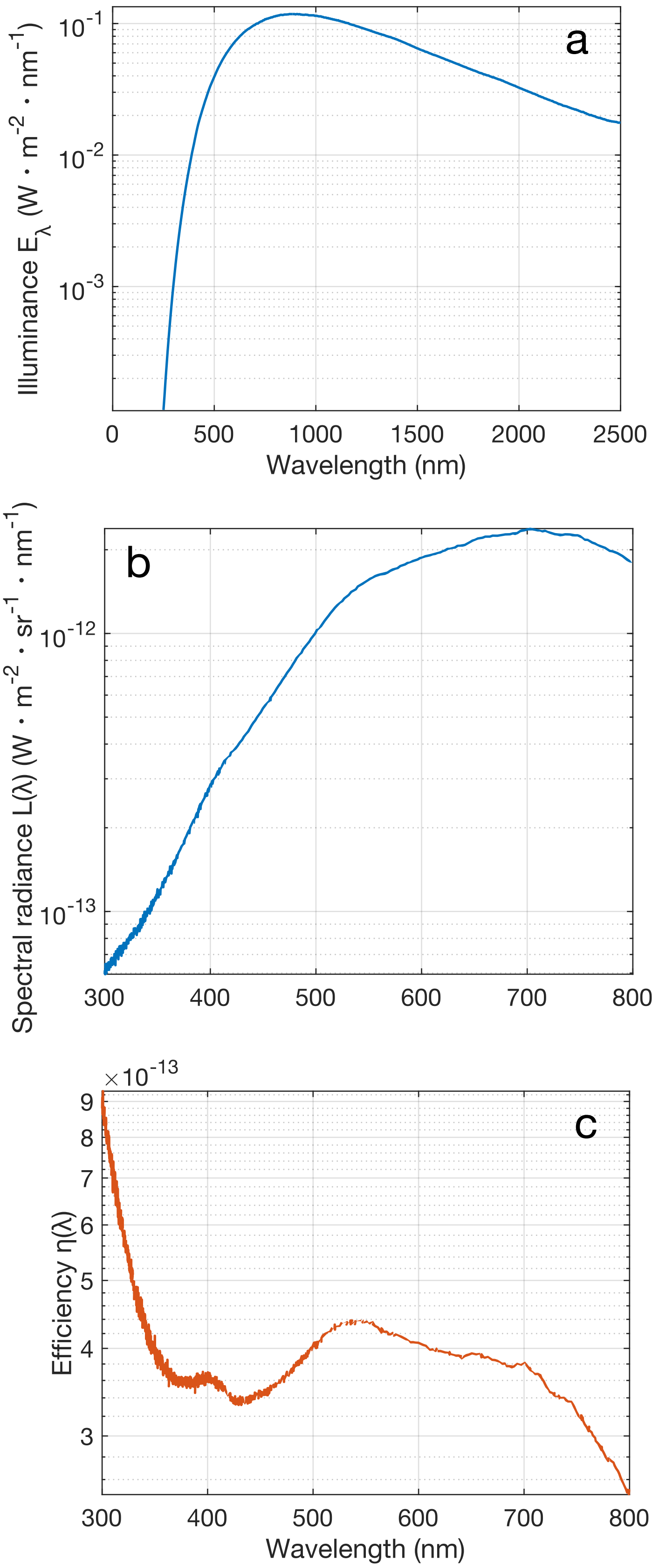

Figure 10. (a) Illuminance $E(\lambda)$ of the standard light source. Obtained spectral radiance $L(\lambda)$ in the absolute calibration. Calculated efficiency $\eta(\lambda)$.

Table 8 (a). Information of the standard light source.

Maker	Ushio lighting
Type	JPD100V500WCS
Series number	2103005
Calibration method	CL-C-60-7
Calibration date	2021.12.16

(b). Parameters of standard reflectance.

Provider	Zenith Polymer
Standard pore sizes	$1-20\ \mu\mathrm{m}$
Surface roughness	$3-25\ \mu\mathrm{m}$
Effective spectral range	$260-2500$ nm
Reflectance ($350-1500$ nm)	$>99\%$
Reflectance ($1500-2500$ nm)	$>95\%$
Absorbance (above 2700 nm)	$<20\%$
None absorption bands	$250-2500$ nm
Laser damage threshold	$7\ \mathrm{J/cm^2}$

3.4. Helium Line Spectrum

An example of the measured line spectrum is shown in Figure 11.

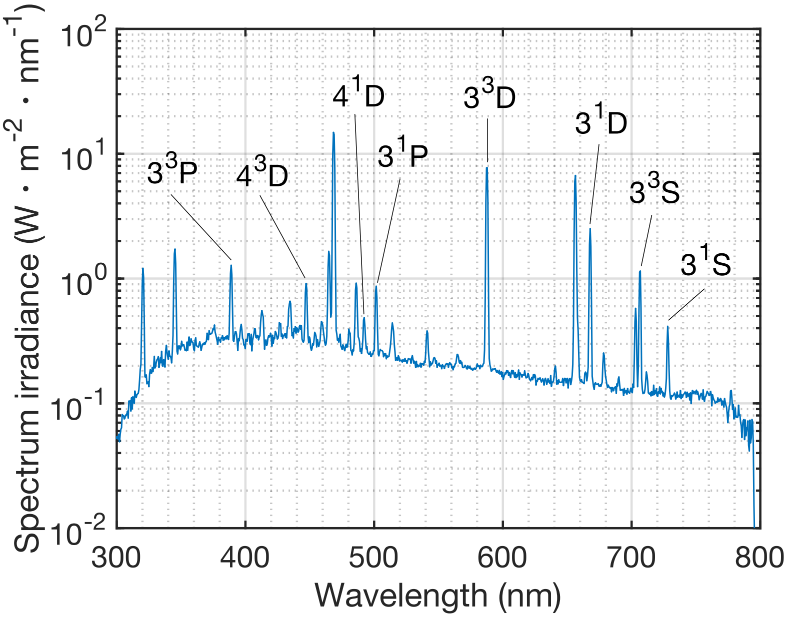

Figure 11. The spectrum of the LHD helium plasma in the visible wavelength range.

Eight emission lines of neutral helium can be identified. Table 9 shows the parameters of the emission lines examined.

Table 9. Helium lines used for line spectrum analysis.

Level p	Wavelength $\lambda_{p,q}$ (nm)	Transition ($n^{2S+1}L \rightarrow n'^{2S'+1}L'$)	Rate coefficient $A_{p,q}$ (s^{-1})
6	728.135	$3^1\mathrm{S} \rightarrow 2^1\mathrm{P}$	1.8291×10^7
7	706.525	$3^3\mathrm{S} \rightarrow 2^3\mathrm{P}$	2.7849×10^7
8	501.568	$3^1\mathrm{P} \rightarrow 2^1\mathrm{S}$	1.3368×10^7
9	388.864	$3^3\mathrm{P} \rightarrow 2^3\mathrm{S}$	0.9472×10^7
10	667.815	$3^1\mathrm{D} \rightarrow 2^1\mathrm{P}$	6.3676×10^7
11	587.566	$3^3\mathrm{D} \rightarrow 2^3\mathrm{P}$	7.0693×10^7
16	492.193	$4^1\mathrm{D} \rightarrow 2^1\mathrm{P}$	1.9855×10^7
17	447.150	$4^3\mathrm{D} \rightarrow 2^3\mathrm{P}$	2.4574×10^7

3.5. Probe Measurement

The double probe method is applied in the low-pressure microwave discharged experiment. It diagnoses the electron temperature and density of plasma by the *I-V* characteristics between two probes. Figure 12 shows the parameters in the double probe measurement experiment [62][63][64].

According to the *I-V* characteristics of the probe, the electron temperature in *V* can be calculated by

$$T_{\mathrm{e}}\ [V] = \frac{I_{\mathrm{d}_0}}{A_1 \left(\frac{\mathrm{d}I_{\mathrm{d}}}{\mathrm{d}V_{\mathrm{d}}}\right)_{V_{\mathrm{d}}=0} - A_2 \left(\frac{\mathrm{d}I_{\mathrm{d}}}{\mathrm{d}V_{\mathrm{d}}}\right)_{V_{\mathrm{d}}>>0}}, \tag{2.4.1}$$

where $\mathrm{d}I_{\mathrm{d}}/\ \mathrm{d}V_{\mathrm{d}}$ can be considered as the slope of the $I_{\mathrm{d}}-V_{\mathrm{d}}$ plot, I_{d_0} is the current when $V_{\mathrm{d}} = 0$, for $(\mathrm{d}I_{\mathrm{d}}/\ \mathrm{d}V_{\mathrm{d}})_{V_{\mathrm{d}}>>0}$, the average value of the slope of saturation region in the two sides of Figure 11 (b) is used. A_1 and A_2 are set as 2 and 1.64, respectively. Then, electron density is given by

$$N_{\mathrm{e}} = \frac{I_{\mathrm{d0}}}{6.05eS_{\mathrm{prob}}}\left(\frac{eT_{\mathrm{e}}}{m_{\mathrm{i}}}\right)^{-1/2}, \tag{2.4.16}$$

where S_{prob} is the surface area of the probe. A power source is applied to generate DC voltage from -25 to 25 V. The electron density and temperature is obtained by taking the mean value of several measurements.

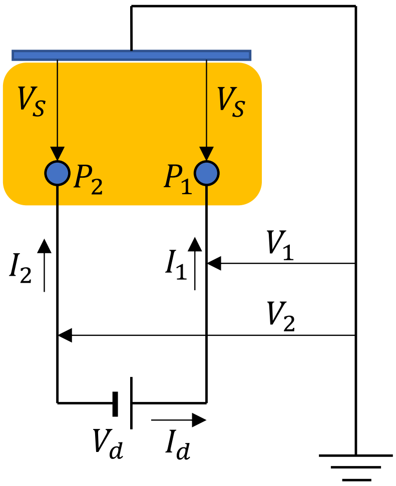

(a) Circuit of double probe.

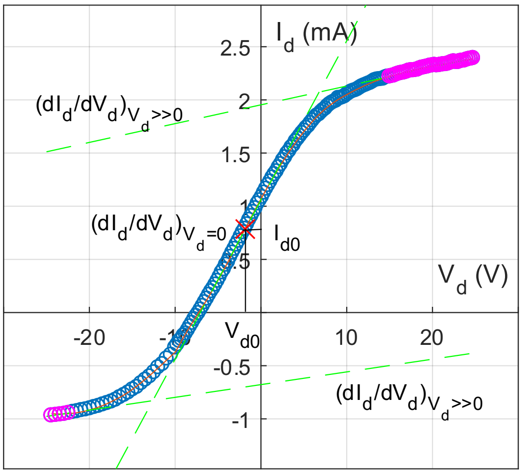

(b) Analysis of result obtained by probe method.

Figure 12. Parameters in the probe measurement.

4. OES DIAGNOSTICS OF LOW-PRESSURE MICROWAVE INDUCED HELIUM PLASMA BASED ON DOMINANT PROCESSES ANALYSIS OF CR MODEL

In this chapter, a method that determine the electron density and temperature of low-pressure microwave induced helium plasma based on a simplified CR model will be illustrated. The dominant processes of the low-pressure helium CR model were analysed and extracted. Then, the OES measurement was applied with the simplified model that only includes dominant processes to determine the electron density and temperature.

4.1. Analysis of Populating and Depopulating Processes

The low-pressure helium CR model developed by Fujimoto [24] is used for analysis. Other atomic collision processes were neglected. As shown in Figure 11, there are eight levels of neutral helium (3^1S, 3^3S, 3^1P, 3^3P, 3^1D, 3^3D, 4^1D, and 4^3D) can be measured in the visible wavelength range. The processes in the populating and depopulating of these levels in the CR model were investigated. It was found the populating and depopulating processes of level 3^1S, 3^3S, and 3^1D have relatively simple structure. Figures 13 – 15 show the diagram of the processes of these levels in different condition.

(a) Populating (T_e = 1 eV) (b) depopulating (T_e = 1 eV)

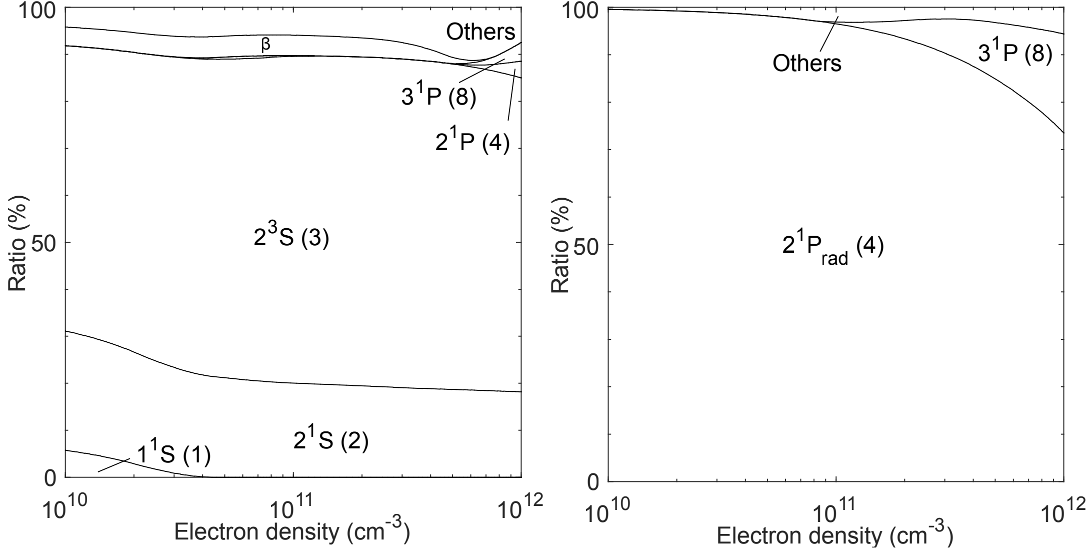

(c) Populating (T_e = 4 eV) (d) Depopulating (T_e = 4 eV)

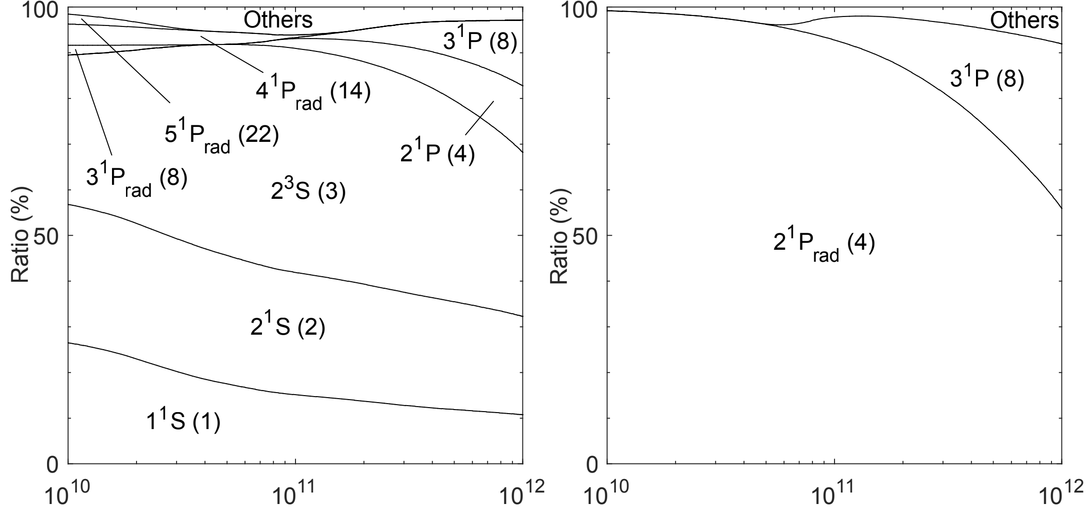

Figure 13. Population flow of 3^1S (p = 6), (a) and (b) show the populating and depopulating processes, respectively, with T_e = 1 eV. (c) and (d) show the populating and depopulating processes, respectively, with T_e = 4 eV.

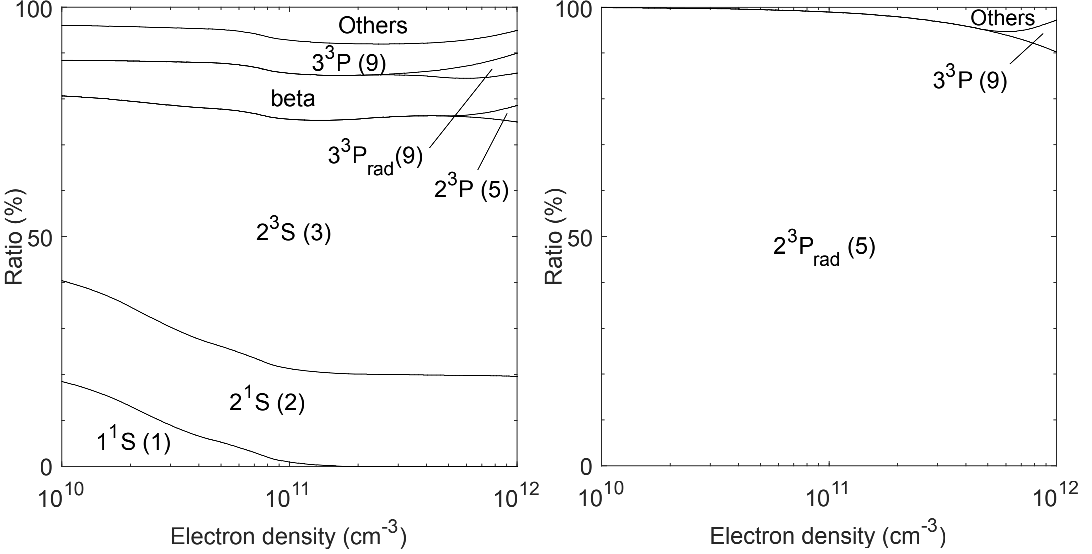
(a) Populating (T_e = 1 eV)

(b) depopulating (T_e = 1 eV)

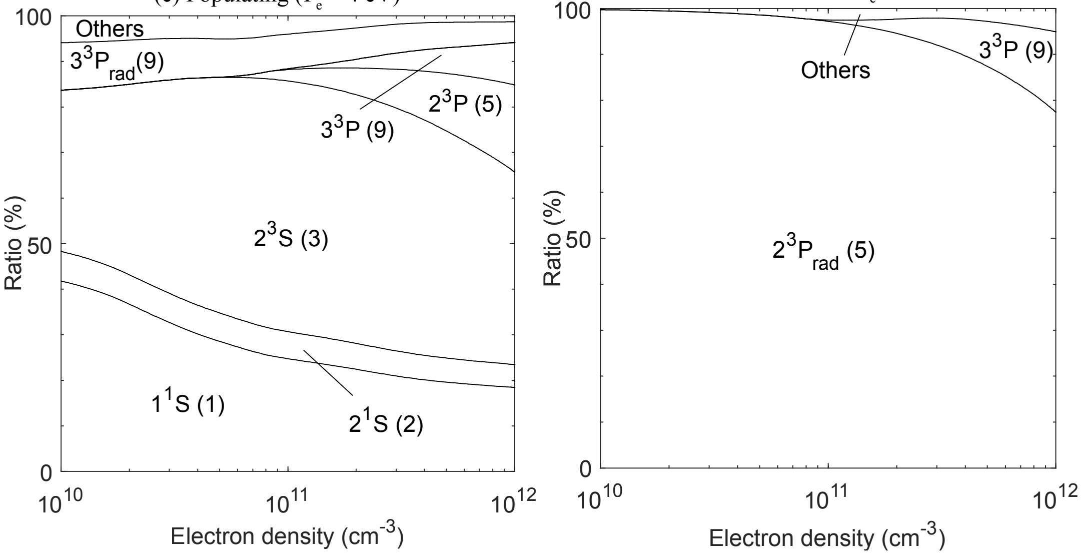
(c) Populating (T_e = 4 eV)

(d) Depopulating (T_e = 4 eV)

Figure 14. Population flow of 3^3S (p = 7), (a) and (b) show the populating and depopulating processes, respectively, with T_e = 1 eV. (c) and (d) show the populating and depopulating processes, respectively, with T_e = 4 eV.

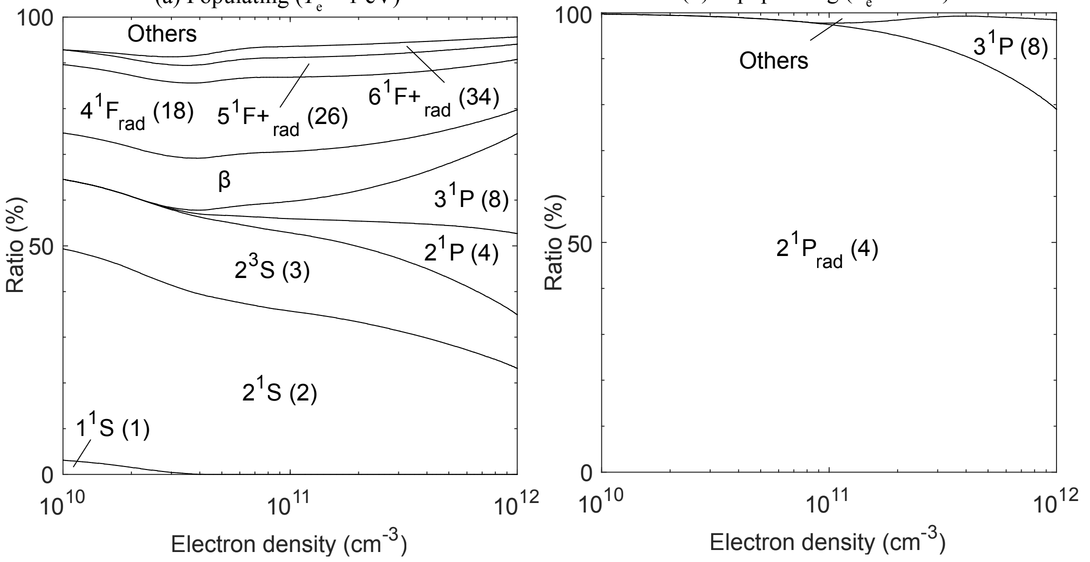
(a) Populating (T_e = 1 eV)

(b) depopulating (T_e = 1 eV)

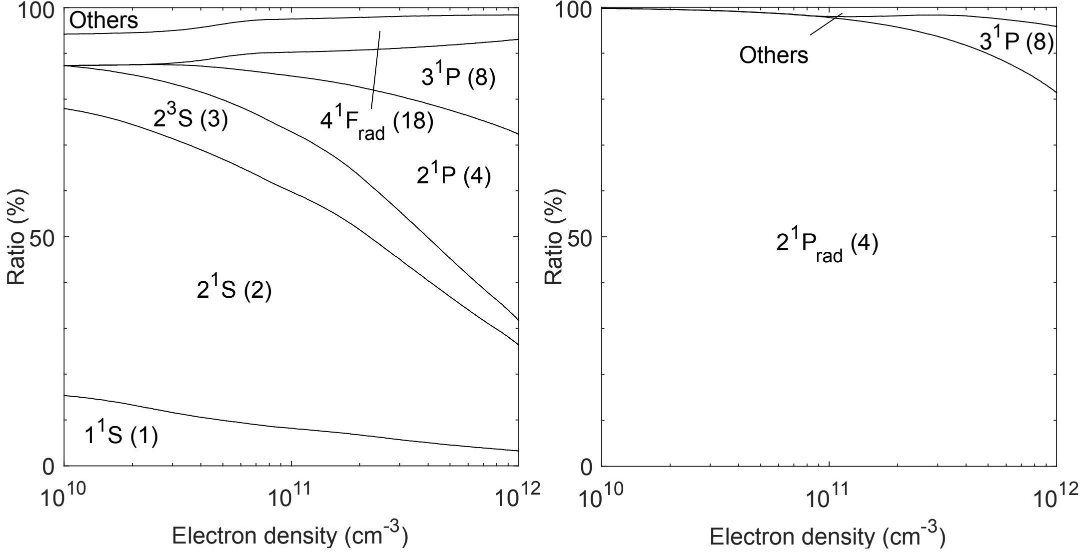
(c) Populating (T_e = 4 eV)

(d) Depopulating (T_e = 4 eV)

Figure 15. Population flow of 3^1D (p = 10), (a) and (b) show the populating and depopulating processes, respectively, with T_e = 1 eV. (c) and (d) show the populating and depopulating processes, respectively, with T_e = 4 eV.

For level $3^1\mathrm{S}$, when $T_\mathrm{e} = 1$ eV, excitations from the level $2^1\mathrm{S}$ and $2^3\mathrm{S}$ induced by electron collisions dominate the flow in population process. Ratio of the dominant processes does not change so much with the increase of electron density. Ratio of the dominant processes occupy over 80% of the populating flux. Radiative decay to $2^1\mathrm{P}$ state dominates the depopulating process, when electron temperature is low ($N_\mathrm{e} < 10^{11}\ \mathrm{cm}^{-3}$). It occupies over 95% of the depopulating flux. When electron temperature is larger than $10^{11}\ \mathrm{cm}^{-3}$, electron collision deexcitation from level $3^1\mathrm{P}$ keeps becoming larger with the increase of electron density. It is neglected because its largest ratio is less than 20 %. When $T_\mathrm{e} = 4$ eV, there are eight processes occupy over 1 % of the populating flux. It can be still considered that the electron collision excitation from the level $2^1\mathrm{S}$ and $2^3\mathrm{S}$ dominate the populating process. Radiative decay to level $2^1\mathrm{P}$ dominates the depopulating process, and its ratio drops to 56% when $N_\mathrm{e} = 10^{12}\ \mathrm{cm}^{-3}$.

For level $3^3\mathrm{S}$, when $T_\mathrm{e} = 1\ \mathrm{eV}$, the electron collision excitation from level $2^3\mathrm{S}$ dominates the populating process. Radiative decay to level $2^3\mathrm{P}$ dominates the depopulating process with the ratio larger than 90%. When $T_\mathrm{e} = 4$ eV, it is considered the dominant processes same as the processes when $T_\mathrm{e} = 1$ eV. Although, the electron collision excitation from $1^1\mathrm{S}$ occupies over 40% populating flux when $N_e = 10^{11}\ \mathrm{cm}^{-3}$, including it will increase number of the variables and make the calculation more complex. In addition, it can be neglected when the electron temperature is low. Therefore, the electron collision excitation from $1^1\mathrm{S}$ is neglected.

For level 3^1D, the electron collisional excitation from levels 2^1S and 2^3S are the dominant processes at low electron density region ($10^{10} < N_\text{e} < 10^{11}$ cm^{-3}) in both Figures 15 (a) and (c). The ratio of the two levels is larger than 50%. When $10^{11} < N_\text{e} < 10^{12}$ cm^{-3}, the ratio of them decrease to approximately 35%. The electron collisional excitation from level 2^1P cannot be neglected in this region. Therefore, electron collisional excitation from levels 2^1S, 2^3S, and 2^1P dominate the populating process. The spontaneous transition to level 2^1P is the dominant process and its ratio is always larger than 79%.

According to the analysis above, the populating of levels 3^1S, 3^3S, and 3^1D is basically dominated by the electron collision excitation from level 2^1S and 2^3S, whose number density cannot be directly obtained by OES measurement. To express the number density of them by other levels that can be measured by OES method, the population and depopulation of level 2^1S, 2^3S, and 2^1P are also analyzed. The diagrams are shown in Figures 16 – 18.

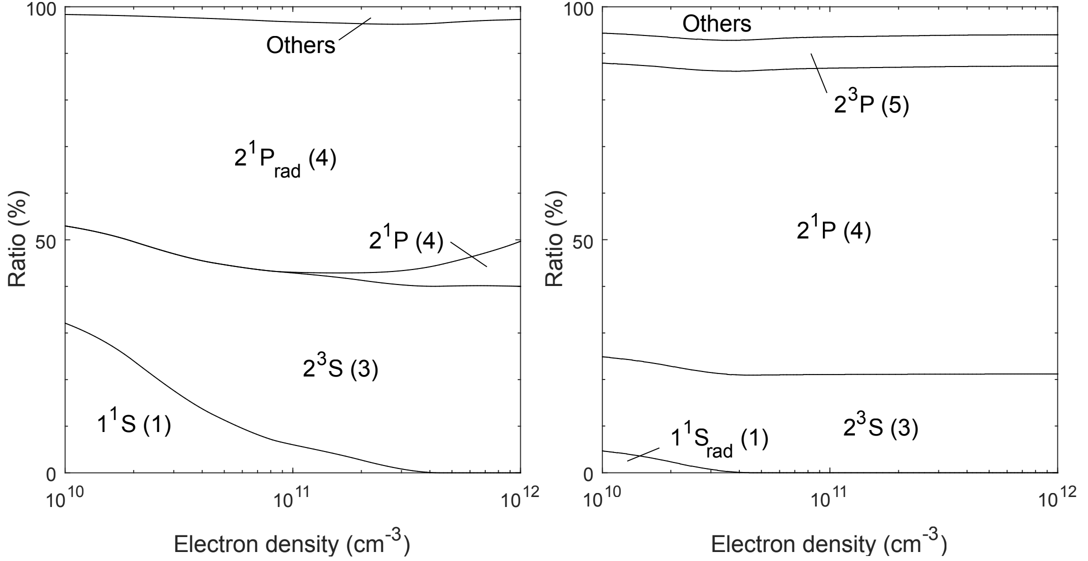
(a) Populating (T_e = 1 eV)

(b) Depopulating (T_e = 1 eV)

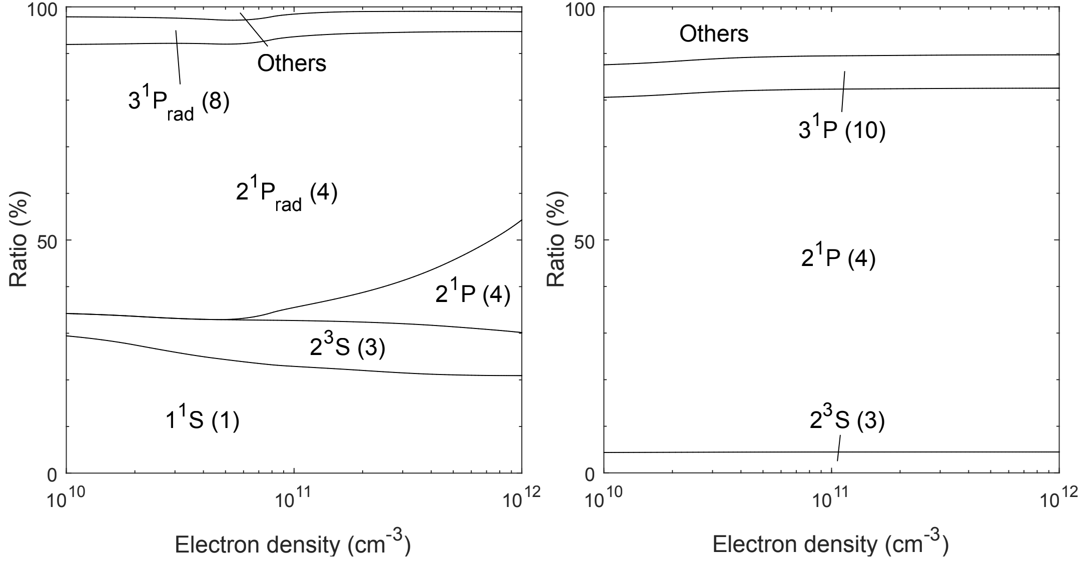
(c) Populating (T_e = 4 eV)

(d) Depopulating (T_e = 4 eV)

Figure 16. Population flow of 2^1S (p = 2), (a) and (b) show the populating and depopulating processes, respectively, with T_e = 1 eV. (c) and (d) show the populating and depopulating processes, respectively, with T_e = 4 eV.

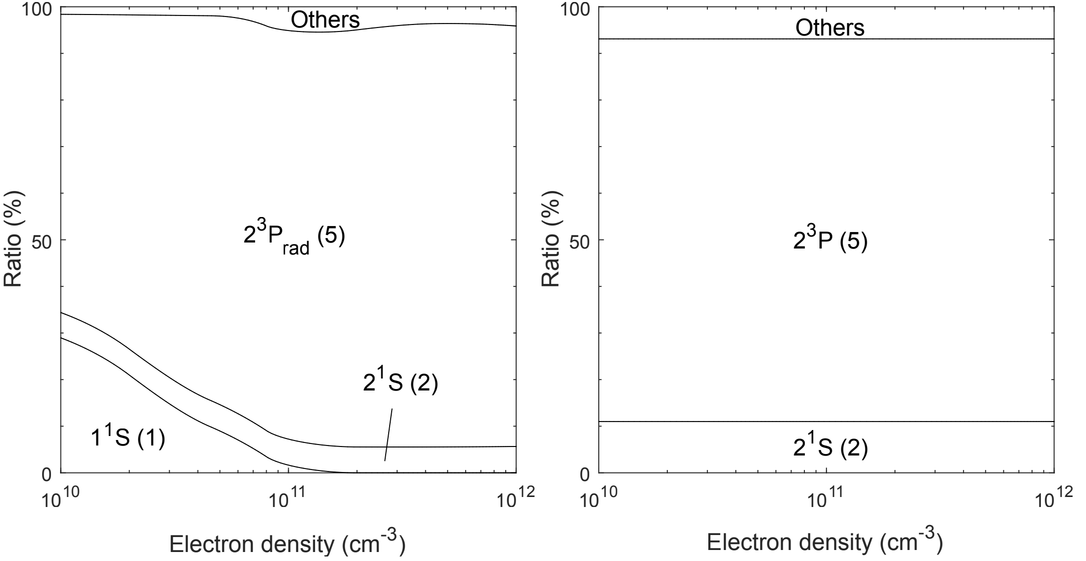
(a) Populating (T_e = 1 eV)

(b) Depopulating (T_e = 1 eV)

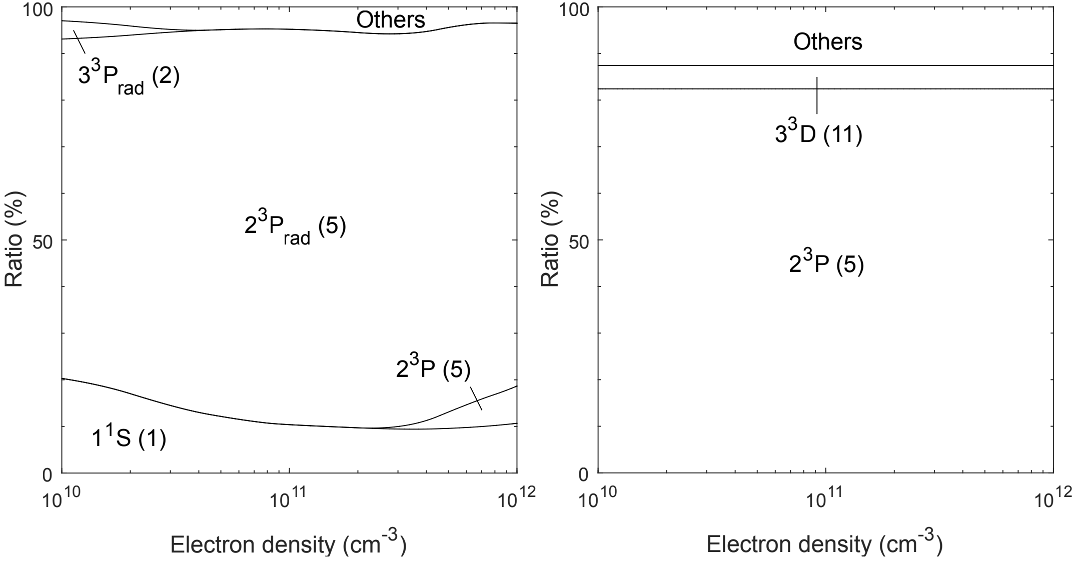
(c) Populating (T_e = 4 eV)

(d) Depopulating (T_e = 4 eV)

Figure 17. Population flow of 2^3S (p = 3), (a) and (b) show the populating and depopulating processes, respectively, with T_e = 1 eV. (c) and (d) show the populating and depopulating processes, respectively, with T_e = 4 eV.

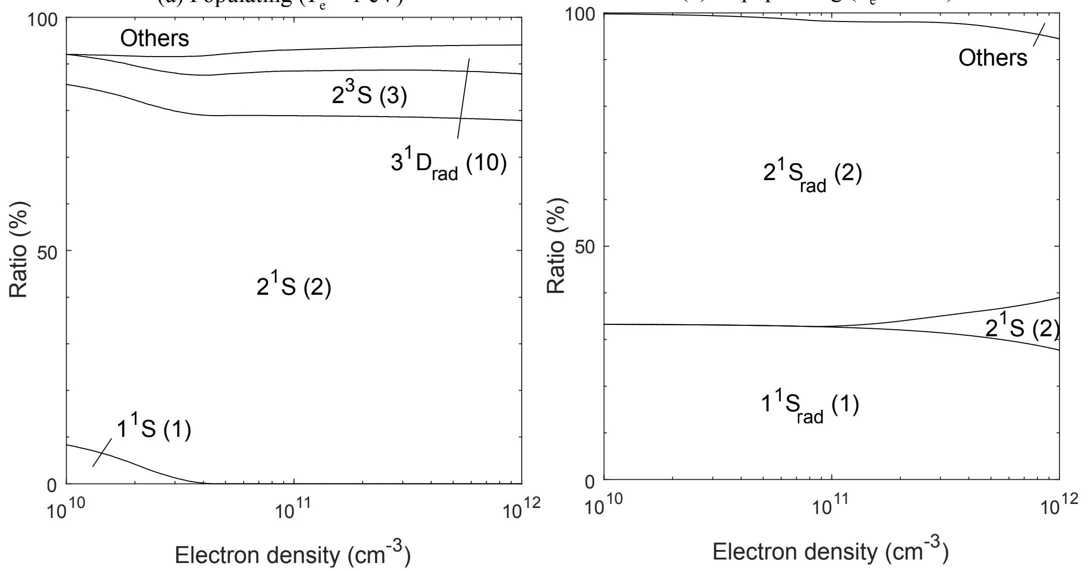

(a) Populating (T_e = 1 eV)

(b) Depopulating (T_e = 1 eV)

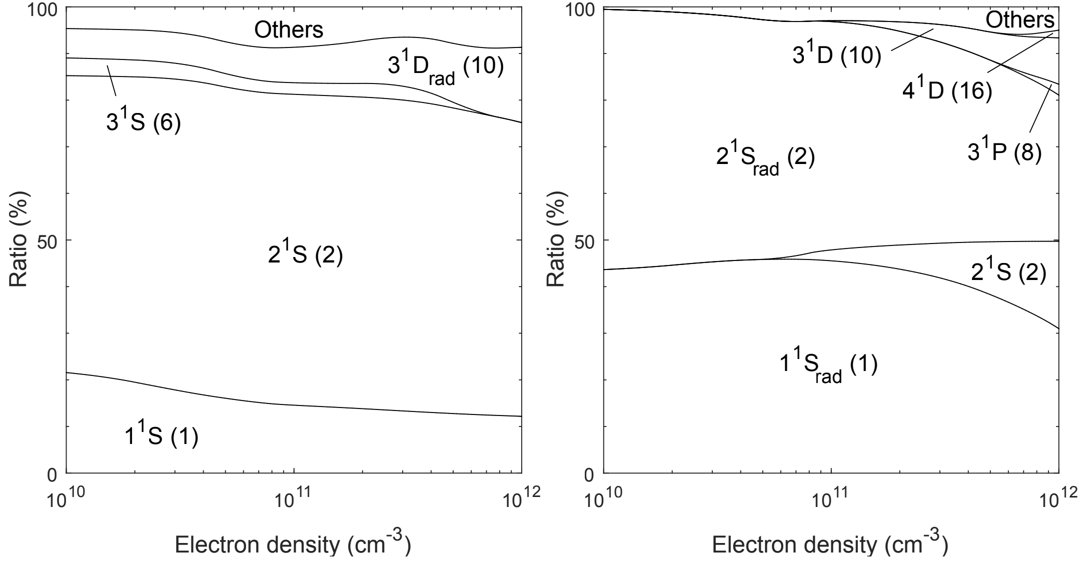

(c) Populating (T_e = 4 eV)

(d) Depopulating (T_e = 4 eV)

Figure 18. Population flow of 2^1P (p = 4), (a) and (b) show the populating and depopulating processes, respectively, with T_e = 1 eV. (c) and (d) show the populating and depopulating processes, respectively, with T_e = 4 eV.

4.2. Rate Equations (Simplified)

Based on the extracted dominant processes in the previous chapter, the following rate equations can be constructed as a simplified model of excitation kinetics.

4.2.1. Rate equation of the level 3^1S

Figure 19 shows the simplified processes of the level 3^1S.

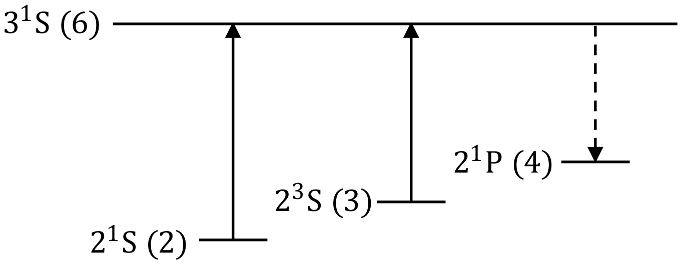

Figure 19. Simplified dominant population and depopulation processes of the level 3^1S (p = 6).

Based on the figure, the corresponding rate equation is given by

$$N_2 C_{2,6} N_{\mathrm{e}} + N_3 C_{3,6} N_{\mathrm{e}} = N_6 A_{6,4}. \tag{4.2.1}$$

4.2.2. Rate equation of the level 3^3S

Figure 20 shows the simplified processes of the level 3^3S.

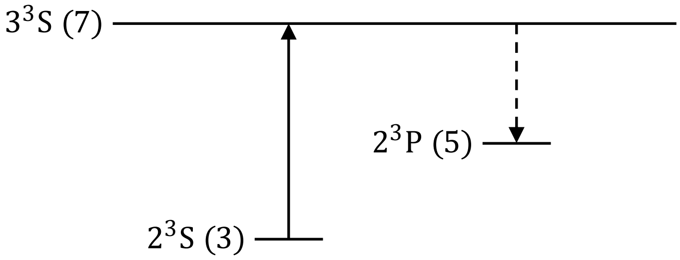

Figure 20. Simplified dominant population and depopulation processes of the level 3^3S (p = 7).

Based on the figure, the corresponding rate equation is given by

$$N_3 C_{3,7} N_\mathrm{e} = N_7 A_{7,5}. \tag{4.2.2}$$

4.2.3. Rate equation of the level 3^1D

Figure 21 shows the simplified processes of the level 3^1D.

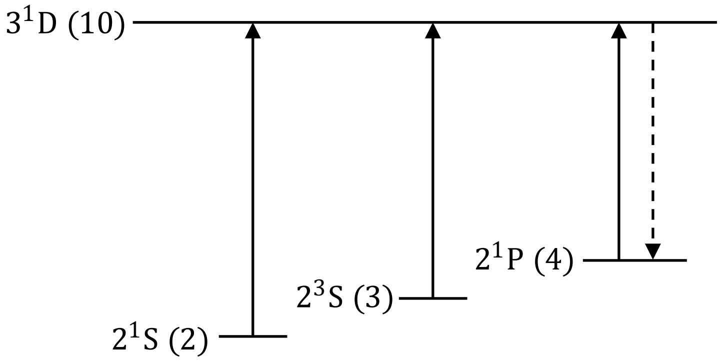

Figure 21. Simplified dominant population and depopulation processes of the level 3^1D (p = 10).

Based on the figure, the corresponding rate equation is given by

$$N_2 C_{2,10} N_\mathrm{e} + N_3 C_{3,10} N_\mathrm{e} + N_4 C_{4,10} N_\mathrm{e} = N_{10} A_{10,4}. \tag{4.2.3}$$

4.2.4. Rate equation of the level 2^1S

Figure 22 shows the simplified processes of the level 2^1S.

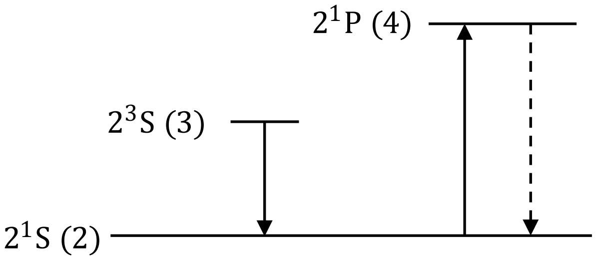

Figure 22. Simplified dominant population and depopulation processes of the level 2^1S ($p = 2$).

Based on the figure, the corresponding rate equation is given by

$$N_3 F_{3,2} N_\mathrm{e} + N_4 A_{4,2} = N_2 C_{2,4} N_\mathrm{e}. \tag{4.2.4}$$

4.2.5. Rate equation of the level 2^3S

Figure 23 shows the simplified processes of the level 2^3S.

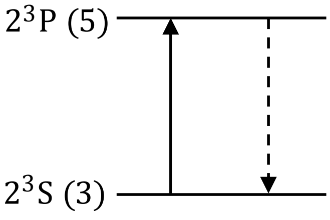

Figure 23. Simplified dominant population and depopulation processes of the level 2^3S ($p = 3$).

Based on the figure, the corresponding rate equation is given by

$$N_5 A_{5,3} = N_3 C_{3,5} N_\mathrm{e}. \tag{4.2.5}$$

Because N_5 cannot be measured, the rate equation of the level 2^3S has not been used for solving the electron density and temperature

4.2.6. Rate equation of the level 3^1P

Figure 24 shows the simplified processes of the level 2^1P.

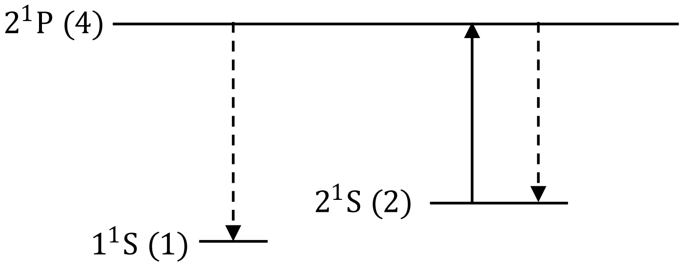

Figure 24. Simplified dominant population and depopulation processes of the level 2^1P ($p = 4$).

Based on the figure, the corresponding rate equation is given by

$$N_2 C_{2,4} N_e = N_4 A_{4,1} + N_4 A_{4,2}. \tag{4.2.6}$$

4.2.7. Solving T_e and N_e

By substituting the term $N_2 C_{2,4} N_e$ in Eq. (4.2.4) with Eq. (4.2.6),

$$N_3 F_{3,2} N_e = N_4 A_{4,1}. \tag{4.2.7}$$

Eq. (4.2.2) can be written as

$$N_3 = \frac{N_7 A_{7,5}}{C_{3,7} N_e}. \tag{4.2.8}$$

Combining Eqs. (4.2.7) and (4.2.8) yields

$$N_4 = \frac{N_7 F_{3,2} A_{7,5}}{C_{3,7} A_{4,1}}. \tag{4.2.9}$$

According to Eq. (4.2.1), N_2 can be expressed as

$$\begin{aligned} N_2 &= \frac{N_6 A_{6,4} - N_3 C_{3,6} N_\mathrm{e}}{C_{2,6} N_\mathrm{e}} \\ &= \frac{N_6 A_{6,4}}{C_{2,6} N_\mathrm{e}} - \frac{N_7 C_{3,6} A_{7,5}}{C_{2,6} C_{3,7} N_\mathrm{e}}. \end{aligned} \tag{4.2.10}$$

Substituting N_2, N_3, and N_4 into Eq. (4.2.10) yields

$$\frac{N_6 C_{2,10} A_{6,4}}{C_{2,6}} - \frac{N_7 C_{2,10} C_{3,6} A_{7,5}}{C_{2,6} C_{3,7}} + \frac{N_7 C_{3,10} A_{7,5}}{C_{3,7}} + \frac{N_7 F_{3,2} C_{4,10} A_{7,5} N_\mathrm{e}}{C_{3,7} A_{4,1}} = N_{10} A_{10,4}. \tag{4.2.11}$$

Since all the rate coefficients in Eq. (4.2.11) can be calculated after T_e is known, T_e and N_e can be determined by finding the global minimum of the following function:

$$\begin{aligned} f_\mathrm{dom}(T_\mathrm{e}, N_\mathrm{e}) &= N_6 \frac{C_{2,10} A_{6,4}}{C_{2,6}} - N_7 \frac{C_{2,10} C_{3,6} A_{7,5}}{C_{2,6} C_{3,7}} + N_7 \frac{C_{3,10} A_{7,5}}{C_{3,7}} \\ &+ N_7 \frac{F_{3,2} C_{4,10} A_{7,5}}{C_{3,7} A_{4,1}} N_\mathrm{e} - N_{10} A_{10,4}. \end{aligned} \tag{4.2.12}$$

4.3. Microwave Induced Low-Pressure Discharged Helium Plasma

The equipment for generating microwave induced low-pressure discharged helium plasma is shown in the following figure. Helium gas in the discharge tube is induced by microwave. The measurements of probe and spectroscopy are taken at the same position. The frequency of generated microwave is 2.45 GHz in this study [65]. The following table shows the information of the microwave generator.

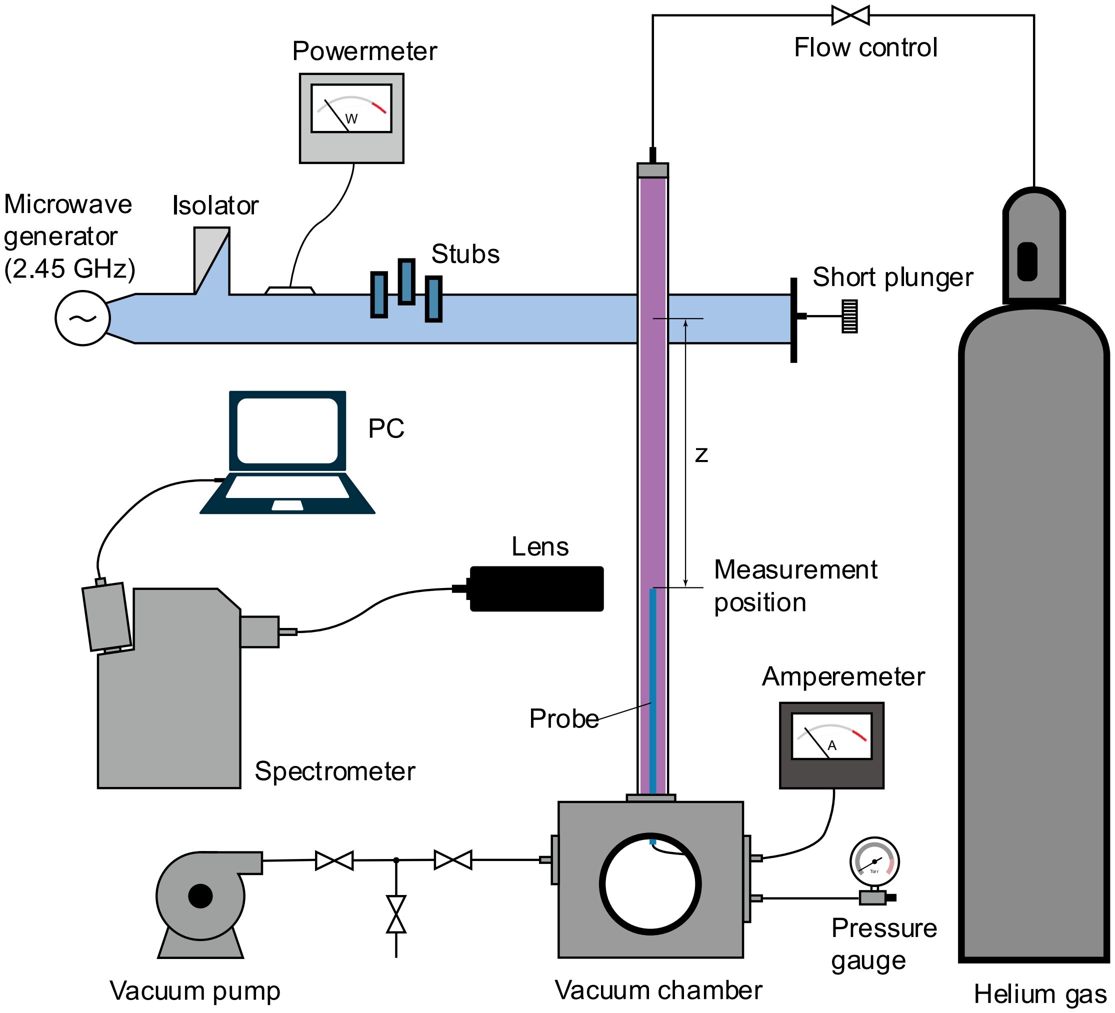

Figure 25. Layout of the low-pressure microwave helium discharge system. The measurement position *z* is the distance from the centre of the wave guide to the position where the plasma is measured.

Table 10. Information of the microwave generator and its related equipment.

Microwave generator	TOSHIBA TNG-491C
Waveguide	TOSHIBA BRJ-2
Isolator	TOSHIBA TMU-261B
Power monitor	TOSHIBA TMU-613A
Stubs	TOSHIBA TMU224A

A gas pump is applied to keep the pressure in the vacuum chamber at 1 Torr. Its parameters are shown in the following table.

Table 11. Information of the vacuum pump, pressure gauge, and power supply.

Pump	ALCATEL 2025SD
Pressure Gauge	MKS Instruments Japan 622A
Power Supply	MKS Instruments Japan PDR-D-1

4.4. Results and Discussion (Simplified CR model)

4.4.1. Theoretical error

A group of number densities were calculated by the CR model with the preset electron density N_{e_0} and electron temperature T_{e_0}. These calculated number densities were used for determining the electron density N_{e_1} and electron temperature T_{e_1}. The comparison between the obtained results and their corresponding original value are shown in Figure 26.

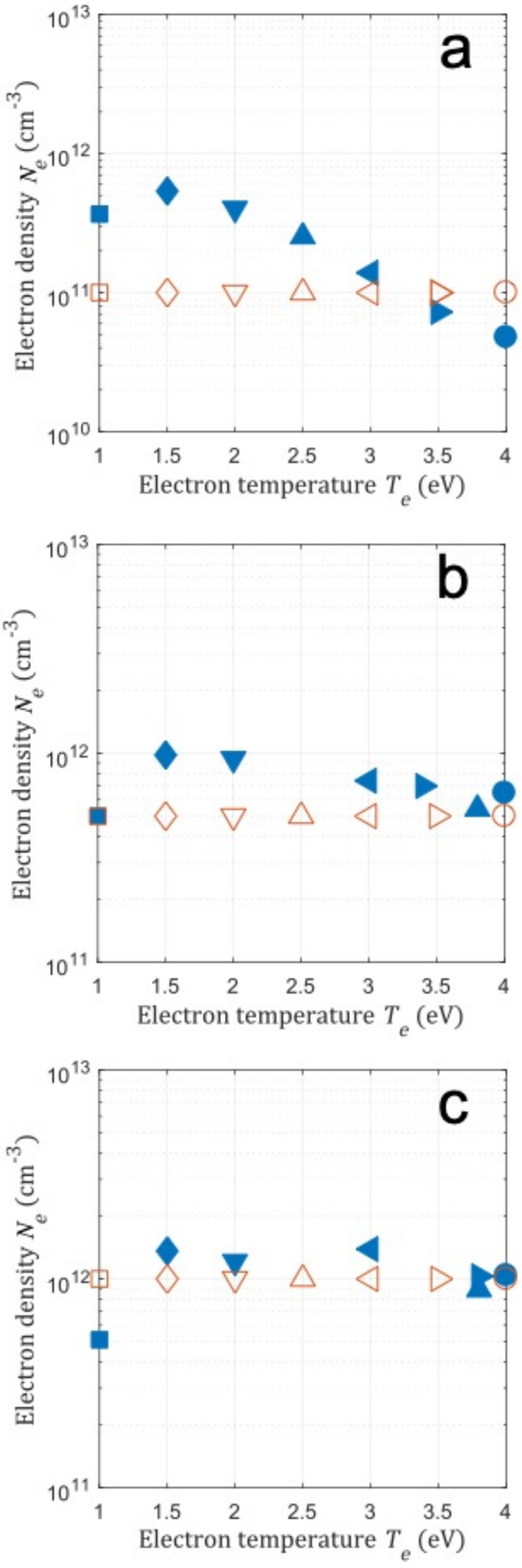

Figure 26. The comparison of the preset data and the calculated data. The orange hollow symbols represent (T_{e0}, N_{e0}), and the blue solid symbols represent (T_{e1}, N_{e1}).

The values of the preset data are shown in Table 12.

Table 12. Preset values of electron density and temperature.

T_{e_0} (eV)	$N_{e_0}(\mathrm{cm^{-3}})$	T_{e_0} (eV)	$N_{e_0}(\mathrm{cm^{-3}})$	T_{e_0} (eV)	$N_{e_0}(\mathrm{cm^{-3}})$
1.0	10^{11}	1.0	5×10^{11}	1.0	10^{12}
1.5	10^{11}	1.5	5×10^{11}	1.5	5×10^{11}
2.0	10^{11}	2.0	5×10^{11}	2.0	5×10^{11}
2.5	10^{11}	2.5	5×10^{11}	2.5	5×10^{11}
3.0	10^{11}	3.0	5×10^{11}	3.0	5×10^{11}
3.5	10^{11}	3.5	5×10^{11}	3.5	5×10^{11}
4.0	10^{11}	4.0	5×10^{11}	4.0	5×10^{11}

In Figure 28 (a), the calculated electron temperature is same as the original value in all of the 7 groups of data. The largest error in electron density is approximately $4.37 \times 10^{11}\mathrm{cm^{-3}}$ which appears at $T_\mathrm{e} = 1.5$ eV. The error is larger when electron temperature is relatively low. In Figure 28 (b) the error of electron temperature is small except at the point when $T_\mathrm{e} = 2.5$ eV, the calculated electron temperature is 3.8 eV. The error of electron density is relatively smaller than results in Figure 28 (a). The largest error appears at $T_\mathrm{e} = 1.5$ eV, and the error also decreased with increasing electron temperature. In Figure 28 (c) the error of electron temperature is the same as the data in Figure 28 (b). Only when $T_\mathrm{e} = 2.5$ eV, the calculated result has large error. The error of electron temperature in other points can be almost neglected. The average error of electron density becomes smaller than Figure 28 (b), and the largest error is $4.12 \times 10^{11}\mathrm{cm^{-3}}$ which appears at $T_\mathrm{e} = 1.0$ eV. In general, the accuracy of calculated electron temperature is considerably high except some large error at $T_\mathrm{e} = 2.5$ eV. It could be caused by the neglecting of non-dominant processes. The error of electron density is relatively larger in the low electron-temperature range.

4.4.2. Experimental results

The low-pressure helium plasma was generated in the equipment shown in Chapter 2.5. The plasma was measured at different positions $(z = 0, 5, \text{and } 10\ \text{cm})$ at different pressures ($p = 2$ and 4 Torr). The obtained number density is shown in Table 13 and the determined electron density and temperature are shown in Figure 27.

Table 13. Measured number density N_p [cm^{-3}] of level 3^1S, 3^3S and 3^1D.

	$p = 2$ Torr	$p = 4$ Torr	
N_6	5.75×10^5	4.45×10^5	$z = 0$ cm
N_7	1.27×10^6	9.05×10^5	
N_{10}	4.16×10^5	2.87×10^5	
N_6	6.31×10^5	5.06×10^5	$z = 5$ cm
N_7	1.58×10^6	1.26×10^6	
N_{10}	4.54×10^5	3.66×10^5	
N_6	6.53×10^5	4.78×10^5	$z = 10$ cm
N_7	1.55×10^6	1.12×10^6	
N_{10}	3.53×10^5	2.07×10^5	

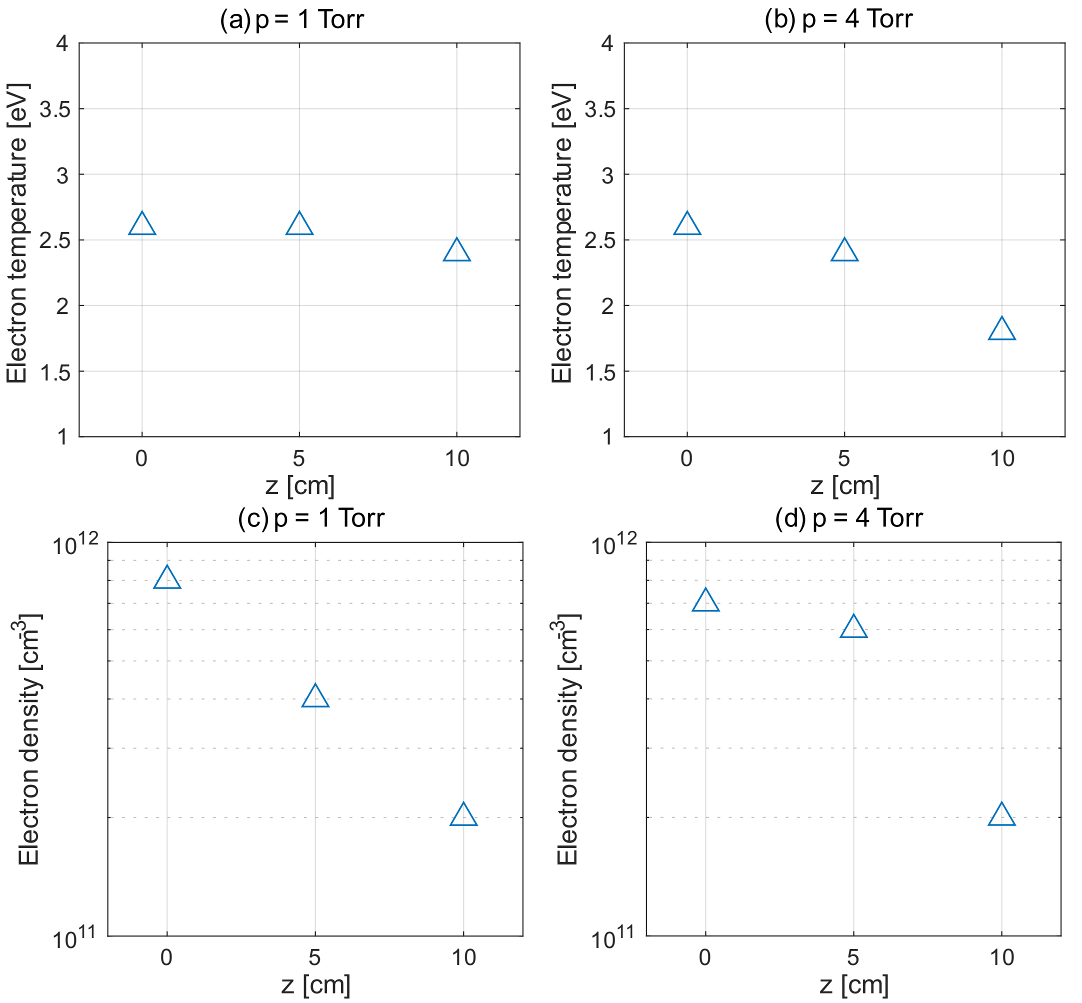

Figure 27. The electron density and temperature diagnosed by the simplified model with OES measurement.

When $p = 2$ Torr, the value of the calculated electron temperature was around 2.5 eV. The electron density was from 2×10^{11} cm^{-3} to 8×10^{11} cm^{-3}. When $p = 4$ Torr, the electron temperature was also around 2.5 eV at measurement position where $z = 0$ and 5 cm. When $z = 10$ cm, electron temperature drops to 1.8 eV. The electron density was 7×10^{11}, 6×10^{11}, and 2×10^{11} cm^{-3} when z equals to 0, 5, and 10 cm, respectively. In general, both electron density and temperature showed a trend of decrease with the increase of z.

5. IMPROVEMENT ON THREE-LINE INTENSITY ANALYSIS FOR LOW-PRESSURE HELIUM PLASMA FOR THERMO-NUCLEAR FUSION REACTOR

Emission lines in the visible wavelength range are widely used in the diagnoses of plasmas. The three-line diagnosis is commonly used to determine the electron density and temperature for helium plasmas, particularly for divertor region of thermonuclear fusion reactor. This method is relatively safe and effective because it only needs to measure three lines in the visible wavelength range. However, the results derived by this method sometimes show inconsistency with other diagnostic results. Therefore, the conventional method still needs further improvements to enhance its reliability.

This chapter demonstrates a new algorithm determining the electron density and temperature of the helium plasma. Firstly, the conventional method which uses only three emission lines and the inconsistency in the experimental results will be introduced. Then, the revision of the CR model and the development of the algorithm will be illustrated. Subsequently, the relevant experiment and discussions will be given. Unlike the previous chapter, the plasmas in Ch.4 have much higher electron temperature, and consequently, the models must be considerably different. Consequently, some special treatment becomes inevitably necessary, which will be specified through this chapter.

5.1. Three-Line Diagnosis

A conventional analysis for deriving T_e and N_e has been attempted with three emission lines, i.e., 667.8 nm, 706.5 nm, and 728.1 nm in the field of divertor measurement of thermonuclear fusion reactors. Intensities of emission lines with the derived T_e and N_e

for examining the consistency have been calculated. 501.6 nm line intensity shows clear discrepancy, and the influence of the reabsorption effect is suspected [66]. The results are shown in Figure 28. The red and blue symbols in Figure 28 (a) represent the intensity ratios of the specific lines for diagnosis, plotted against the line-averaged electron density determined by laser interferometer measurement.

In general, both of the determined electron density and the intensity ratio of lines at 667.8 and 728.1 nm show increasing trends with the increase of the line-averaged electron density; the determined electron temperature and the intensity ratio of the line at 728.1 and 706.5 nm have similar tendency. Thus, the three lines are commonly used for the diagnosis of the electron density and temperate due to their similar dependency on the line-average electron density for the parameter range of boundary area of thermonuclear fusion plasmas, i.e., $20 \leq T_e$ [eV] ≤ 400 and $10^{12} \leq n_e$ [cm^{-3}] $\leq 10^{14}$.

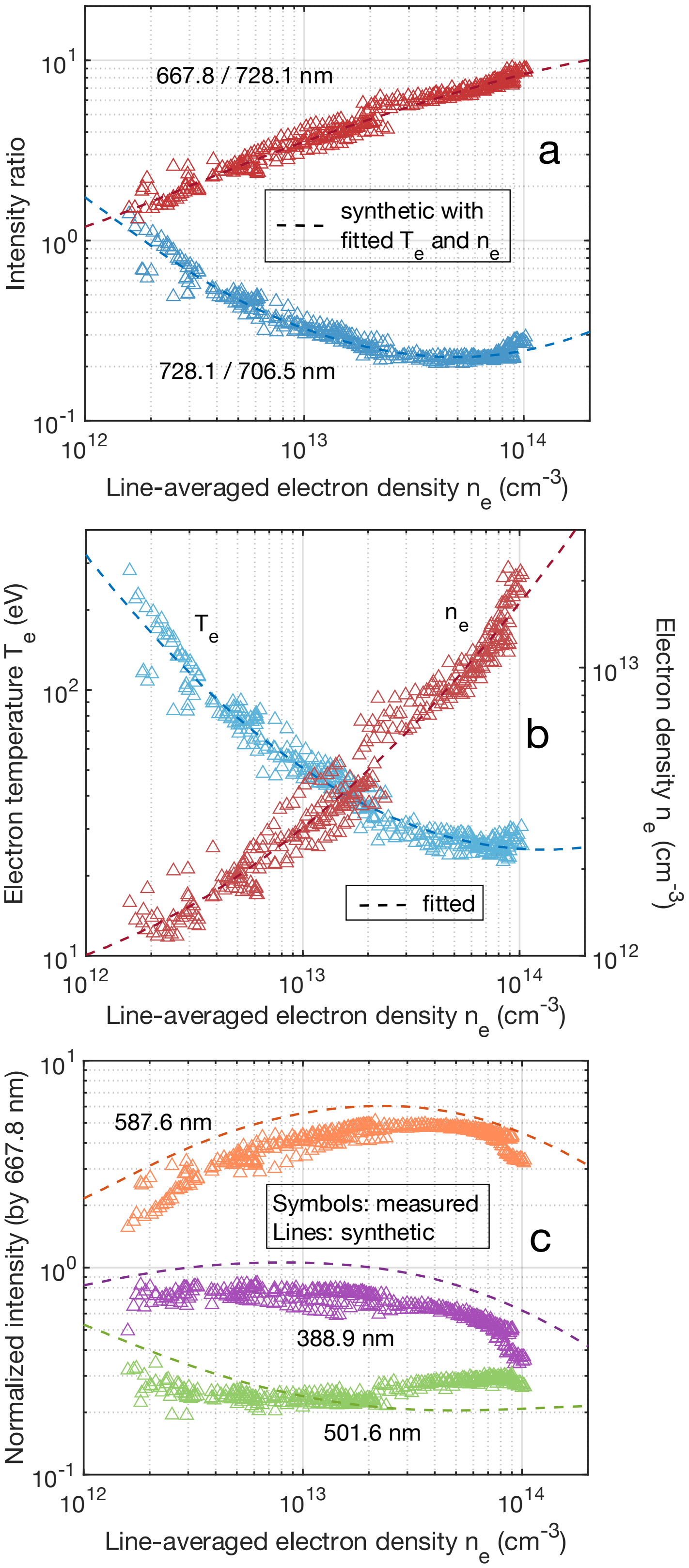

Figure 28. Results obtained with three emission lines. (a) Intensity ration of the three lines for diagnosis. (b) Electron density and temperature determined by the three-line diagnosis. (c) Comparison between the normalized intensities fitted by the three-line diagnosis and their counterparts measured by OES method directly.

The intensity ratio of the line at 667.8 and 728.1 nm (red symbols) increases with the increase of the line-averaged electron density and has almost the same increasing rate in the range from 10^{18} m^{-3} to 10^{20} m^{-3}. The intensity ratio of the line at 728.1 nm and 706.5 nm (blue symbols) has a tendency to decrease in the range from 1×10^{18} to 5×10^{19} m^{-3} with increasing line-averaged electron density, and starts to grow when it is larger than 6×10^{19} m^{-3}. The corresponding electron densities and temperatures determined are shown with the red and blue symbols in Figure 28 (b), respectively. The determined electron density increases with an increase of line-averaged electron density; the electron temperature decreases first, and shows an increasing trend when the line-averaged electron density is high. The results were fitted with polynomial functions and the results are shown with the dashed lines. The synthetic intensity ratios (dashed lines) obtained with the fitted T_e, N_e, and the CR model [37] are shown in Figure 28 (a) with the dashed lines. The synthetic results of the intensity ratios of the three lines agree their original values well in Figure 28 (a).

The normalized intensity of the other three observable lines (symbols) obtained by the OES measurement are also compared with the synthetic results in Figure 28 (c), and some disagreements are seen, i.e., the synthetic results of the lines at 388.9 and 587.6 nm have similar tendencies with corresponding measured results but there exist some differences between the results (lines and symbols). Especially when the line-averaged electron is approximately 10^{20} m^{-3}, relatively large errors occurred between the synthetic and measured results. In addition, the measured results of the line at 501.6 nm show the opposite trend with the corresponding synthetic result. Thus, it can be considered that using three lines to determine the electron density and temperature with the OES measurement and the CR model cannot perfectly fit the measured result. The conventional diagnosis could be further improved.

5.2. Methodology (Low-Pressure)

5.2.1. Calculation of optical escape factor (slab model)

The reabsorption effect can be incorporated in the model as the escape factor. Accurate evaluation of the escape factor is generally difficult. In a previous work, the escape factor was treated as a fitting parameter. However, the escape factor was introduced only for a single resonance line ($1^1\mathrm{S} - 4^1\mathrm{P}$), and the validity of the obtained value was not examined.

In this study, a persuasive method for determining the fitting conditions regarding the escape factors was developed. The escape factors can be roughly evaluated assuming the plasma has a slab or cylindrical structure (details of the escape factor with a slab model). An infinite plane-parallel slab model [67] with thickness $D = 0.01\ \mathrm{m}$ is applied. The optical escape factor at the center of the slab is considered, which is given by

$$\Lambda_{p,q} = \int_0^1 T\left(\frac{\kappa_\nu D}{2x}\right) \mathrm{d}x\,, \tag{5.2.1}$$

where the absorption coefficient κ_ν is obtained by Eqs. (1.2.43), (1.2.44), and (1.3.3a). $T(\tau_0)$ is the average probability that a photon within the line profile propagates τ_0:

$$T(\tau_0) = \int_{-\infty}^{\infty} \exp\left[-\tau_0 \cdot \frac{P(\nu)}{P(0)}\right] P(\nu) d\nu, \tag{5.2.2}$$

Figure 29 shows the calculated optical escape factors for the levels n^1P as a function of the ground state density.

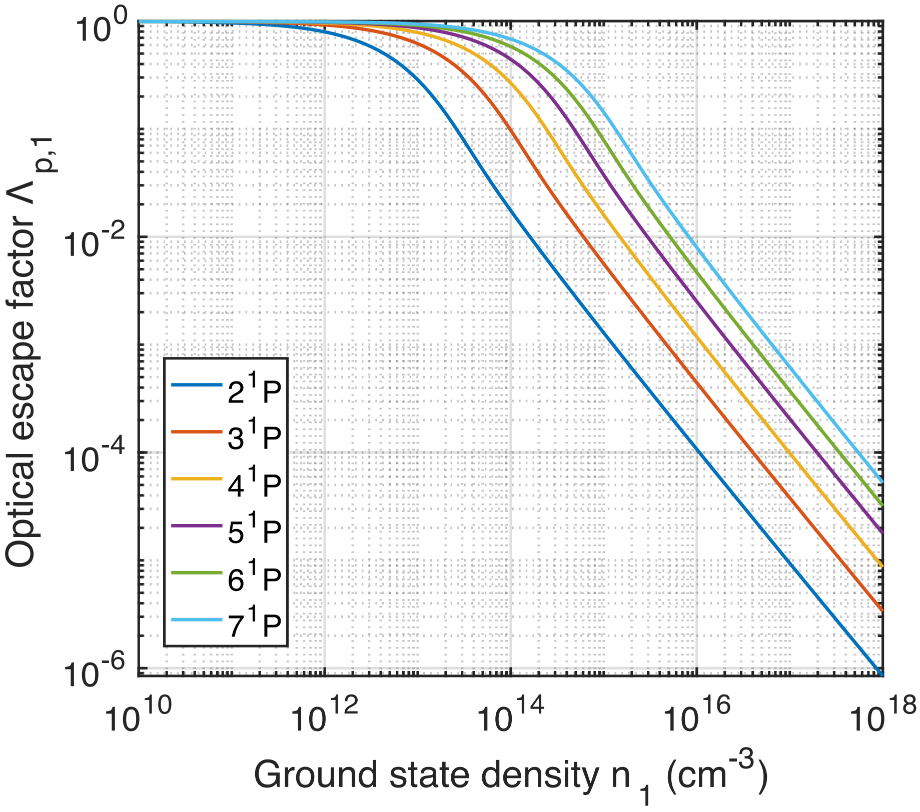

Figure 29. The optical escape factor of the n^1P levels ($n = 2, 3, 4, 5, 6$ and 7).

The 2^1P level has the smallest optical escape factor among the three n^1P levels. This indicates that lower levels have relatively stronger absorption effect. The absorption effect of n^1P ($n = 5, 6$ and 7) can be neglected when the ground state density is smaller than 10^{13} cm^{-3}.

5.2.2. Diagnosis of the electron density and temperature

An algorithm diagnosing the electron density and temperature was originally developed in this study. The diagram of the fitting algorithm is shown in Figure 30. It uses the number densities corresponding to the eight measured emission lines as input. The interior-point method [68][69] was applied to optimize the object function:

$$f_{\mathrm{obj}} = \sum_{p} \left(\frac{N_p - N_p'}{N_p^{\mathrm{small}}} \right)^2 + \mu \left(\frac{\Lambda_{n^1\mathrm{P},1^1\mathrm{S}}^{\mathrm{cal}} - \Lambda_{n^1\mathrm{P},1^1\mathrm{S}}'}{\Lambda_{n^1\mathrm{P},1^1\mathrm{S}}^{\mathrm{cal}}} \right)^2 , \tag{5.2.3}$$

where N_p' and $\Lambda_{n^1P,1^1S}'$ are the number density and optical escape factor generated by the optimizing algorithm. N_p^{small} equals to the smaller one between N_p and N_p'. $\Lambda_{n^1\mathrm{P},1^1\mathrm{S}}^{\mathrm{cal}}$ is the optical escape factor calculated by Eq. (5.2.1), which is basically a function of N_1' when T_{g} and D are fixed. The hyper parameter μ controls the weight of the restriction of the escape factors. The optimizing algorithm generates N_{e}', T_{e}', N_1', and $\Lambda_{p,q}'$ in different values and finds the global minimum of the object function. The outputs are the N_{e}' and T_{e}' that make the object function minimum.

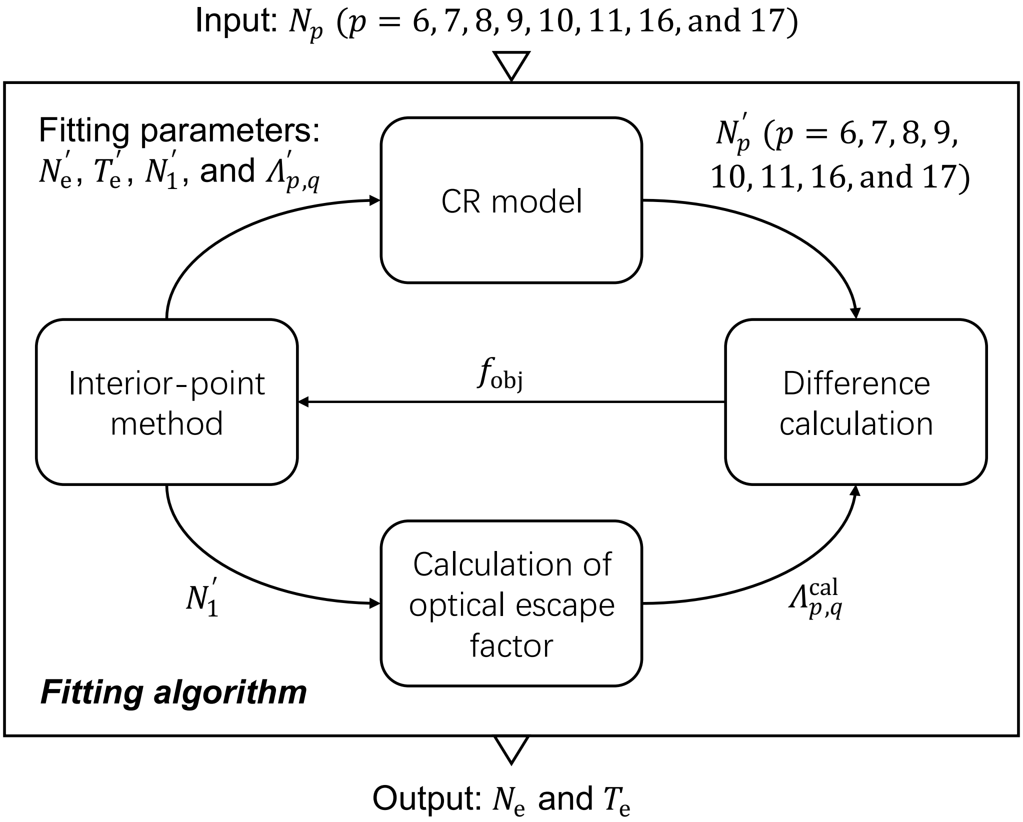

Figure 30. The diagram of the fitting algorithm for diagnosing the electron density and temperature.

5.2.3. Bias-variance analysis

The escape factors with a slab structure are evaluated and the fitting is conducted with a restriction that the derived escape factors should not be far away from the evaluated ones. Such a restriction can be realized by a regularization term in the object function like Eq. (5.2.3). Firstly, the optimum μ is determined through a bias-variance analysis. The bias-variance analysis [70][71][72] was used for determining μ. The helium plasma was generated in a stable condition. 40 spectra were obtained by OES measurements every 0.01 s. It is assumed that the electron density and temperature do not change during the 0.4 s. The acquired spectra were used for the analysis. The bias is obtained by:

$$(bias)^2 = \frac{1}{8} \sum_{p=6,7,8,9,10,11,16,17} \left[\frac{\log_{10}(|\bar{N}_p^{\mathrm{meas}} - \bar{N}_p^{\mathrm{fit}}|)}{\log_{10}(\bar{N}_p^{\mathrm{meas}})} \right]^2, \tag{5.2.4}$$

and the variance "*var*" is obtained by:

$$var = \frac{1}{8} \sum_{p=6,7,8,9,10,11,16,17} \left\{ \frac{1}{K} \sum_{k=1}^{K} \left[\frac{\log_{10}(|\bar{N}_p^{\mathrm{fit}} - N_p^{(k)\mathrm{fit}}|)}{\log_{10}(N_p^{\mathrm{fit}})} \right]^2 \right\}, \tag{5.2.5}$$

where $\bar{N}_p^{\mathrm{meas}}$ is the mean value of the measured number density of the level p, $\bar{N}_p^{\mathrm{fit}}$ is the mean value of the number density obtained by the fitting algorithm, and $N_p^{(k)\mathrm{fit}}$ is the fitted number density of level p in the *k*-th measured spectrum. The bias and variance with different μ, in the range of 0.01 – 100, are shown in Figure 31.

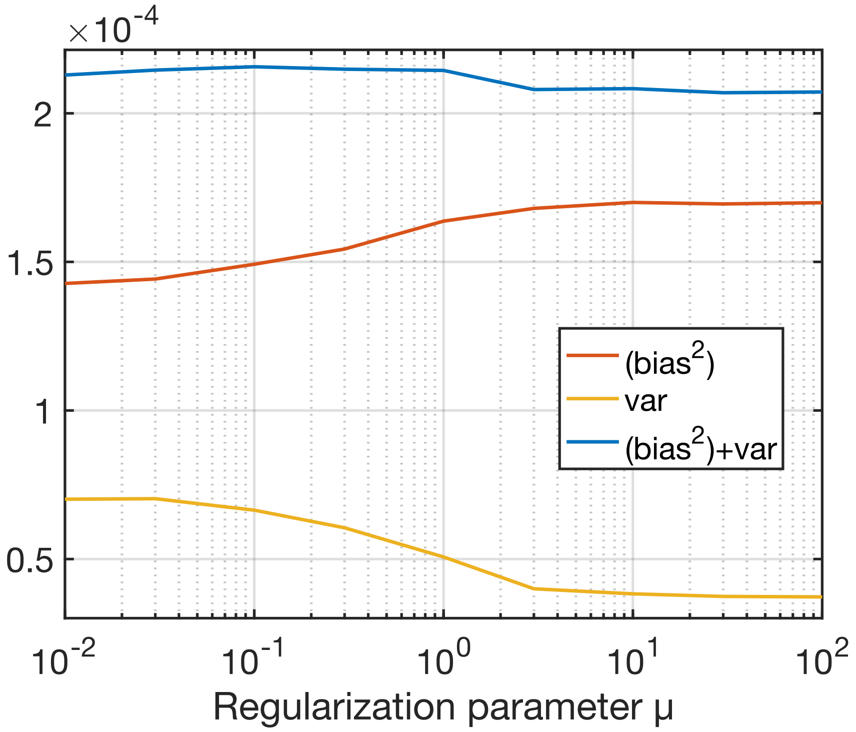

Figure 31. The calculated bias and variance of the algorithm with different μ.

The bias increases with an increase of the regularization parameter. It keeps relatively steady after μ is larger than 3. The variance decreases rapidly when μ is smaller than 3, and also keeps steady when μ is larger than 3. This indicates that the algorithm could be overfitted when $\mu < 3$. It is difficult to find the global minimum of the total error, but $\mu = 5$ is considered to be reasonable in the present case. It restricts the optical escape factors generated by the algorithm in a reasonable range but not completely being a function of the ground state density.

The present model could still suffer from the over-fitting problem, and we next attempt optimization for the number of escape factors considered in the model. Then, the bias-variance analysis is conducted again with increasing number of escape factors considered in the model. The results are shown in Figure 32

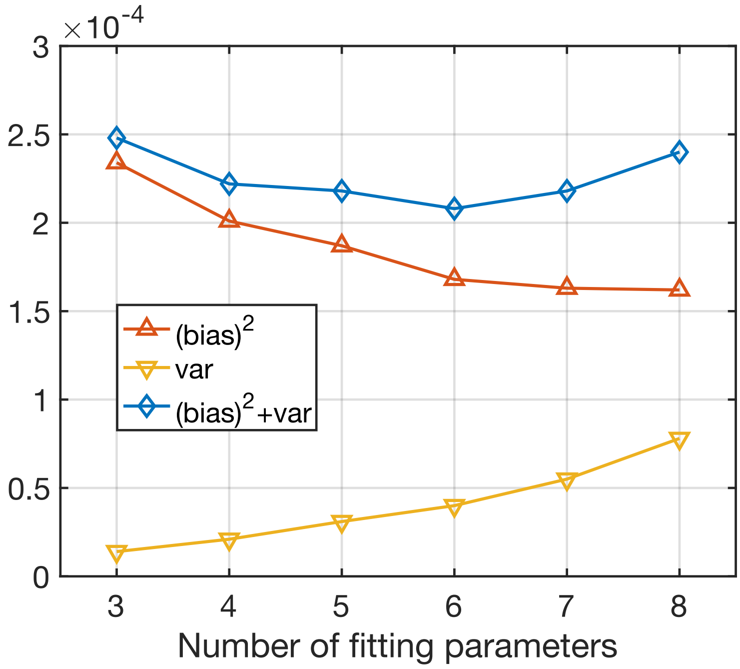

Figure 32. The calculated bias and variance of the algorithm with different number of fitting parameters.

The variance increases steady with an increase of the number of fitting parameters. The bias decreases rapidly when the number of fitting parameters is less than 6. The total error has the minimum value when the number of fitting parameters is equal to 6. Therefore, 6 parameters (N_e, T_e, N_1, $\Lambda_{4,1}$, $\Lambda_{8,1}$, and $\Lambda_{14,1}$) were selected as the fitting parameters of the algorithm.

5.3. LHD Experiment Setup

The measurements were made for LHD which is a heliotron type experiment device for the magnetically confined fusion plasma. The spectra of 10 discharges with helium gas was measured for which the magnetic axis radius was fixed at 3.6 m but the magnetic field strength was changed at 0.75 T, 1.5 T, and 2.75 T. The line-of-sight was roughly in the radial direction passing through the plasma central region on a horizontally elongated poloidal cross section. The field view collimated by a lens had a cylindrical profile of about 30 mm width. The light introduced into an optical fiber having a core diameter of 100 μm was guided to a Czerny-Turner type spectrometer having a focal length of 0.5 m. The spectrometer was equipped with a 100 grooves/mm grating and the reciprocal linear dispersion was measured to be 19.976 nm/mm. A CCD (charge-coupled-device) consisting of 1024 pixels x 255 pixels with each pixel size of 26 μm x 26 μm was used as a detector. Consequently, a wavelength width of about 520 nm could be measured simultaneously. The central wavelength was adjusted to cover all the six transitions from $n = 3$ to $n = 2$, i.e., 388.9 nm to 728.1 nm. The line-of-sight of the measurement is shown in the following figure.

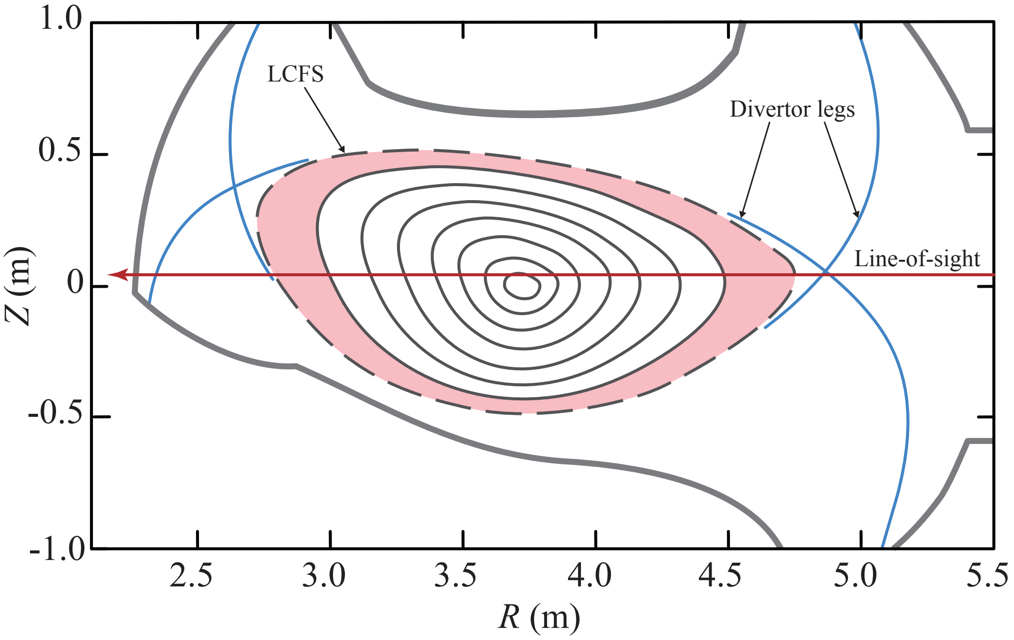

Figure 33. A cross-sectional view of the plasma with the magnetic flux surfaces in the measurement.

5.4. Results and Discussion (low-pressure)

Comparison between the electron density and temperature obtained as the fitting results and those obtained by three-line analysis are shown in Figure 34. Both electron density and temperature obtained with the new method have increasing and decreasing tendency with an increase of the line-averaged electron density which are similar to the results, as shown in Figure 30 (b), obtained by the three-line method. When the line-averaged electron density is low, the electron temperature obtained by the two method is close. The electron temperature diagnosed by the new model decreases faster when the line-averaged electron density becomes much higher. The electron density obtained by the new model is generally slightly lower than counterpart obtained by the three-line method. The measured intensities of the eight states and their counterparts fitted by the algorithm and three-line analysis are shown in Figures 35 - 36, respectively. All the fitted results show the similar tendencies with their corresponding measured results with an increase of the line-averaged electron tendency. The 3^1S, 3^3S, 3^1P, 3^3P, 3^1D, and 3^3D show relatively a good fitting, and the differences between the measured and fitted results are small. The differences for the level 4^1D and 4^3D are relatively large. Comparing with the results of three-line analysis, the difference between the fitted and measured line intensity of level 3^1S, 3^3S, and 3^1D slightly increased. The fitting of the level 3^1P and 3^3D was improved a little. The level 3^3P, 4^1D, and 4^3D of the new algorithm had better fitting.

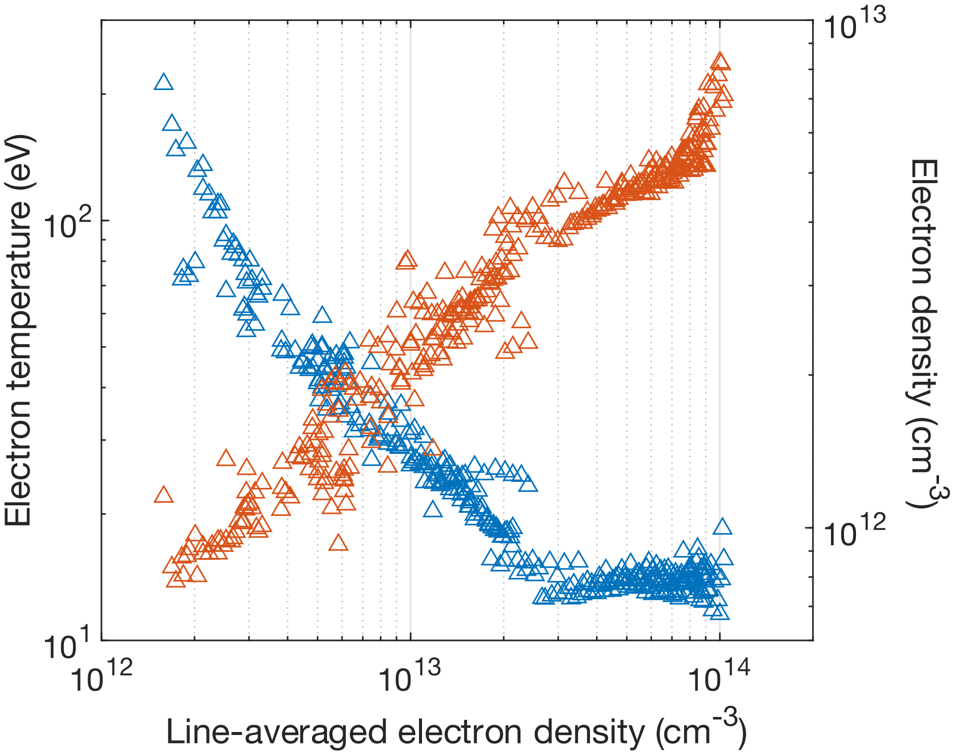

Figure 34. Results obtained with the new fitting algorithm.

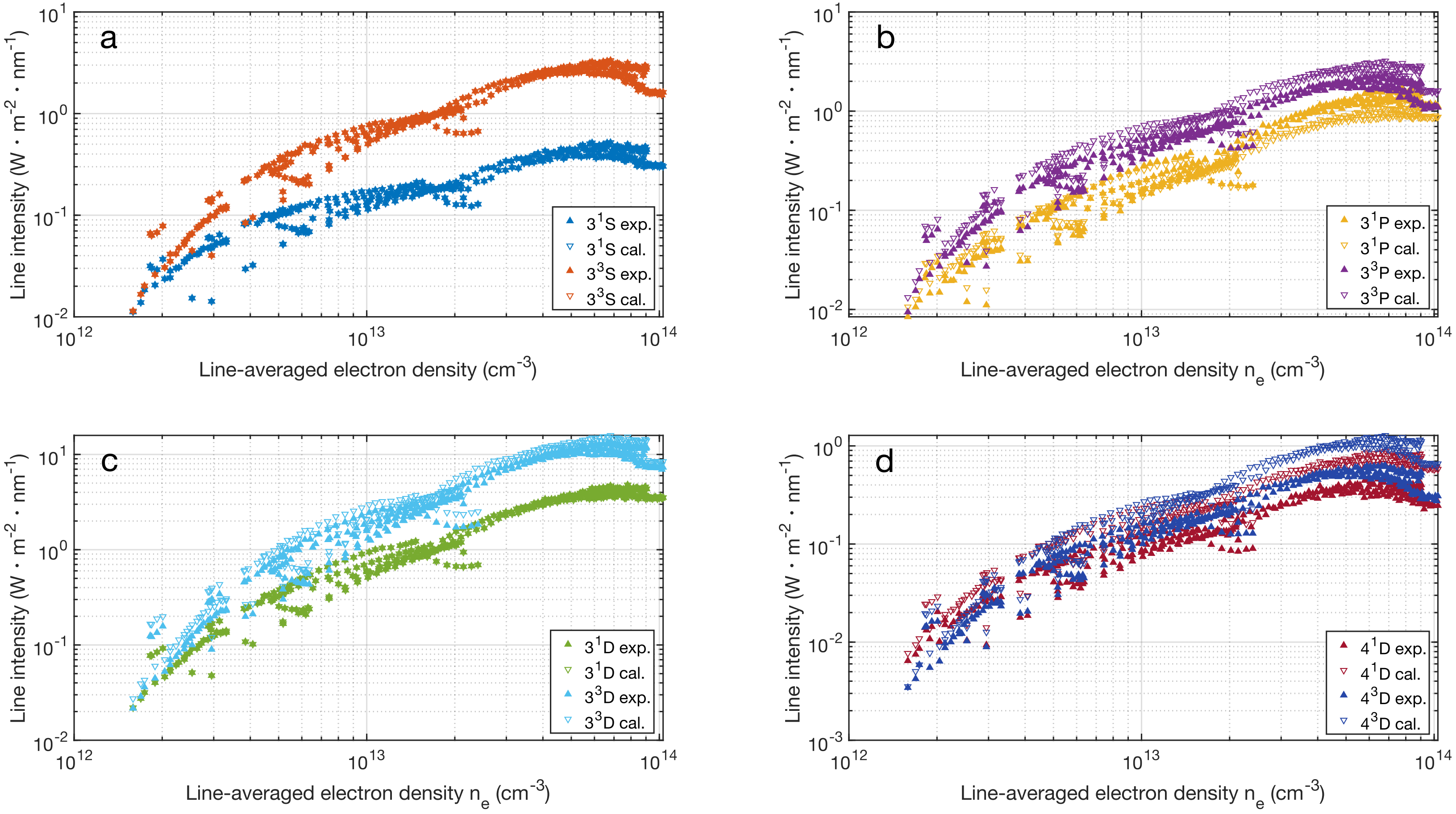

Figure 35. Comparison between the number densities measured in the experiment (solid symbols) and those fitted by three-line analysis (hollowed symbols). (a) The number densities of states 3^1S (p = 6) and 3^3S (p = 7). (b) The number densities of states 3^1P (p = 8) and 3^3P (p = 9). (c) The number densities of states 3^1D (p = 10) and 3^3D (p = 11). (d) The number densities of states 4^1D (p = 16) and 4^3D (p = 17).

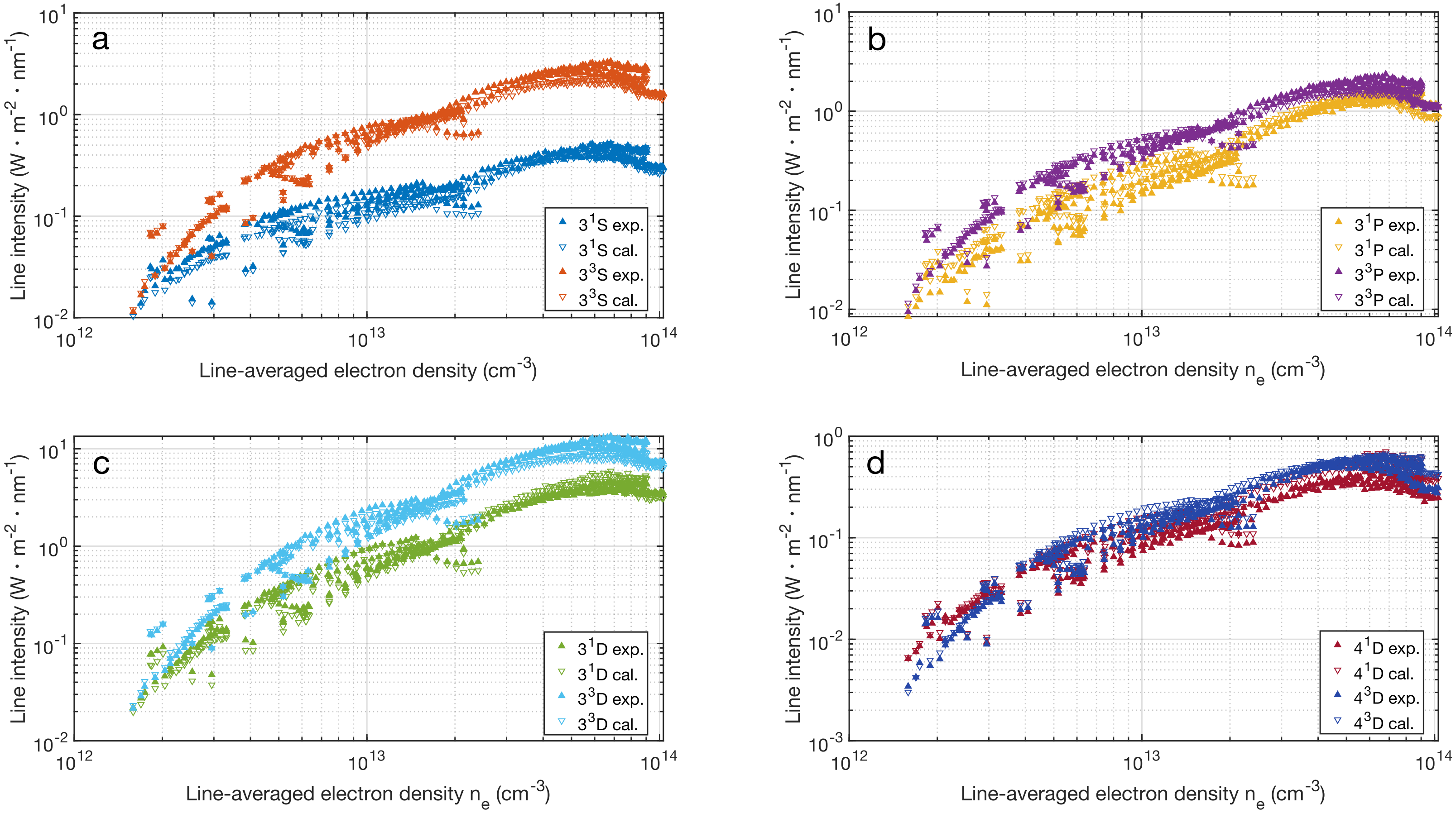

Figure 36. Comparison between the number densities measured in the experiment (solid) and those fitted by the new algorithm (hollowed). (hollowed symbols). (a) The number densities of states 3^1S (*p* = 6) and 3^3S (*p* = 7). (b) The number densities of states 3^1P (*p* = 8) and 3^3P (*p* = 9). (c) The number densities of states 3^1D (*p* = 10) and 3^3D (*p* = 11). (d) The number densities of states 4^1D (*p* = 16) and 4^3D (*p* = 17).

6. DEVELOPMENT OF DIAGNOSTICS FOR ATMOSPHERIC-PRESSURE HELIUM PLASMA

The OES method is commonly used to measure various plasma types. OES diagnoses both line and continuum spectra to determine the electron density and temperature of argon plasma [73], as the atmospheric-pressure argon CR model has already been developed [74][75]. Unfortunately, the current OES diagnostics based on the helium CR model are only available for low pressures, mainly because the current helium CR model, which is demonstrated in Chapter 1, only considers electron collisions and radiative processes, as these dominate the population and depopulation at low pressures. As the pressure increases, atomic collisions become the dominant process instead of electron collisions, so the conventional model no longer works. The conventional CR model needs to be improved for the atmospheric pressure.

6.1. Methodology (Atmospheric Pressure)

In this chapter, the development of an atmospheric-pressure helium CR model is presented. Based on the new model, an algorithm capable of diagnosing the electron density and temperature as well as the number density of two metastable states by fitting the results of OES measurements has been developed.

6.1.1. Atomic process (atmospheric pressure)

According to the ideal gas law:

$$P = N_1 k_{\mathrm{B}} T_{\mathrm{g}}, \tag{6.1.1}$$

for weak ionized plasma at room temperature $T_{\mathrm{g}} = 300\ \mathrm{K}$ and atmospheric pressure, the ground state density can be approximately $2.4 \times 10^{25}\ \mathrm{m}^{-3}$, which is much higher than the electron density. Since the flux is obtained by multiplying the flow rate with the density of the incident particle, the populating and depopulating fluxes contributed by atomic collisions (neutral impacts) are essential compared to those at low pressure. In order to make the CR model also available at atmospheric pressure, it is necessary to include the atomic collision processes into the model. Figure 37 shows the processes considered in the new model.

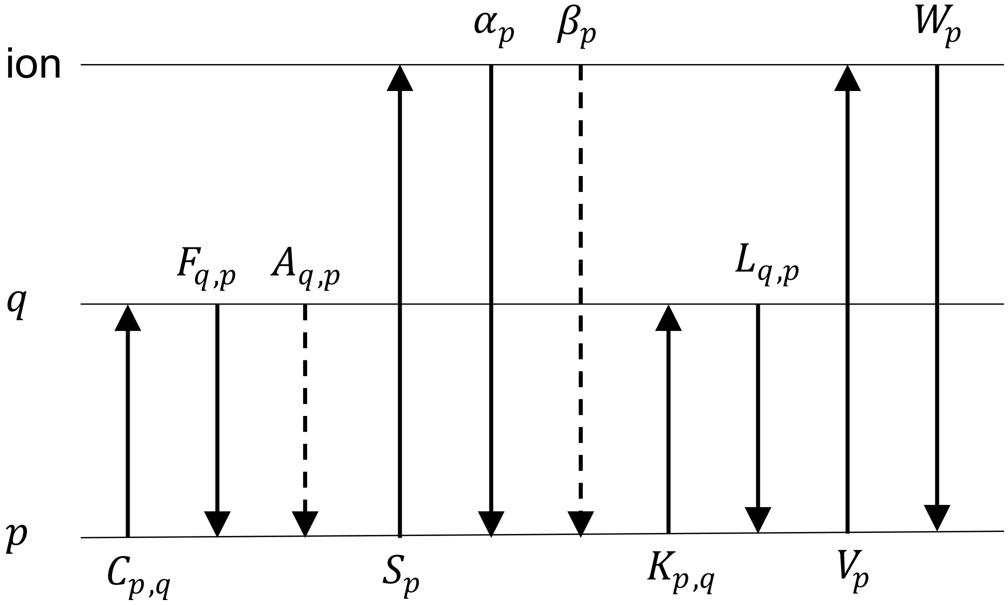

Figure 37. Populating and depopulating processes in the atmospheric-pressure helium CR model. The solid and dashed lines represent collisional and radiative processes, respectively.

Processes in Eqs. (2.1.1a) – (2.1.1f) are included. Obtaining details of the rate coefficients are shown in Chapter 2.3. The infinite cylinder model (Chapter 1.3.2) is used for calculating the escape factor of optical thick levels ($1^1\mathrm{S}$, $2^1\mathrm{S}$, and $2^3\mathrm{S}$). Although cross sections for the dissociative recombination of the $\mathrm{He_2}^+$ in the energy region of 1-15 eV have been investigated [77], its influence to the excited state populations have not been studied yet. Therefore, impacts of molecular ions He_2^+ are omitted in this model.

6.1.2. Rate equation (atmospheric pressure)

The temporal development of the number density of level p at atmospheric pressure can be described in the similar way as Eq. (2.1.2) by ignoring all the other transitions:

$$\frac{\mathrm{d}N_p}{\mathrm{d}t} = \sum_{q<p} C_{q,p} N_\mathrm{e} N_q + \sum_{q>p} F_{q,p} N_\mathrm{e} N_q + \sum_{q>p} A_{q,p} N_q - \sum_{q>p} C_{p,q} N_\mathrm{e} N_p -$$

$$\sum_{q<p} F_{p,q} N_\mathrm{e} N_p - \sum_{q<p} A_{p,q} N_p - S_p N_\mathrm{e} N_p + \alpha_p {N_\mathrm{e}}^2 N_\mathrm{i} + \beta_p N_\mathrm{e} N_\mathrm{i}$$

$$+ \sum_{q<p} K_{q,p} N_1 N_q + \sum_{q>p} L_{q,p} N_1 N_q - \sum_{q>p} K_{p,q} N_1 N_p - \sum_{q<p} L_{p,q} N_1 N_p -$$

$$V_p N_1 N_p + W_p N_1 N_\mathrm{e} N_\mathrm{i}. \tag{6.1.2}$$

The first two lines are same as the rate equation at low pressure. The third and fourth line are the flux contributed by atomic collisions. Chapter 1.4.3 introduced QSS as approximation to simplify the rate equations. In the case of helium, the $2^1\mathrm{S}$ ($p = 2$) and $2^3\mathrm{S}$ ($p = 3$) levels, which are called the metastable states, have much longer relaxation time than other excited levels because the transitions from them are forbidden in quantum mechanism. Thus, if we neglect their diffusion loss or three-body atomic collisional losses as in Eq. (6.1.2), it is better to also consider the time derivative of them to increase the accuracy of calculations:

$$\frac{\mathrm{d}N_p}{\mathrm{d}t} = 0\ (p \geq 4), \tag{6.1.3}$$

The matrix of these levels is expressed as

$$\begin{pmatrix} \zeta_{1,4} & \zeta_{2,4} & \zeta_{3,4} & -\zeta_{4} & \zeta_{5,4} & \zeta_{6,4} & & \zeta_{65,4} \\ \zeta_{1,5} & \zeta_{2,5} & \zeta_{3,5} & \zeta_{4,5} & -\zeta_{5} & \zeta_{6,5} & \cdots & \zeta_{65,5} \\ \zeta_{1,6} & \zeta_{2,6} & \zeta_{3,6} & \zeta_{4,6} & \zeta_{5,6} & -\zeta_{6} & & \zeta_{65,6} \\ & & & \vdots & & & \ddots & \vdots \\ \zeta_{1,65} & \zeta_{2,65} & \zeta_{3,65} & \zeta_{4,65} & \zeta_{5,65} & \zeta_{5,65} & \cdots & -\zeta_{65} \end{pmatrix} \begin{pmatrix} N_1 \\ N_2 \\ N_3 \\ N_4 \\ N_5 \\ N_6 \\ \vdots \\ N_{65} \end{pmatrix} = \begin{pmatrix} -\zeta_{\mathrm{ion},4} \\ -\zeta_{\mathrm{ion},5} \\ \vdots \\ -\zeta_{\mathrm{ion},65} \end{pmatrix} N_{\mathrm{i}} \quad (6.1.4a)$$

with

$$\zeta_{q,p} = C_{q,p}N_{\mathrm{e}} + A_{q,p} + K_{q,p}N_1, \quad (6.1.4b)$$

$$\zeta_p = S_pN_{\mathrm{e}} + V_pN_1 \sum_{p \neq q} (C_{p,q}N_{\mathrm{e}} + A_{p,q} + K_{p,q}N_1)\,, \quad (6.1.4c)$$

and

$$\zeta_{\mathrm{ion},p} = \alpha_p N_{\mathrm{e}} N_{\mathrm{i}} + \beta_p N_{\mathrm{e}} + W_p N_{\mathrm{e}} N_1. \quad (6.1.4d)$$

It should be noted that to simplify the expression, $C_{p,q}$, $F_{p,q}$ and $K_{p,q}$, $L_{p,q}$ are written as single rate coefficients. $F_{p,q}$ is replaced by $C_{p,q}$, and $L_{p,q}$ is replaced by $K_{p,q}$ when $p > q$. The populations of all levels p ($p \geq 4$) can be solved if N_1, N_2, and N_3 is known. N_1 is given by the equation of ideal gas under the present condition of low degree of ionisation:

$$p = N_1 k_{\mathrm{B}} T_{\mathrm{g}}, \quad (6.1.15)$$

where p is the pressure.

6.1.3. Development of the fitting algorithm

The fitting algorithm is developed in MATLAB and the flowchart of the program is shown in Figure 38.

The object function is defined as

$$f_{\mathrm{obj}} = \sum_{\substack{p=6,7,8,9,10\\11,16,17}} \left(\frac{N_p^{\mathrm{exp}} - N_p^{\mathrm{cal}}}{N_p^{\mathrm{small}}}\right)^2, \tag{6.1.16}$$

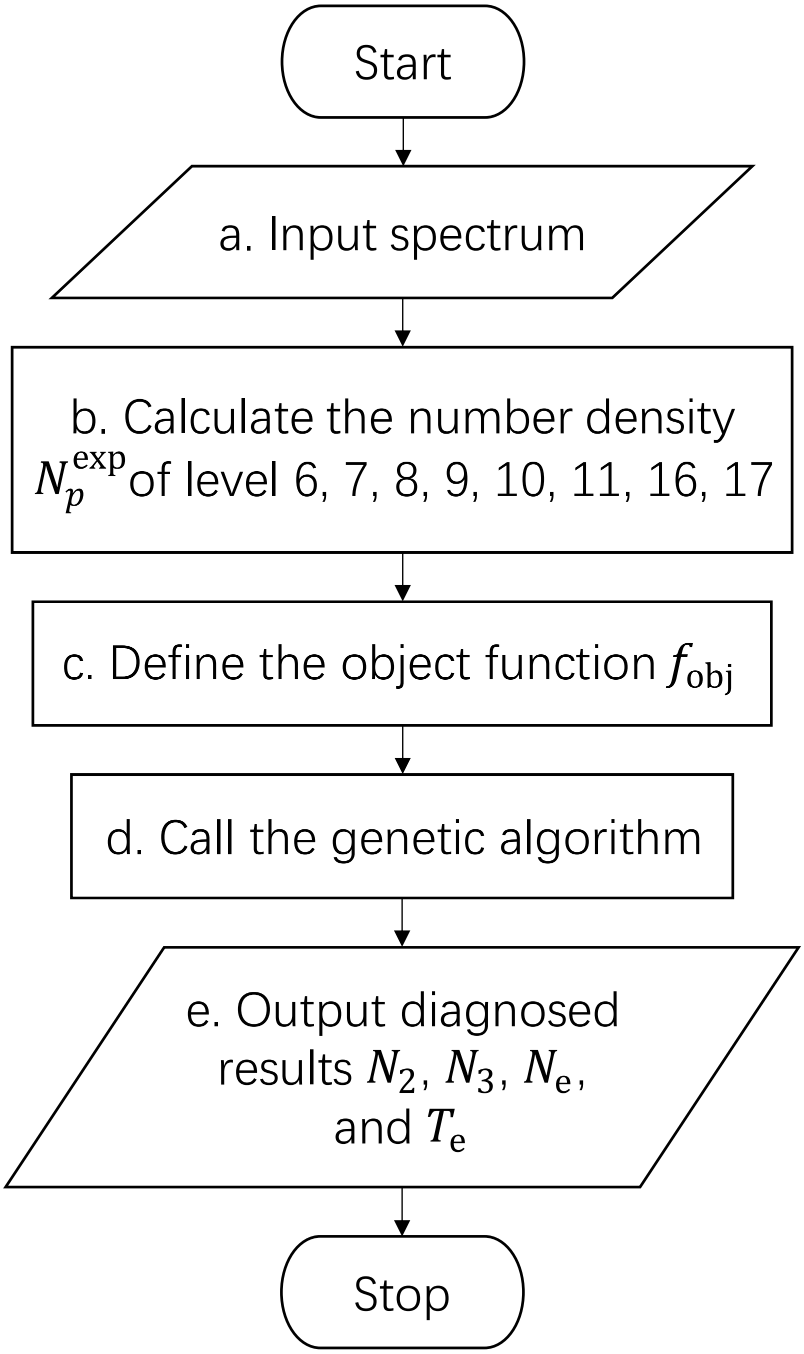

Figure 38. Flowchart of the developed fitting algorithm.

where N_p^{exp} is the number density measured in the experiment, N_p^{cal} *is* the number density calculated with the revised CR model, and N_p^{small} equals to the smaller one in N_p^{exp} and N_p^{cal}. The flow chart of the object function is show in Figure 39.

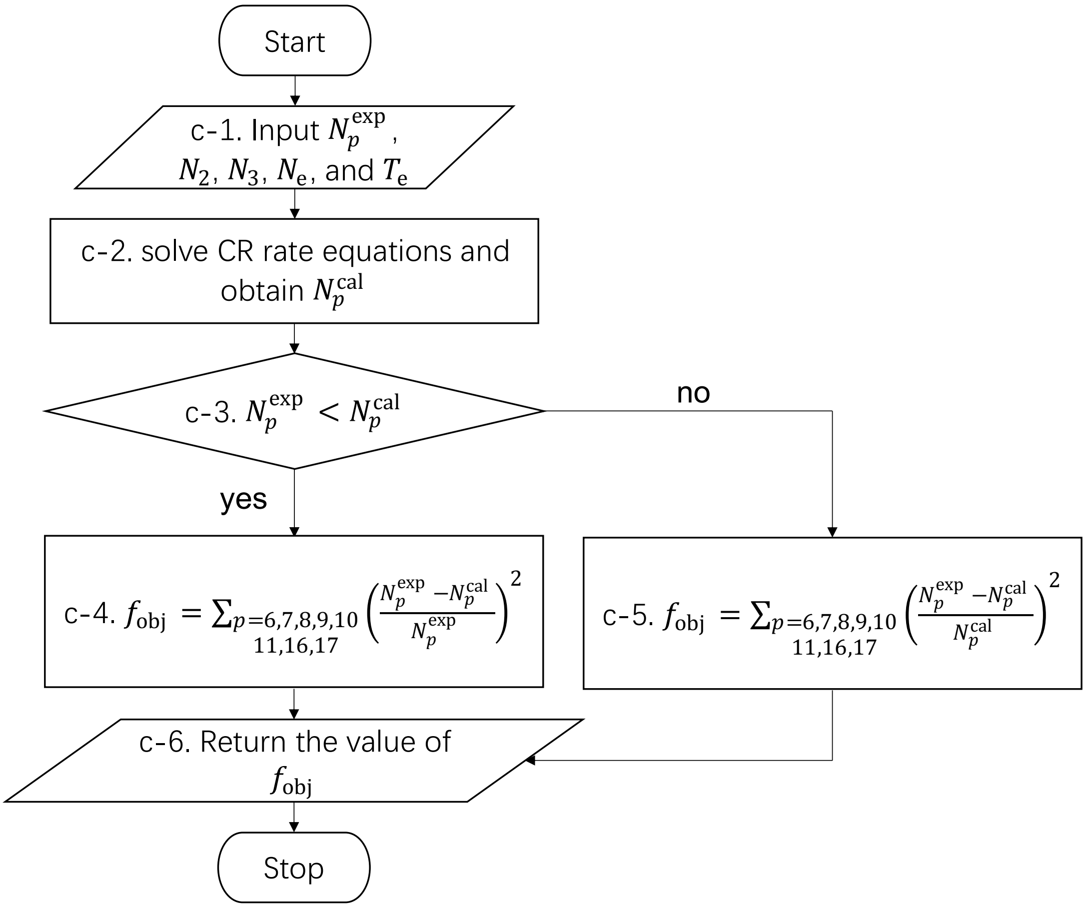

Figure 39. Fowchart of the object function.

The object function solves the rate equations shown in Eq. (5.1.14) in the step c-2 according to the input in the step c-1. The object function is defined as:

```
function diff = f_obj(Te,Ne,N2,N3,Np_exp)
```

It is optimized by the genetic algorithm [78] in the step d:

```
fun_obj = @(pp) f_obj(pp(1),pp(2),pp(3),pp(4),Np_exp);
rslt = ga(fun_obj,4,[],[],[],[],lb,ub,[],opt_ga);
```

6.2. Atmospheric-Pressure AC Discharged Helium Plasma

The discharge tube for atmospheric-pressure helium plasma is shown in Figure 40.

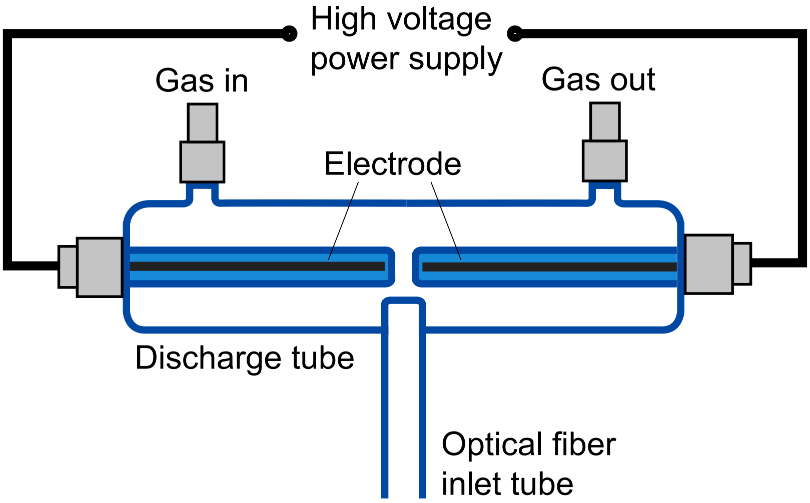

Figure 40. Schematic overview of the atmospheric-pressure non-equilibrium discharge plasma generator.

An inverter-type neon transformer is applied to supply high voltage up to 9.0 kVp-p. The details of the power supply are shown in the following table.

Table 14. Helium lines used for line spectrum analysis.

Maker	RECIP
MODEL	100-C-9HEP
Input voltage	AC 100V
Input current	0.8 A
Input frequency	50 – 60 Hz
Output voltage	9 kVo-p

Figure 41 shows the parameters of the OES measurement for the atmospheric-pressure non-equilibrium discharge plasma generator.

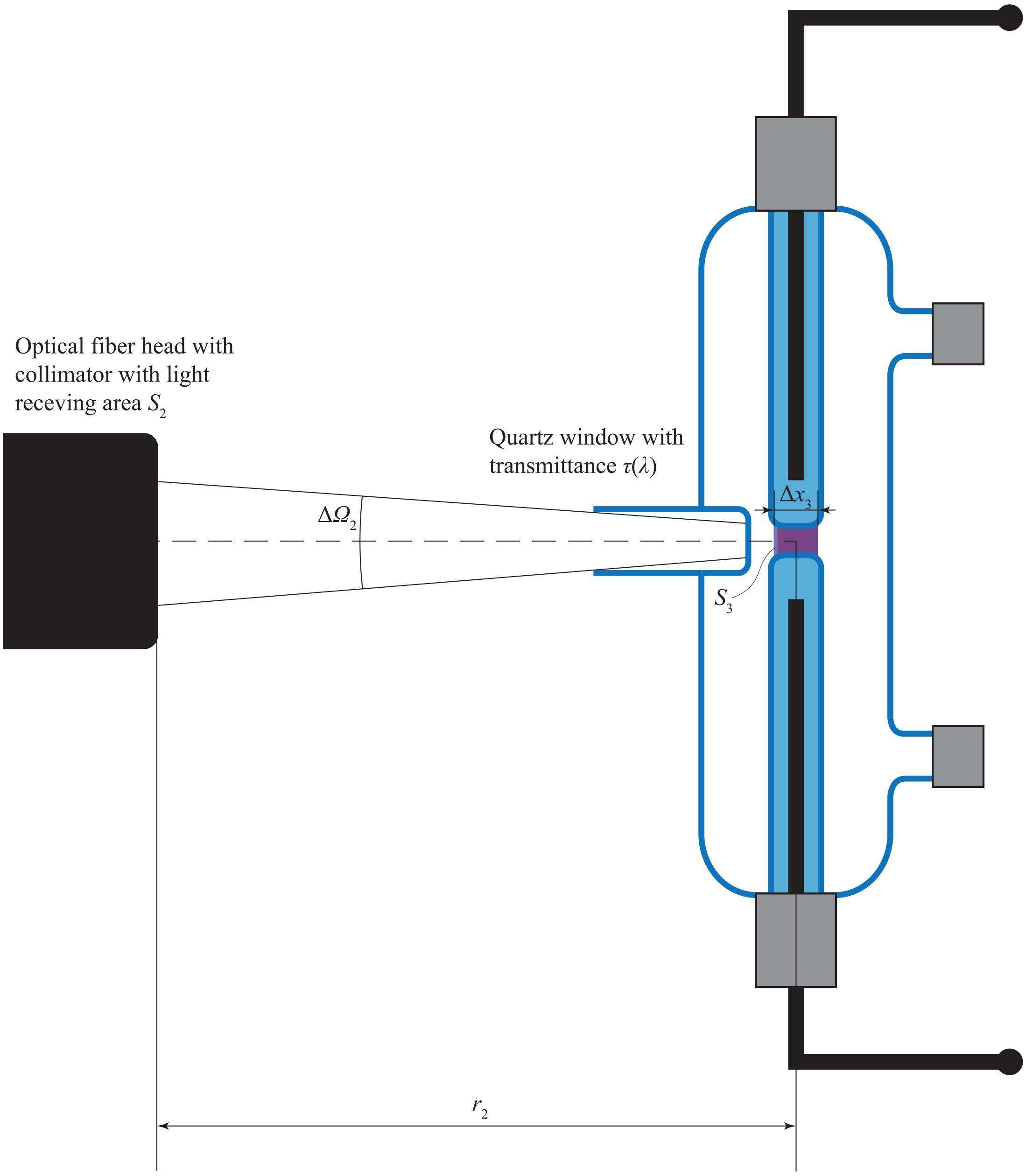

Figure 41. Parameters of the OES measurement of the atmospheric pressure plasma.

Δx_3 is the depth of the plasma in the direction that is parallel to the measurement direction, S_3 is the luminous area observed from the fiber head. The solid angle $\Delta\Omega_2$ is given by

$$\Delta\Omega_2 = \frac{S_2}{{r_2}^2}. \tag{6.2.1}$$

According to Eqs. (3.2.1) and (3.2.4a) the spectral raidance including the transimittance of the quatz window $\tau(\lambda)$ is given by

$$\begin{aligned} L(\lambda) &= \frac{hc}{\lambda}\frac{y_{\text{meas}}(\lambda)}{\eta(\lambda)\tau(\lambda)S_3\Delta\Omega_2} = \frac{hc}{\lambda}\frac{{r_2}^2}{S_2 S_3}\frac{y_{\text{meas}}(\lambda)}{\eta(\lambda)\tau(\lambda)} \\ &= \frac{S_2{r_2}^2}{\pi S_3{r_1}^2}\frac{\rho(\lambda)E(\lambda)}{\tau(\lambda)}\frac{y_{\text{meas}}(\lambda)}{y_{\text{cali}}(\lambda)}, \end{aligned} \tag{6.2.2}$$

The spectral emissivity is given by

$$\varepsilon(\lambda) = \frac{L(\lambda)}{\Delta x_3} = \frac{S_2{r_2}^2}{\pi\Delta x_3 S_3{r_1}^2}\frac{\rho(\lambda)E(\lambda)}{\tau(\lambda)}\frac{y_{\text{meas}}(\lambda)}{y_{\text{cali}}(\lambda)}, \tag{6.2.3}$$

The line emissivity of a specific transition is given by

$$\varepsilon_{p,q} = \int_{\text{line}} \varepsilon(\lambda)\, d\lambda = \frac{S_2{r_2}^2}{\pi\Delta x_3 S_3{r_1}^2}\int_{\text{line}} \frac{\rho(\lambda)E(\lambda)}{\tau(\lambda)}\frac{y_{\text{meas}}(\lambda)}{y_{\text{cali}}(\lambda)}\, d\lambda. \tag{6.2.4}$$

Then, according to Eqs. (3.2.4) and (3.2.5) the number density of the corresponding line can be obtained as

$$\begin{aligned} N_p &= \frac{\lambda_{p,q}}{hc}\frac{4\pi}{A_{p,q}}\int_{\text{line}} \varepsilon(\lambda)\, d\lambda = \frac{\lambda_{p,q}}{hc}\frac{4\pi}{A_{p,q}}\varepsilon_{p,q} \\ &= \frac{4}{A_{p,q}}\frac{\lambda_{p,q}}{hc}\frac{S_2{r_2}^2}{\Delta x_3 S_3{r_1}^2}\int_{\text{line}} \frac{\rho(\lambda)E(\lambda)}{\tau(\lambda)}\frac{y_{\text{meas}}(\lambda)}{y_{\text{cali}}(\lambda)}\, d\lambda. \end{aligned} \tag{6.2.5}$$

6.3. Results and Discussion

6.3.1. Microwave induced low-pressure helium plasma

The algorithm was applied to measure low-pressure microwave induced helium plasma ($p = 1$ Torr). The results were compared with those obtained by the double probe method in Chapter 2.4. Comparison of the determined electron density and temperature at different measurement position z are shown in Figure 42.

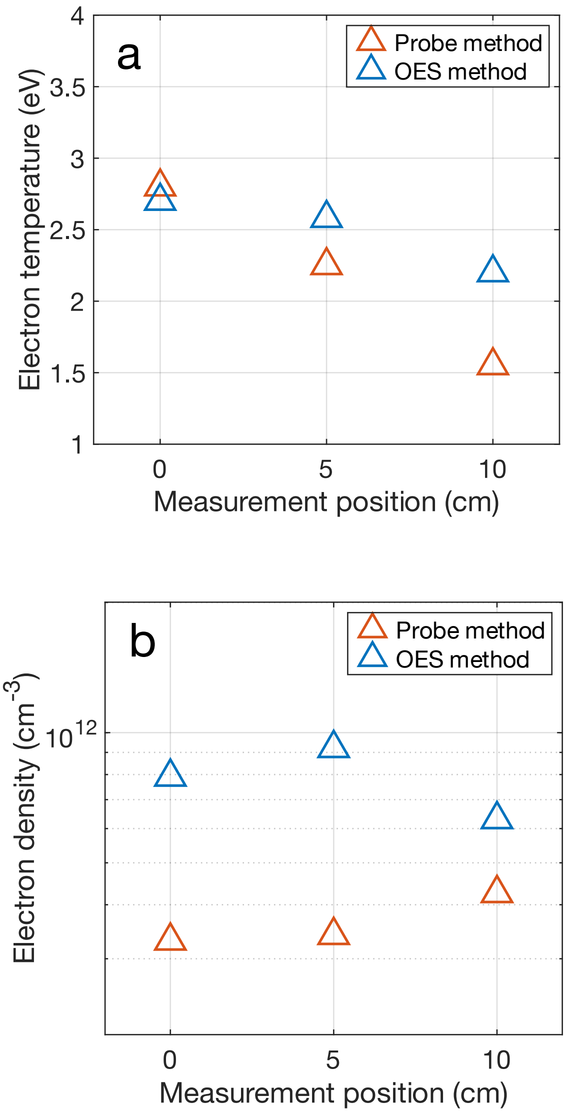

Figure 42. Comparison of results between OES diagnosis and probe method. (a) Determined electron temperature, (b) Determined electron density.

The blue and orange symbols represent the results obtained by the OES diagnosis and the probe method, respectively. In Figure 42 (a), the electron temperature measured by the probe method decreases from 2.8 to 1.6 eV. The electron temperature determined by OES decreases from 2.7 to 2.3 eV. The largest difference between the two methods is only approximately 0.7 eV and the measurement results show the same trend with the increase of the measurement position. In Figure 42 (b), the electron density measured with both methods does not change significantly with the measurement position. The electron density measured by the probe method is approximately $4 \times 10^{11}\ \mathrm{cm}^{-3}$, which is slightly lower than the results obtained by the OES diagnosis ($8 \times 10^{11}\ \mathrm{cm}^{-3}$ in average). In general, the electron density determined by the two methods is of the same order of magnitude, and the measured electron temperature is similar. Thus, it can be assumed that the results of the algorithm at low pressure, $p = 1\ \mathrm{Torr}$ agree well with those of the probe method.

6.3.2. Atmospheric-pressure non-equilibrium helium plasma

6.3.2.1 Dependency of number density on plasma parameters

The Figure 43 shows the electron density, electron temperature, and gas temperature dependency of the number density of the eight levels calculated by the revised model (pressure was set to 760 Torr). In Figure 43 (a), the number density is calculated for a fixed electron density ($N_\mathrm{e} = 10^{11}\ \mathrm{cm}^{-3}$), fixed gas temperature ($T_\mathrm{g} = 300$ K), and an electron temperature range $T_\mathrm{e} = 1 - 10\ \mathrm{eV}$. The number densities of all the levels increase rapidly with the growth of the electron temperature in the range of 1-3 eV. In the range of higher electron temperatures, they increase relatively slowly. The reduced number density of the level $3^1\mathrm{S}$ is the largest of the 8 levels up to 7 eV, and is suppressed by level $3^1\mathrm{P}$. In the high electron temperature region, the reduced number densities of levels $3^1\mathrm{S}$, $3^3\mathrm{S}$, $3^1\mathrm{D}$, and $3^3\mathrm{D}$ are very close to those of levels $3^1\mathrm{P}$, $3^3\mathrm{P}$, $4^1\mathrm{D}$, and $4^3\mathrm{D}$, respectively. According to Figure 43 (b), the proportion of

reduced number density of the eight levels is similar when the electron temperature and gas temperature are fixed at 2 eV and 300 K, respectively, from 10^9 to 10^{11} cm^{-3}. The increasing rates of $3^1\mathrm{D}$ and $3^3\mathrm{D}$ become much larger than those of the other levels when $n_\mathrm{e} > 10^{11}$ cm^{-3}. This could be due to the electron collision excitation from lower levels, which dominate the population processes at high electron density. Figure 43 (c) shows a line chart of the number density as a function of gas temperature. The electron density and temperature were 10^{11} cm^{-3} and 2 eV, respectively. Since the ground-state density can be determined by $p = nk_\mathrm{B}T_\mathrm{g}$, it decreases with an increase in gas temperature at a fixed pressure. The $3^1\mathrm{S}$, $3^3\mathrm{S}$, $3^1\mathrm{P}$, $3^3\mathrm{P}$, $3^1\mathrm{D}$, and $3^3\mathrm{D}$ levels have a similar decreasing trend with increasing gas temperature. The states $4^1\mathrm{D}$ and $4^3\mathrm{D}$ also have the same tendencies as the other levels in the low gas temperature region but off more rapidly when $T_\mathrm{g} > 1500$ K. This might be caused by their relatively higher atomic collision de-excitation rate coefficients at high gas temperature.

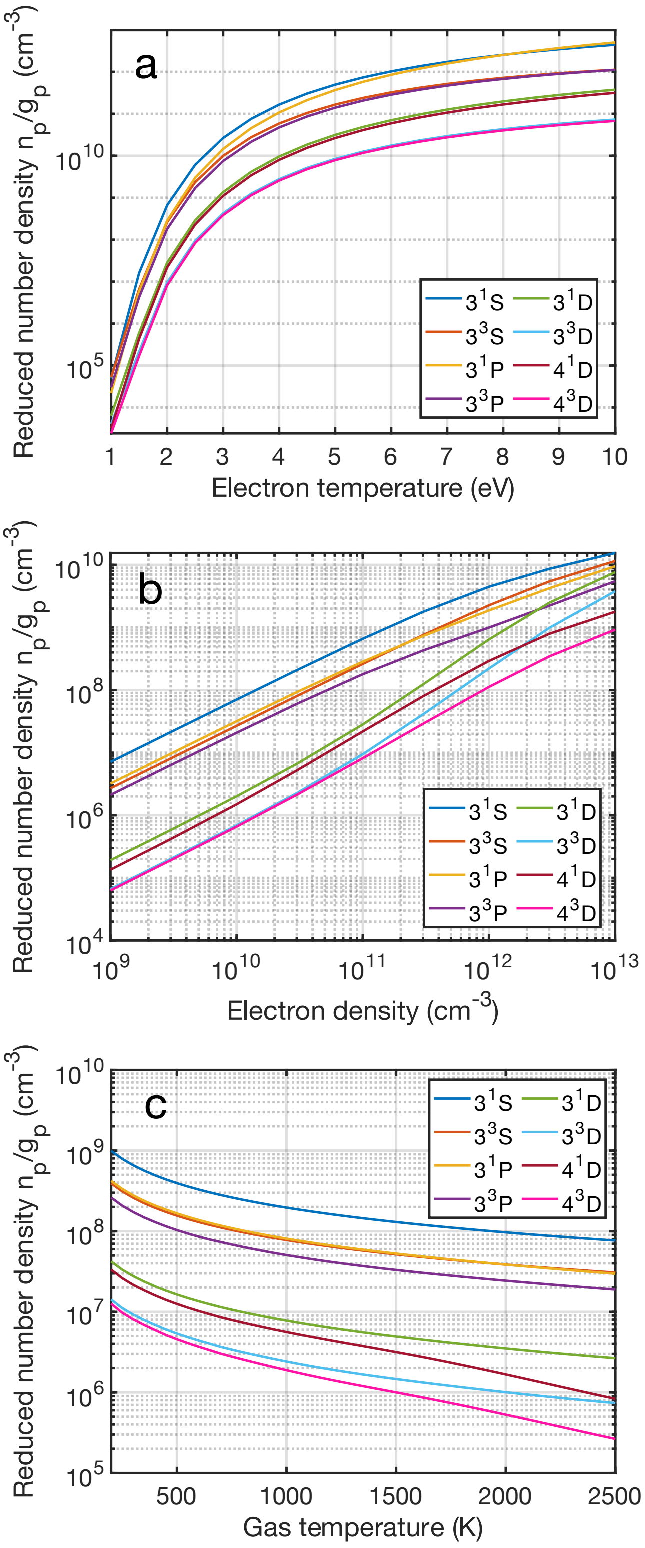

Figure 43. Dependency of number density the 8 input levels. Dependency of number density the 8 input levels. (a)Dependence of the number density of the eight input levels on the electron temperature. (b) Dependence of the number density of the eight input levels on the electron density. (c) Dependence of the number density of the eight input levels on the gas temperature.

6.3.2.2 Diagnosis of atmospheric-pressure helium plasma

The following figure shows the theoretical spectral emissivity with Maxwellian EEDF in different electron density and temperature.

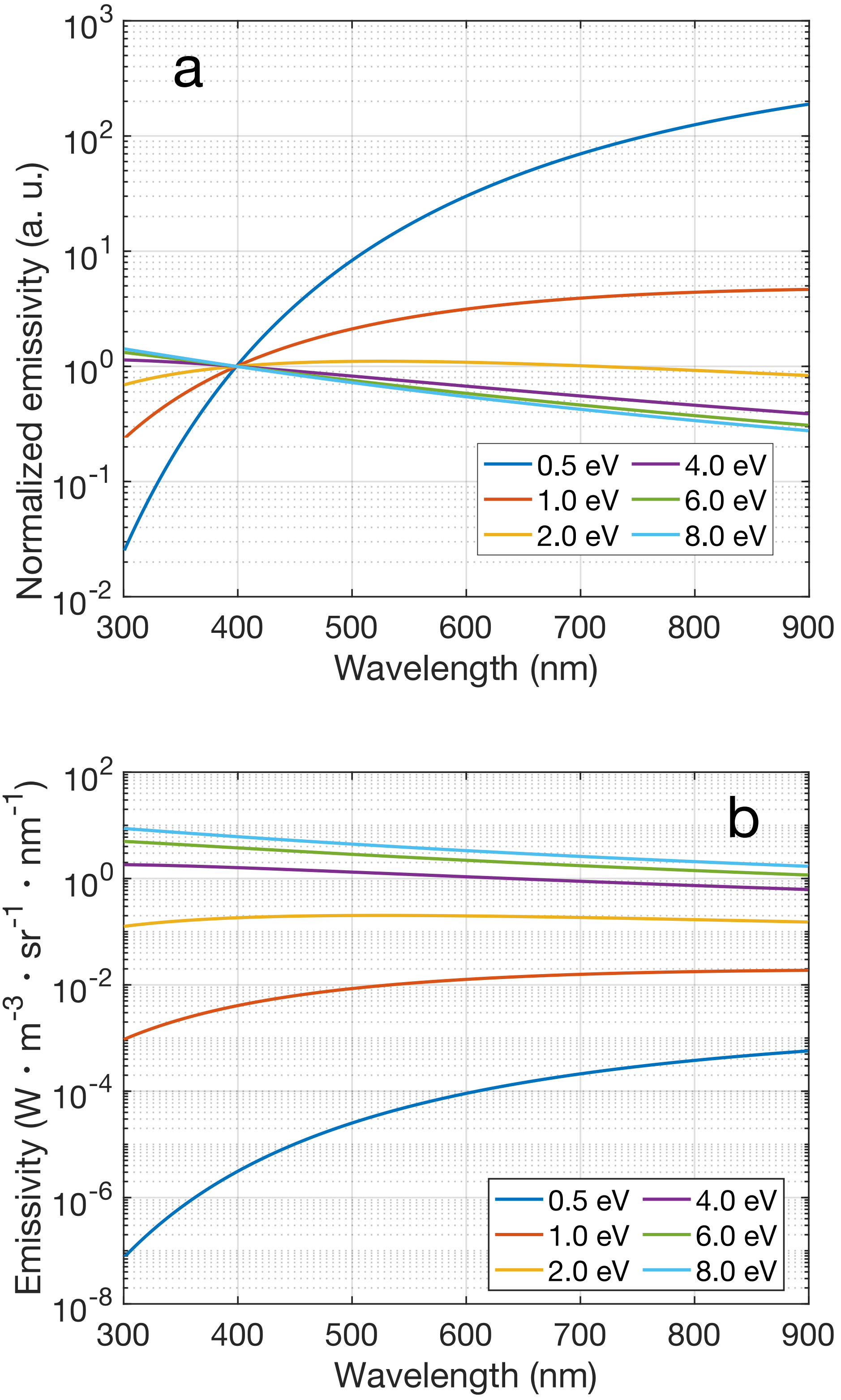

Figure 44. Emissivity with electron temperature from 0.5 to 8.0 eV. (a) Theoretical emissivity normalized at 400 nm. (b) Absolute emissivity with electron density $N_e = 10^{13}$ cm^{-3}.

Figure 45 shows the fitting curves for different electron temperatures and the emissivity normalised at 400 nm. Figure 45 (a) shows that an electron temperature of 1.7 eV, the theoretical emissivity was best agreed with the experimental data. The theoretical value was slightly lower than the emissivity measured in the experiment from 400 to 550 nm and exceeded the experimental data from 700 to 800 nm. Figure 45 (b) indicates that the blue line ($T_\mathrm{e} = 1.4$ eV) has a relatively better fit with the experimental data in the range of 400 - 470 nm.

As shown in Figure 46, the electron density and temperature obtained by the algorithm in this study were $3.2 \times 10^{10}\ \mathrm{cm}^{-3}$ and 1.42 eV, respectively. This result was plotted as the theoretical emissivity, and compared with the best fit of the continuum analysis. The results are shown in Figure 45. The electron density and temperature determined by the continuum spectrum analysis were $2.6 \times 10^{10}\ \mathrm{cm}^{-3}$ and 1.7 eV, respectively. The emissivity calculated by the electron density and temperature determined by the algorithm was approximately 1/2 of the emissivity measured in the experiment. The electron density and temperature values obtained by the two different methods are very close, and the fitting lines also agree well.

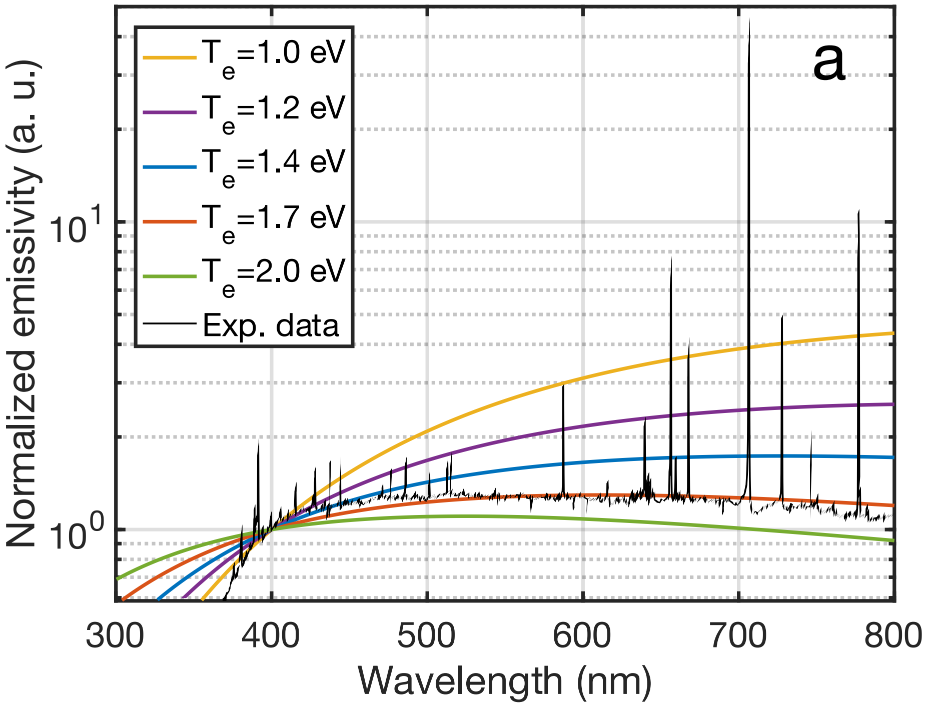

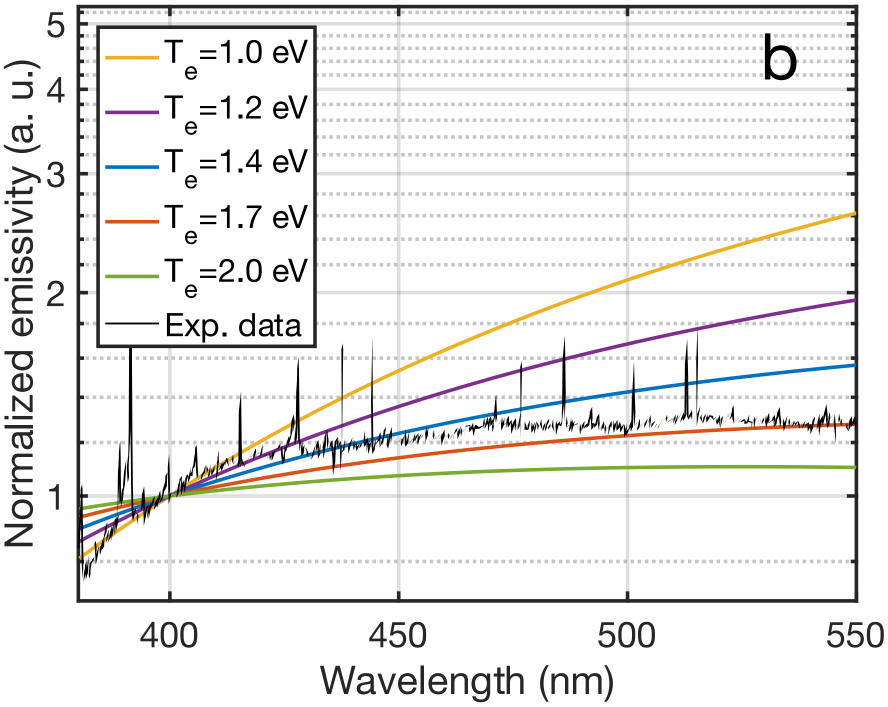

Figure 45. Fitting of the emission spectrum of the atmospheric-pressure plasma in the visible range by the normalized emissivity with Eq. (2.2.1). (a) Normalized emissivity in the range of 300 - 800 nm. (b) Normalized emissivity in the range of 380 - 550 nm.

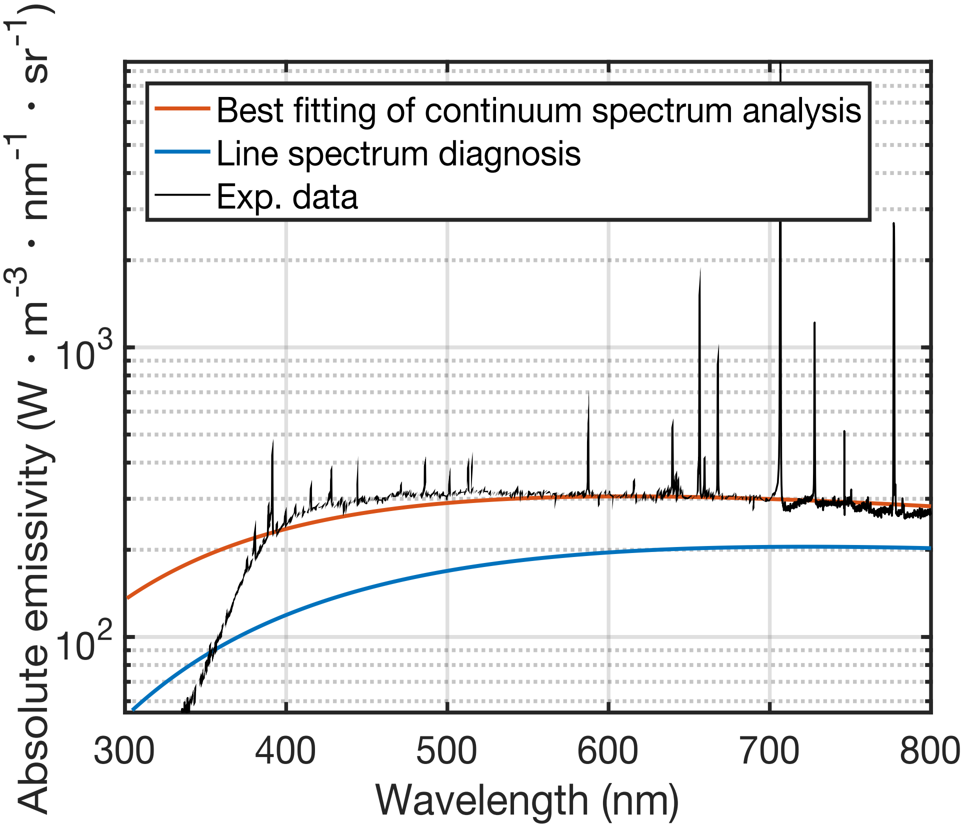

Figure 46. Comparison between the result diagnosed by the developed spectrum and continuum spectrum analysis.

Figure 47 shows the number density of the eight levels measured in the experiment and fitted by the algorithm. Levels 3^1S, 3^3D, and 4^1D show the best fit, and the calculated number density is very close to the result measured in the experiment. There is relatively large difference in the levels 3^3S, 3^1D, and 4^3D. Because they are in the same order of magnitude, the difference is acceptable. The difference in the lines of 3^1P (501.568 nm) and 3^3P (388.864 nm) was larger than that of the other levels. In particular, for 3^3P, the fitted data were 10 times larger than the experimental data. This could be due to the relatively strong line at 391 nm that overlaps with 388 nm in the measured spectrum. This affects the determination of the line width and height when calculating of the number density. Therefore, the measured number density of the state

3^3P is not accurate enough. A similar problem also exists for the state 3^1P due to its weak intensity. These problems might be solved by increasing the exposure time and resolution of the spectrometer.

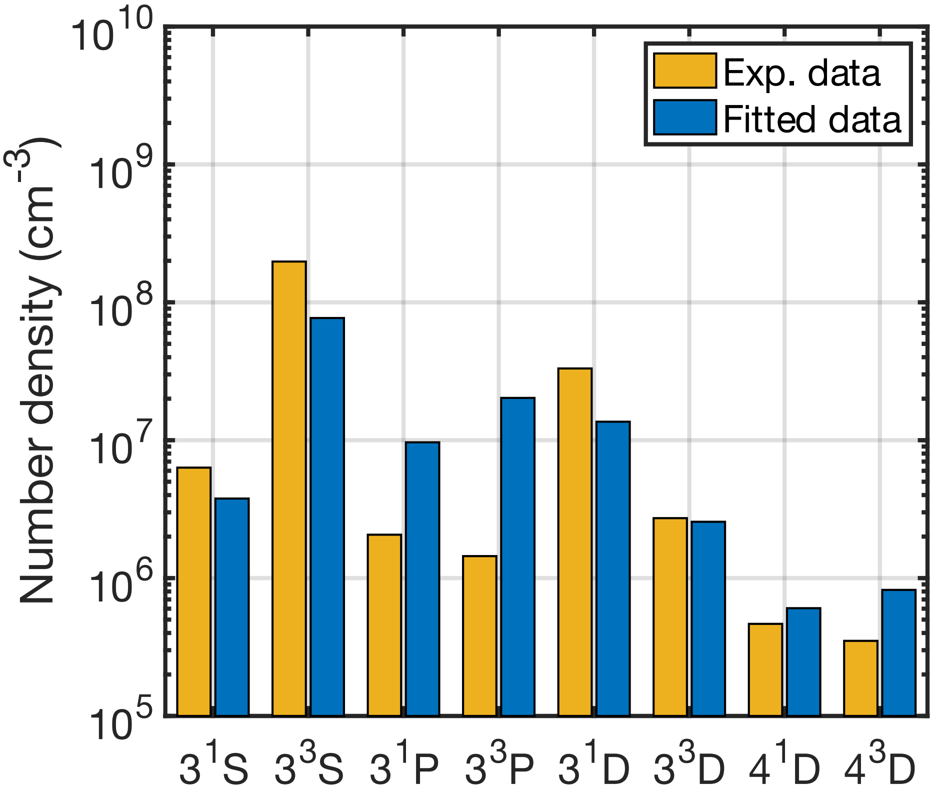

Figure 47. Comparison between the result diagnosed by the developed spectrum and continuum spectrum analysis.

The He_2^+ molecular ion have not been taken into account in this study. Although cross sections for the dissociative recombination of the He_2^+ in the energy region of 1-15 eV have been investigated [79], its influence to the excited state populations have not been studied yet. It brings uncertainty to the excited state populations. However, considering the results of the continuous spectrum measurement, it seems that the plasma parameters can be obtained with acceptable accuracy even if it is ignored under the experimental condition in this study.

Overall, it can be concluded that the algorithm developed in the present study is reliable for diagnosing the electron density and temperature of non-equilibrium atmospheric-pressure helium plasma. The revised CR model has wider applications than the conventional model due to its validity at atmospheric pressure.

7. CONCLUSION AND FUTURE PROSPECTS

7.1. Summary and Highlights

7.1.1. Conclusion for diagnosis based on the simplified CR model

In the study of dominant processes analysis, A simplified model based on the low-pressure helium CR model was developed by extracting dominant processes. The model is able to determine electron density and temperature of helium plasma by input number density of excited levels 3^1S, 3^3S, and 3^1D. Rate equations consist of the extracted processes is built, and the electron density and temperature can be determined by finding the global minimum of the rate equation.

Reliability of the simplified model was verified theoretically and experimentally. Different combinations of preset electron temperature and density were input to the low-pressure helium CR model. Calculated number density of excited levels 3^1S, 3^3S, and 3^1D were used to examine the theoretical error of the simplified model. The results showed the simplified model has considerably high accuracy at most electron temperature range. The error of calculated electron density was relatively larger. In experiment, the inverse model was applied with OES measurement. Helium plasma at different pressure and measurement position was diagnosed. The experimental results showed that extraction of essential process is an effective way to simplify the calculation CR model. In the range of $T_{\mathrm{e}} = 1.0 - 4.0\ \mathrm{eV}$ and $N_{\mathrm{e}} = 10^{11} - 10^{12}\ \mathrm{cm}^{-3}$, the model has relative high accuracy.

In general, the method developed in this study has good performance in the experiment. It provides a new choice to diagnose low-pressure helium plasma with relatively simple calculation, less input, and high accuracy.

7.1.2. Conclusion for low-pressure LHD diagnostics

In the study of low-pressure diagnosis of electron density and temperature with very high electron temperature which can be applicable even to the thermonuclear fusion plasma, the helium CR model was modified by including the optical escape factor. The algorithm was developed to use the n_e, T_e, n_1, $\Lambda_{4,1}$, $\Lambda_{8,1}$, and $\Lambda_{14,1}$ to fit eight emission lines in the visible wavelength range. According to the results, the algorithm is capable of determining the electron density and temperature of the LHD helium plasma precisely. The disagreement of the line at 501.6 nm in the conventional three-line diagnosis can be solved by including optical escape factor to the CR model and increasing the number of input lines from three to eight.

However, in the developed algorithm, the differences between the measured and fitted results of the states 3^1S, 3^3S, and 3^1D slightly increased compared to the conventional method. This could be improved by including statistical weight to the object function. In general, the algorithm has a good performance in the determination of the electron density and temperature.

The algorithm provides another choice to determine the electron density and temperature for the low-pressure helium plasma with OES method, and can be applied to plasma in various conditions. The validity of the algorithm for the other types of helium plasma will be further investigated in the future.

7.1.3. Conclusion for atmospheric-pressure diagnostics

In the study of atmospheric-pressure diagnosis of electron density and temperature, the valid pressure of the conventional CR model was extended to atmospheric pressure by including atomic collision processes. The developed algorithm is able to diagnose the electron density and temperature by inputting number density of eight states (3^1S, 3^3S, 3^1P, 3^3P, 3^1D, 3^3D, 4^1D, and 4^3D) that can be measured in the visible wavelength range using the OES method.

The theoretical error shows that the algorithm can inversely solve the revised CR model accurately. The results of the low-pressure microwave-induced helium plasma experiment show that this method is as reliable as the probe method for measuring low-pressure helium. It is safe and effective because it does not require direct contact with the plasma. In the atmospheric-pressure helium plasma measurement experiment, the results show that this algorithm has the same accuracy as the continuum spectrum analysis. This provides another way to obtain the electron density and temperature of atmospheric pressure non-equilibrium helium plasma with a low degree of ionisation, in addition to the OES of the continuum spectrum. Overall, according to the present experimental results, the algorithm has a relatively high accuracy for both low-pressure and atmospheric-pressure helium plasmas with an electron temperature not exceeding 10 eV. It is proposed to apply both line and continuum spectrum analyses to atmospheric-pressure helium plasmas to obtain more accurate results.

For plasma at extremely high temperatures or helium plasma mixed with other gases, the reliability of the algorithm needs to be further verified. The influence of the He_2^+ also needs to be investigated in the future.

7.2. Prospects for Future Research

7.2.1. Future prospects of diagnosis based on the simplified CR model

In the extraction of essential processes in the present study, population and depopulation fluxes in the low-pressure helium CR model were only investigated in a limited range. The electron temperature was set to values lower than 5 eV, and the electron density was in the range of 10^{10} – 10^{12} cm^{-3} which corresponds to the condition of low-pressure microwave discharge. Characteristic of dominant processes can be further studied in wider ranges to expand the validity of the method. For example, the helium plasma in applications of nuclear fusion usually has electron temperature higher than 100 eV. The electron density is also higher than 10^{12} cm^{-3} in some cases. Investigating the essential processes in those ranges is valuable for simplifying the diagnosis for helium plasma at higher temperature in applications. In addition, the method of dominant processes extraction can be also applied to other CR model, such as atmospheric pressure helium and argon CR model. This could be helpful for understanding the influence of neutral impacts to CR model at higher pressure.

7.2.2. Future prospects of low-pressure LHD diagnostics

In the study of low-pressure LHD diagnostics, the quasi-steady-state was assumed for the CR model. The time differential of all levels except 1^1S was neglected. Although, the metastable stats 2^1S and 2^3S has relaxation time much smaller than the ground state, it is much higher than the other levels ($p \geq 4$). The reabsorption by metastable states may also have influence to the results. Therefore, including time differential and escape factors of the metastable states to the CR model could further improve the accuracy in the future.

7.2.3. Future prospects of atmospheric-pressure diagnostics

The atmospheric-pressure helium plasma diagnosis base on the new CR model developed in this study applied the Maxwellian EEDF in the calculation of rate coefficients. It is found that the distribution of electron energy shows Maxwellian characteristics from 1 to 20 eV at low temperature. However, the real distribution decreases faster than the Maxwellian distribution when the electron energy is larger than 20 eV. If the electron energy distribution can be described in a more accurate way, the model could have higher accuracy. In addition, the helium molecular ions are essential in some cases at atmospheric pressure. It is important to study their influence to the CR model in the future.

Acknowledgement

I would like to acknowledge the valuable contributions and support of various individuals who have played a significant role in the successful completion of this research. Their guidance, expertise, and assistance have been instrumental in shaping the content and direction of this chapter.

First and foremost, I extend my sincere gratitude to my esteemed supervisor, Prof. Hiroshi Akatsuka, whose expert guidance and insightful feedback have been invaluable throughout this research. His mentorship has been pivotal in ensuring the rigor and relevance of the content presented in the thesis.

I would like to express my appreciation to Prof. Motoshi Goto for his generous assistance and profound insights into the study of LHD helium plasma. His expertise has broadened the scope and depth of the research conducted.

Special thanks are due to Mr. Atsushi Nezu for his unwavering support in conducting experiments. His dedicated efforts have contributed significantly to the acquisition of crucial data for the analysis.

I am grateful to Dr. Thijs van der Gaag for his valuable advices on continuum spectrum analysis and his expertise in programming on Matlab. His contributions have strengthened the analytical aspects of the research.

I also wish to acknowledge and thank the other members of the Akatsuka lab for their engaging discussions and constructive feedback, which have played a key role in shaping the ideas and refining the content.

Lastly, I am deeply thankful to my family, friends, and loved ones for their unwavering encouragement and understanding during the course of this research.

The collaborative efforts and support of these exceptional individuals have made a significant difference in the quality and outcomes of this chapter. Their contributions have been pivotal in advancing the scientific knowledge presented here, and I am truly honored to have had the opportunity to work with such exceptional mentors and colleagues.

Reference

[1] T. Fujimoto, *Plasma Spectroscopy* (Clarendon Press, Oxford, 2004).

[2] M. Ueda, L. A. Berni, and G. F. Gomes, *J. Appl. Phys.* **86**, 4821 (1999).

[3] R. Günzel, M. Betzl, I. Alphonsa, B. Ganguly, P. I. John, S. Mukherjee, *Surf. Coat. Technol.* **112** (1-3), 307-309 (1999).

[4] M. Chen, Z. Y. Zou, J. M. Huang, B. N. Ye, and W. G. Qian, *Rev. Sci. Instrum.* **65**, 1340 (1994).

[5] A. Zaikovskii and S. Novopashin, *Mater. Today: Proc.* **4** (11), 11406-11410 (2017).

[6] D. K. Kostrin and A. A. Lisenkov, *IOP Conf. Ser.: Mater. Sci. Eng.* **387**, 012041 (2018).

[7] E. Martines, P. Brun, R. Cavazzana, L. Cordaro, M. Zuin, T. Martinello, C. Gomiero, A. Perazzi, L. Melotti, L. Maccatrozzo, M. Patruno, and I. Iacopetti, *Clin. Plasma Med.* **17-18**, 100095 (2020).

[8] E. García-Alcantara, R. López-Callejas, P. R. Morales-Ramírez, R. Peña-Eguiluz, R. Fajardo-Muñoz, A. Mercado-Cabrera, S. R. Barocio, R. Valencia-Alvarado, B. G. Rodríguez-Méndez, A. E. Muñoz-Castro, A. de la Piedad-Beneitez, and I. A. Rojas-Olmedo, *Arch. Med. Res.* **44** (3), 169-177 (2013).

[9] A. I. Al-Shamma'a, S. R. Wylie, J. Lucas, and J. Yan, *IEEE Trans. Plasma Sci.* **30** (5), 1863-1871 (2002).

[10] S. R. Wylie, A. I. Al-Shamma'a, J. Lucas, and R. A. Stuart, *Mater. Process. Technol.* **153-154** (10), 288-293 (2004).

[11] T. Hino, E. Hayashishita, Y. Yamauchi, M. Hashiba, Y. Hirohata, and A. Kohyama, *Fusion Eng. Des.* **71** (1), 51-56 (2005).

[12] H. Ullmaier, *Nucl. Fusion* **24**, 1039 (1984).

[13] R. Sakamoto, E. Bernard, A. Kreter, and N. Yoshida, *Nucl. Fusion* **57**, 016040 (2017).

[14] J. Cooper, *Rep. Prog. Phys.* **22**, 35 (1966).

[15] H. R. Griem, *Plasma Spectroscopy* (McGraw-Hill, New York, 1964).

[16] H. R. Griem, *Principles of Plasma Spectroscopy* (Cambridge University, Cambridge, 1997).

[17] R. H. Huddlestone and S. L. Leonard, *Plasma Diagnostic Techniques* (Academic Press, New York, 1965).

[18] H. A. Bethe and E. E. Salpeter, *Quantum Mechanics of One- and Two-Electron Atoms* (Plenum, New York, 1957).

[19] E. U. Condon and G. H. Shortley, *Theory of Atomic Spectra* (Cambridge University Press, London, 1935).

[20] G. Hertzberg, *Atomic Spectra and Atomic Structure* (Dover, New York, 1944).

[21] B. W. Shore and D. H. Menzel, *Principles of Atomic Spectra* (John Wiley and Sons, New York, 1968).

[22] A. Thoren, U. Litzén, and S. Johansson, *Spectrophysics* (Springer, Berlin, 1999).

[23] H. E. White, *Introduction to Atomic Spectra* (McGraw-Hill, New York, 1934).

[24] T. Fujimoto, *J. Quant. Spectrosc. Radiat. Transfer* **21**, 439 (1979).

[25] H. Akatsuka and M. Suzuki, *Contrib. Plasma Phys.* **34** (4), 539 (1994).

[26] T. Holstein, *Phys. Rev.* **72**, 1212 (1947).

[27] T. Holstein, *Phys. Rev.* **83**, 1159 (1951).

[28] T. Fujimoto and Y. Nishimura, *J. Quant. Spectrosc. Radiat. Transfer* **34**, 217 (1985).

[29] E. Akdoğan and H. T. Şirin, *Mater. Sci. Eng. C* **131**, 112474 (2021).

[30] D. Boehm and C. Canal, *Appl. Sci.* **11** (16), 7203 (2021).

[31] X. Yang, Y. Liu, W. Xu, Y. He, and G. Xia, *Nucl. Fusion* **63,** 066001 (2023).

[32] O. Kaneko, *Magnetic Fusion Energy* **15**, 469 (2016).

[33] Kil-Byoung Chai and Duck-Hee Kwon, *Spectrochim. Acta B* **183**, 106269 (2021).

[34] H. Akatsuka, *Phys. Plasmas* **16**, 043502 (2009).

[35] F. Jia, Y. Wu, Q. Ming, M. Su, K. Takeda, K. Ishikawa, H. Kondo, M. Sekine, M. Hori, Z. Zhong, *Plasma Sci. Technol.* **22** (6), 065404 (2020).

[36] R. F. Boivin, J. L. Kline, and E. E. Scime, *Phys. Plasmas* **8**, 5303 (2001).

[37] M. Goto and K. Sawada, *J. Quant. Spectrosc. Radiat. Transfer* **137**, 23 (2014).

[38] Neslihan Şahin and Murat Tanışlı, *Eur. Phys. J. Plus* **135**, 653 (2020).

[39] Yu. V. Ralchnko, R. K. Janev, T. Kato, D. V. Fursa, I. Bray, and F. J. de Heer, Cross Section Database for Collisional Processes of Helium Atom with Charged Particles. I. Electron Impact Processes, Rep. NIFS-DATA-**59**, NISF, Nagoya, Japan (2000).

[40] M. Goto, *J. Quant. Spectrosc. Radiat. Transfer* **76**, 331 (2003).

[41] M. B. Shah, D. S. Elliott, P. McCallion, and H. B. Gilbody, *J. Phys. B.* **21**, 2751 (1988).

[42] G. Gousset and C. Boulmer-Leborgne, *Journal de Physique* **45** (4), 689 (1984).

[43] L. C. Cusachs and H. S. Aldrich, *Chem. Phys. Lett.* **12** (1), 197 (1971).

[44] F. Devos and J. Boulmer, *Journal de Physique* **40** (3), 215 (1979).

[45] J. Gruninger *et al.*, *Int. J. Quantum Chem.* **7**, 103 (1973).

[46] O.G. Verin, *Russ. Phys. J.* **65**, 710 (2022).

[47] H. W. Drawin and F. Emard, *Z. Physik* **254**, 202 (1972).

[48] T. Fujimito, *J. Phy. Soc. Jpn.* **47**, 265 (1979).

[49] T. Fujimito, *J. Phy. Soc. Jpn.* **47**, 273 (1979).

[50] T. Fujimito, *J. Phy. Soc. Jpn.* **49**, 1561 (1980).

[51] T. Fujimito, *J. Phy. Soc. Jpn.* **49**, 1569 (1980).

[52] T. Kawachi and T. Fujimito, *Phys. Rev. E* **51**,1440 (1995).

[53] K. Tachibana and K. Fukuda, *Jpn. J. Appl. Phys.* **12**, 895 (1973).

[54] H. Akatsuka and M. Suzuki, *Phys. Rev. E* **49**, 1534 (1994).

[55] H. Akatsuka and M. Suzuki, *Plasma Sources Sci. Tech.* **4**, 125 (1995).

[56] T. Fujimito, *J. Phy. Soc. Jpn.* **49**, 1591 (1980).

[57] U. Fantz, *Plasma Sources Sci. Techinol.* **15**, S137-S147 (2006).

[58] H. Onishi, F. Yamazaki, Y. Hakozaki, M. Takemura, A. Nezu, and H. Akatsuka, *Jpn. J. Appl. Phys.* **60**, 026002 (2021).

[59] K. T. A. L. Burn, *Plasma Sources Sci. and Technol.* **13**, 387 (2004).

[60] S. Parl, W. Choe, S. Youn Moon, and J. Park, *Appl. Phys. Lett.* **104**, 084103 (2014).

[61] W. Graef, "The LXCat Project," 73rd Annual Gaseous Electronics Virtual Conf. (73rd GEC, APS) (LT1.00008, 2020).

[62] E. O. Jhonson, and L. Malter, *Phys. Rev*, Vol. 80, 58, 1950.

[63] S. Matsumura, "Measurements of Electron Density and Electron Temperature by a Double Probe", *Introduction to Plasma Experiments IV*, 4.3, 1993.

[64] T. Dote, *J. Appl. Phys*., Vol. 7, 964, 1968.

[65] Yu. A. Lebedev, Phys. Conf. Ser. **257** (2010) 012016.

[66] K. Sawada, Y. Yamada, T. Miyachika, N. Ezumi, A. Iwamae, M. Goto, *Plasma Fusion Res.* **137**, 23 (2014).

[67] F. E. Irons, *J. Quant. Spectrosc. Radiat. Transfer* **22**, 1-20 (1979).

[68] S. Kim, K. Koh, M. Lustig, S. Boyd, and D. Gorinevsky, *IEEE J. Sel. Top. Signal Process.* **1** (4), 606 (2007).

[69] Y. Zhang, *Optim. Methods Softw.* **10** (1), 1 (1998).

[70] M. Rajasekhar Reddy, B. Nithish Kumar, N. Madhusudana Rao, and B. Karthikeyan, "A New Approach for Bias–Variance Analysis Using Regularized Linear Regression," *Advances in Bioinformatics, Multimedia, and Electronics Circuits and Signals* (Springer, Singapore, 2020).

[71] R.C.Wilson and E. R.Hancock, *Comput. Vis. Image Underst.* **77** (1), 25 (2000).

[72] S. Doroudi, *AERA Open* **6** (4), 2332-8584 (2020).

[73] H. Onishi, F. Yamazaki, Y. Hakozaki, M. Takemura, A. Nezu, and H. Akatsuka, *Jpn. J. Appl. Phys.* **60**, 026002 (2021).

[74] H. Akatsuka, *Phys. Plasmas* **16**, 043502 (2009).

[75] A. Bogaerts and R. Gijbels, *J. Appl. Phys.* **84**, 121 (1998).

[76] T. Fujimoto, *J. Quant. Spectrosc. Radiat. Transfer* **21**, 439 (1979).

[77] J. Royal and A. E. Orel, *Phys. Rev. A* **72**, 022719 (2005).

[78] S. Sivanandam, and S. Deepa, *"Genetic Algorithm Implementation Using Matlab"*. *Introduction to Genetic Algorithms*, Springer, Berlin, Heidelberg (2008).

[79] J. Royal and A. E. Orel, *Phys. Rev. A* **72**, 022719 (2005).